Chemical Reaction Dynamics of the Liquid/Vapor Interface Studied by Mass Spectrometry

Thesis by

Daniel A. Thomas

In Partial Fulfillment of the Requirements for
the Degree of
Doctor of Philosophy

CALIFORNIA INSTITUTE OF TECHNOLOGY
Pasadena, California

2016
(Defended May 16, 2016)

Daniel A. Thomas
ORCID: 0000-0001-9415-5991

ACKNOWLEDGEMENTS

Achievement in science is not the work of an individual. I could not write this thesis without the incredible resources invested in me by countless friends, family members, teachers, and advisors. To all of you, I am grateful for your encouragement, your advice, and your sacrifice on my behalf.

I didn't know I wanted to go to graduate school until well into my junior year of college. I didn't even know I wanted to be a chemist. But there are many people who taught me the skills I would need in graduate school long before I ever arrived. I am so thankful for Diane Bailes, who demonstrated by example what it means to challenge, support, and encourage a student. Tim Gilland taught me to keep challenging myself and to seek help when you need it. Sue Sams showed me what an instructor can accomplish with meticulous preparation and contagious enthusiasm.

The world of scientific research was opened to me by Gary Glish, who gave me a position in his lab and let me play with a prototype mass spectrometer. Jared Bushey and Natalie Thompson were fantastic graduate student advisors who encouraged me to become more involved in research. Takashi Baba taught me almost everything I know about mass spectrometers and often let me take on important tasks that he could have completed himself in one tenth of the time. Thanks also to Ali, Mark, Asher, Atim, Natalie, Masaki, Dave, and Alice for being great labmates and friends.

Chemistry at Caltech goes nowhere without the hard work of the division staff. Priscilla Boon keeps everything in the group running. You can even spot her working hard on the weekends, making sure it all goes off without a hitch. Agnes works tirelessly on the behalf of graduate students. Elisa and Steve order every weird thing you can think of as quickly as possible. Rick and Mike are masters of glass and steel, respectively. Mona, Dave, and Angelo provide amazing resources for sample analysis. Memo will travel up many flights of stairs to bring you packages. Joe Drew can fix just about any problem you can dream up. Thanks to all of you.

I am lucky enough to have worked alongside many great researchers while here at Caltech. Chang Ho Sohn introduced me to the lab and shared his insights on gas-phase free radical chemistry. Jinshan Gao taught me synthetic chemistry and let me work with him on glycan sequencing. Wilton Mui taught me about aerosol particle classification and brought his ROMIAC to the lab so we could do biomolecule separation. Matt Coggon was instrumental in getting the work on photo-Fenton chemistry off the ground. Lingtao Wang set up his self-focusing acoustic transducer in our lab so we could study heterogeneous chemistry. Nathan Dalleska lent his expertise on countless projects and readily provided me with access to the EAC (anyone who has ever been to Nathan's office and seen the line of postdocs and graduate students outside his door knows what an invaluable contribution he makes to research at Caltech). Scott Virgil loaned me some of his equipment with incredible friendliness and enthusiasm. Thanks also to Monika, Paul, Mohammad, Kerry, Byoungsook, Aleena, Matt, Lily, Andrew, Jenny, Fedor, Cassy, Alex, Keziah, Reilly, and Taylor for all of your hard work.

Kate and Kevin have been in the lab with me almost since the beginning. Thanks for your friendship over the last five years.

Thanks to everyone at the CTLO. Noelle and Kelsey have done great things for teaching and learning at Caltech through CPET. James, Julius, and Mitch are the best outreach team in existence. Leslie and Ellie pull off every event with an air of effortlessness that can only come from hard work. Holly and Jenn have both offered me so much advice and put in countless hours to guide CPET into the future. I am grateful to Tina for all of her hard work and her friendship. Cassandra Horii has been a second advisor to me during graduate school. She has challenged me to do great things and has followed up with incredible instruction and encouragement. I am so thankful for her support.

Thanks to Jack. I am grateful to Jack for always supporting his graduate students in their work. He has also taught me that ideas that might sound crazy often lead to new avenues of research. I am most grateful for his "family comes first" perspective that has allowed me to spend time at home as well as in the lab.

I am thankful for all of the folks at Grace Pasadena, who have provided us with community, fellowship, and encouragement over the last six years. To to all of our neighbors, I wish that moving wasn't mandatory upon graduation. Thanks especially to Brock, Lindsay, Aubrey, Annabelle, Myoung, Irene, Violet, and Chloe.

Thanks to all of the wonderful people at LCPCICC and the CCC for all of the time they have invested in caring for Florence. Thanks especially to Grace Ayubo and Starla Richardson, who have helped Florence grow and learn so much.

Thanks to my family. My parents have been an endless source of support for me. They have endured phone calls in the middle of the night seeking medical advice, and they have spent weeks in California caring for Florence. I am so grateful to my wife, Claire, who has supported me through long weeks in lab and offered much advice in science and in life. I never would have made it through graduate school without you. Thanks to Florence. Coming home to see you is the best part of the day.

ABSTRACT

This thesis presents investigations of chemical reactions occurring at the liquid/vapor interface studied using novel sampling methodologies coupled with detection by mass spectrometry. Chapters 2 and 3 utilize the recently developed technique of field-induced droplet ionization mass spectrometry (FIDI-MS), in which the application of a strong electric field to a pendant microliter droplet results in the ejection of highly charged progeny droplets from the liquid surface. In Chapter 2, this method is employed to study the base-catalyzed dissociation of a surfactant molecule at the liquid/vapor interface upon uptake of ammonia from the gas phase. This process is observed to occur without significant modulation of the bulk solution pH, suggesting a transient increase in surface pH following the uptake of gaseous NH_3. Chapter 3 presents real-time studies of the oxidation of the model tropospheric organic compound glycolaldehyde by photodissociation of iron (III) oxalate complexes. The oxidation products of glycolaldehyde formed in this process are identified, and experiments in a deoxygenated environment identify the role of oxygen in the oxidation pathway and in the regeneration of iron (III) following photo-initiated reduction. Chapter 4 explores alternative methods for the study of heterogeneous reaction processes by mass spectrometric sampling from liquid surfaces. Bursting bubble ionization (BBI) and interfacial sampling with an acoustic transducer (ISAT) generate nanoliter droplets from a liquid surface that can be sampled via the atmospheric pressure interface of a mass spectrometer. Experiments on the oxidation of oleic acid by ozone using ISAT are also presented. Chapters 5 and 6 detail mechanistic studies and applications of free-radical-initiated peptide sequencing (FRIPS), a technique employing gas-phase free radical chemistry to the sequencing of peptides and proteins by mass spectrometry. Chapter 5 presents experimental and theoretical studies on the anomalous mechanism of dissociation observed in the presence of serine and threonine residues in peptides. Chapter 6 demonstrates the combination of FRIPS with ion mobility-mass spectrometry (IM-MS) for the separation of isomeric peptides.

PUBLISHED CONTENT AND CONTRIBUTIONS

Chapters 1 and 4 are based in large part on the publication:

Thomas, Daniel A.; Wang, Lingtao; Goh, Byoungsook; Kim, Eun Sok; Beauchamp, J.L. Mass Spectrometric Sampling of a Liquid Surface by Nanoliter Droplet Generation from Bursting Bubbles and Focused Acoustic Pulses: Application to Studies of Interfacial Chemistry. *Anal. Chem.* **2015**, *87*, 3336-3344. http://dx.doi.org/10.1021/ac504494t

D.A.T. was the lead researcher on this project and the main author of the manuscript.

Chapter 5 is based in large part on the publication:

Thomas, Daniel A.; Sohn, Chang Ho; Gao, Jinshan; Beauchamp, J. L. Hydrogen Bonding Constrains Free Radical Reaction Dynamics at Serine and Threonine Residues in Peptides. *J. Phys. Chem. A* **2014**, *118*, 8380-8392. http://dx.doi.org/10.1021/jp501367w

D.A.T. was the lead researcher on this project and the main author of the manuscript.

Chapter 6 is based in large part on the publication:

Mui, Wilton; **Thomas, Daniel A.**; Downard, Andrew J.; Beauchamp, J. L.; Seinfeld, John. H.; Flagan, Richard C. Ion Mobility-Mass Spectrometry with a Radial Opposed Migration Ion and Aerosol Classifier (ROMIAC). *Anal. Chem.* **2013**, *85*, 6319-6326. http://dx.doi.org/10.1021/ac400580u

D.A.T. assisted in experimental design and data collection, implemented biomolecule separation and sequencing by mass spectrometry, and contributed to the writing of the manuscript.

TABLE OF CONTENTS

LIST OF FIGURES

LIST OF SCHEMES

LIST OF TABLES

NOMENCLATURE

FIDI. Field-induced droplet ionization

MS. Mass spectrometry; typically combined with other nomenclature (e.g., FIDI-MS, ISAT-MS, BBI-MS, ROMIAC-MS, etc.)

HV. High voltage

HDB. Hexadecyl betaine (2-(hexadecyloxy)-N,N,N-trimethyl-2-oxoethan-1-aminium chloride)

ESI. Electrospray ionization

SSI. Sonic spray ionization

SOA. Secondary organic aerosol

BBI. Bursting bubble ionization

ISAT. Interfacial sampling with an acoustic transducer

PZT. Piezoelectric transducer

VSFG. Vibrational sum frequency generation

HPLC. High-performance liquid chromatography

FRIPS. Free-radical-initiated peptide sequencing

TEMPO. 2,2,6,6-tetramethylpiperidine-1-oxyl free radical

BDE. Bond dissociation energy

IMS, IM-MS. Ion mobility spectrometry, ion mobility-mass spectrometry

ROMIAC. Radial opposed migration ion and aerosol classifier

C h a p t e r 1

INTRODUCTION

(Reproduced in part with permission from Thomas, D. A.; Wang, L.; Goh, B.; Kim, E. S.; Beauchamp, J.L. *Anal. Chem.* **2015**, *87*, 3336-3344. http://dx.doi.org/10.1021/ac504494t

1.1 Background

The liquid/vapor interface is one of the most ubiquitous chemical environments in nature, present on the surface of oceans and lakes,[1] on cloud and fog waters,[2-4] on aqueous deliquescent particles,[5,6] and in the human respiratory system.[7,8] As a result of its singular attributes including an immense change in density on molecular length scales,[9] the existence of a localized electrical potential,[10-13] and the presence of free surface hydroxyl groups,[14] this intriguing environment often serves as a medium for unique processes unobserved in bulk phases.[1,7,15-17] In the earth's atmosphere, processes such as adsorption of gas-phase molecules,[3,9,18-22] surface partitioning of amphiphilic or highly polarizable analytes,[9,11,23,24] and heterogeneous reactions between dissolved organics and gas-phase oxidants[17,25-28] can strongly influence the chemical evolution and properties of aqueous aerosol. In spite of the pervasiveness of the liquid/vapor interface, numerous attributes of this system remain poorly understood, with even the properties and structure of the neat water/air interface still the subject of much debate.[29]

The study of chemical or structural changes occurring at interfaces has been difficult, as the selective detection of molecules in the interfacial environment and their differentiation

from the underlying bulk phase is not straightforward. Specialized experimental methodologies are required to specifically study the chemistry occurring at the liquid/vapor interface, and among the most popular of these methods are the nonlinear optical spectroscopy techniques of vibrational sum frequency generation (VSFG) and second harmonic generation (SHG) spectroscopy, in which transitions are forbidden in media with inversion symmetry (i.e., bulk phases), and the spectrum is therefore dominated by interface-specific surface resonances.[30,31] These techniques, in combination with theoretical simulations,[11,12,32-34] have been employed to study the structure of neat water at the interface,[35] the surface enhancement of hydronium and hydroxide ions,[36,37] the surface properties of inorganic ions,[38-40] and the orientation of molecules in the interfacial region.[41-43] Other interface-specific spectroscopic methods, including infrared-reflection absorption spectroscopy,[44-46] glancing-angle spectroscopy,[47-49] and Brewster angle microscopy[50-54] have also provided insight into the orientation and arrangement of molecules at the water surface. In addition, the properties of liquid/vapor interfaces have been studied recently by photoelectron spectroscopy of liquid jets,[55-58] neutron reflection from a liquid surface,[59] and grazing incidence X-ray diffraction of surface monolayers.[53,60-62] To study the dynamics and kinetics of exchange at the interface between gas- and liquid-phase species, droplet train flow reactor (DTFR) and molecular beam scattering experiments have been employed.[20,63,64]

Though the above methodologies yield extensive information on the structure and properties of the liquid/vapor interface, their application to the study of time-dependent, multicomponent chemical systems is challenging. Nevertheless, VSFG spectroscopy in particular has been successfully applied to the study of several chemical systems, including

the uptake and reaction of methanol on sulfuric acid solutions,[19] the oxidation of oleic acid by ozone,[27] and the uptake of SO_2 from the gas phase and subsequent reaction in aqueous solution.[65-67] In addition, the heterogeneous chemistry of model atmospheric aerosols has been studied by online chemical ionization mass spectrometry of organic particles,[68-70] VSFG of model sea spray aerosol,[71] and detection of products in large aerosol chambers.[11,15]

Several methods utilizing atmospheric pressure ionization mass spectrometry have also been developed recently to study the dynamics of chemical reactions at the water/air interface. Colussi, Hoffmann, and co-workers developed a technique based on sonic spray ionization (SSI)[72] for the analysis of interfacial reactions. Droplets in an aqueous microjet produced by SSI are exposed to gas-phase reactants and subsequently sampled by transfer through the atmospheric pressure interface of a mass spectrometer. This method has been used to examine several interfacial processes, including the reaction of halogen anions and organic species with ozone and the availability of hydronium ions at the interface.[73-78] In addition, surface-selective sampling of analytes has been achieved by laser ablation of droplets on a rod or suspended by acoustic levitation.[79-82]

The technique of field-induced droplet ionization mass spectrometry (FIDI-MS), developed by Grimm and co-workers, has been utilized for the time-resolved examination of interfacial reactions between a hanging droplet and gas-phase reagents.[83] In this method, the application of a strong electric field induces prolate elongation of a droplet, generating symmetric negatively and positively-charged Taylor cone-jets of highly charged progeny droplets, which are subsequently sampled by a mass spectrometer.[84,85] FIDI-MS has been applied to the investigation of oxidative damage in the lungs caused by the exposure of

various components of the lung surfactant system to ozone, highlighting the ability of this technique to analyze complex processes such as ozonolysis that are common at liquid/vapor interfaces.[7,86,87]

The studies presented in this thesis continue the investigations initiated by Grimm and co-workers into heterogeneous reactions occurring at the surface of liquid droplets. Chapter 2 details experiments examining base-catalyzed reactions occurring at the liquid/vapor interface upon uptake of ammonia from the gas phase. In addition, the FIDI apparatus has been redesigned and coupled to a new mass spectrometer to increase sensitivity and enable the exploration of more complex chemical systems. The design and fabrication of an enclosure for the source allows for greater control of ambient conditions during FIDI experiments, and this new apparatus is utilized in Chapter 3 to study the oxidation of glycolaldehyde initiated by photolysis of iron (III) oxalate complexes. Chapter 4 details the development of alternative methods for mass spectrometric sampling of the liquid/vapor interface, with special focus on the ejection of nanoliter droplets from the surface by focused acoustic waves.

The studies detailed in Chapters 5 and 6 do not address the chemistry of the liquid/vapor interface; instead, these chapters examine the application of gas-phase free radical chemistry to the sequencing of biomolecules. Specifically, Chapter 5 explores the mechanism of free-radical-initiated dissociation observed at serine and threonine residues in peptides, and Chapter 6 details the combination of a free-radical-initiated peptide sequencing (FRIPS) and ion mobility-mass spectrometry (IM-MS) for the separation of isomeric peptides.

1.2 Contents of Thesis

1.2.1 Base-Catalyzed Chemistry at the Liquid/Vapor Interface

Recent studies on the rapid unfolding and refolding of proteins in electrospray droplets exposed to gaseous acids and bases[88,89] prompted us to examine if similar conditions could initiate chemical changes at the liquid/vapor interface of a hanging droplet. As the uptake of gaseous acids and bases by aqueous particles is an important atmospheric process, such reactions also yield insight into the processing of tropospheric aerosol. Ammonia (NH_3) is the primary volatile base found in the atmosphere and thus plays an especially important role in atmospheric chemistry. Chapter 2 explores the dissociation of a dissolved base-cleavable surfactant upon exposure of pendant droplets to gas-phase NH_3. Importantly, the concentration of ammonia utilized in these experiments is insufficient to modulate the bulk droplet pH, yet significant surfactant dissociation is still observed, suggesting that unique conditions at the liquid/vapor interface increase the rate of this reaction. A simple model of analyte uptake into a droplet coupled with reaction and diffusion suggests that an increase in pH near the surface of the droplet occurs upon absorption of NH_3 from the gas phase.

1.2.2 Photochemistry of Iron (III) Oxalate: Oxidation of Organics

As an abundant inorganic component of atmospheric aerosol, iron is known to undergo many key redox processes that exert a strong influence on the composition and properties of tropospheric particles. For example, iron catalyzes the oxidation of sulfur dioxide to sulfate in mineral dust aerosols, resulting in the removal of sulfate from the atmosphere by aerosol deposition and altering the estimated radiative forcing of tropospheric sulfate

aerosol.[90] Dark Fenton chemistry and photo-Fenton chemistry, both of which produce hydroxyl radicals by iron redox processes in solution, have also been suggested as important processes in tropospheric aerosol.[91] In addition, the complexation of iron (III) with oxalic acid in aqueous solution results in the reduction of iron with high quantum yield and the generation of hydroxyl radicals.[92] Recent field experiments found an inverse correlation between the concentration of iron and oxalic acid in cloud waters in the northwest Pacific Ocean, suggesting this chemistry may also be operative in tropospheric systems.[93] In Chapter 3, we study the oxidation of glycolaldehyde, a model semi-volatile organic compound abundant in the troposphere, initiated by photodissociation of iron (III) oxalate complexes. We monitor the consumption of oxalic acid and identify the oxidation products generated in real time by FIDI-MS. The utilization of an enclosed FIDI source provides a means to control ambient conditions, and experiments conducted in a deoxygenated environment support the proposed mechanisms of reaction.

1.2.3 Alternative Methods for MS Sampling of Liquid Surfaces

Although FIDI-MS has proven an extremely effective method for the study of heterogeneous reactions occurring on a time scale of tens of seconds to minutes, the inability to sample from planar surfaces using this technique prompted the study of alternative sampling methods. The coupling of mass spectrometric sampling with surface pressure measurements in a Langmuir trough or similar device would provide real-time information on both the physical properties and chemical composition of a liquid surface over the course of a reaction. Toward this goal, Chapter 4 introduces the sampling techniques of bursting bubble ionization (BBI) and interfacial sampling with an acoustic

transducer (ISAT), in which droplets (0.5-10 nL volume) are ejected from the surface of bulk solution. In BBI, these droplets are generated at the tip of a liquid jet that fills the cavity left by a bursting bubble at a liquid surface. Utilizing ISAT, droplets are ejected on demand by piezoelectrically generated acoustic waves focused at the liquid/vapor interface. Experiments show that droplets generated by either method are near-neutral in net charge, suggesting that the production of gas-phase ions occurs by the breakup and charging of droplets during transfer through the atmospheric pressure interface of the mass spectrometer, similar to the process proposed for sonic spray or thermospray ionization. As a proof of concept for the study of heterogeneous reactions by ISAT-MS, we present results from experiments on the oxidation of aqueous oleic acid by ozone impinging upon the liquid surface from the gas phase.

1.2.4 Mechanism of Radical-Initiated Dissociation at Serine and Threonine

Free-radical-initiated peptide sequencing (FRIPS) is an alternative method for the dissociation of gas-phase peptide ions within a mass spectrometer that takes advantage of the unique reactions of free radicals to gain peptide sequence information. In its most recent incarnation, a free radical precursor is coupled to a peptide or protein, and gas-phase collisional activation results in the selective formation of an acetyl radical at the N-terminus by homolytic bond cleavage. This radical then initiates dissociation by abstraction of a hydrogen atom, typically from either C_α or C_β of the peptide side-chain. Recent experiments by Sohn and co-workers demonstrate nearly 100% sequence coverage utilizing this method in peptides that are challenging to sequence by standard collisional activation methods.[94] Anomalous dissociation patterns are observed at serine and threonine

residues within a peptide chain during FRIPS experiments. Chapter 5 details extensive experimental and theoretical studies of the mechanism of dissociation in the presence of these amino acids. It is found that hydrogen bonding between the side-chain hydroxyl group and backbone amide carbonyl results in distinct low-energy dissociation pathways the give rise to the anomalous product ions observed in FRIPS spectra.

1.2.5 Separation of Isomeric Peptides by FRIPS and IM-MS

The implementation of ion mobility spectrometry in combination with mass spectrometry (IM-MS) provides an additional degree of separation that greatly improves the analysis of complex samples. In proteomics experiments, the isolation of peptides with strong sequence homology, which are challenging to separate by liquid chromatography alone, may yield significantly more insight into the expression levels and role of cellular proteins. Most IM-MS systems integrate the ion mobility device directly into the mass spectrometer or require extensively customized instrumentation. A new ion mobility device, the radial opposed migration ion and aerosol classifier (ROMIAC), developed by Mui and co-workers, is relatively simple to fabricate and easily integrated with the atmospheric pressure interface of most commercial mass spectrometers.[95] Chapter 6 details some of the initial studies performed using the ROMIAC. Specifically, the ROMIAC is used to separate isomer peptides as a demonstration of its utility in the analysis of complex peptide samples. In addition, the tagging of peptides with the FRIPS reagent is found to enhance peptide separation during IM-MS experiments.

Chapter 2

Probing the Chemistry of Ammonia at the Liquid/Vapor Interface: Base-Catalyzed Dissociation of a Cleavable Surfactant Studied by Field-Induced Droplet Ionization Mass Spectrometry

2.1 Abstract

The uptake of gaseous species into aqueous solutions is a central process in atmospheric chemistry that strongly influences the composition and processing of aerosol particles. Extensive research into the mechanism of uptake has revealed the complexity that often underlies this process. For example, the uptake of gas-phase ammonia at the liquid/vapor interface involves the interplay of accommodation, solvation, proton transfer, and diffusion. This study investigates the potential for changes in liquid properties near the liquid/vapor interface upon uptake of NH_3 to initiate base-catalyzed reactions selectively near a liquid surface. Droplets 2.5 µL in volume containing the pH-sensitive cleavable surfactant hexadecyl betaine (HDB) are exposed to gas-phase ammonia and sampled by field-induced droplet ionization mass spectrometry (FIDI-MS). Surfactant dissociation to yield hexadecanol and betaine in aqueous solutions or betaine methyl ester in solutions containing methanol is observed to occur without modulation of the bulk pH, suggesting that this process takes place selectively near the droplet surface. Sequential sampling experiments confirm that the reaction does not continue in the absence of gas-phase NH_3, providing further evidence that dissociation is not the result of changes in bulk solution pH. A model of NH_3 uptake coupled with reaction and diffusion indicates that transient

increases in pH may occur near the droplet surface, resulting in an increased rate of base-catalyzed dissociation in the interfacial region in comparison to bulk solution.

2.2 Introduction

The uptake of gaseous acids and bases at aqueous interfaces has received significant attention in both theoretical and experimental studies due to its importance in numerous atmospheric environments. These studies also provide insight into the fundamental properties and unique reactivity of the water/air interface, such as the acidity of the water surface[96-98] and the degree of solvation required for proton transfer reactions to occur.[99] Gas uptake at the water/air interface is hypothesized to proceed by the "critical cluster" model, in which surface accommodation is followed by the formation of a cluster of solvent molecules around the adsorbed species that facilitates its transfer into bulk solution.[20] For example, in the case of hydrochloric acid, a combination of theoretical and experimental studies has concluded that hydrolysis occurs at the interface or in the first few surface layers via the coordination of water molecules both above and below the hydrogen chloride molecule, resulting in efficient solvation of the ions and the formation of a stable ion pair.[49,99] Proton transfer to or from a base or acid generally occurs rapidly once the molecule is solvated, and this process occurs in concert with diffusion through the liquid to determine the time scale and spatial extent of pH change in solution.

The process of adsorption of gaseous ammonia (NH_3) at the water/air interface has been the subject of numerous studies, as NH_3 is the primary soluble base present in the earth's atmosphere. Studies employing SFG spectroscopy for the analysis of the structure of the interfacial region of ammonia-water solutions at high concentrations (mole fraction X_{NH_3}

> 0.1) found that ammonia-water complexes are present in the interfacial region, with the nitrogen lone pair of ammonia interacting with the free OH groups present at the liquid/vapor interface.[100,101] Similarly, surface tension measurements of ammonia-water solutions with X_{NH_3} between 0.01 and 0.1 found the Gibb's energy of adsorption of NH_3 to the liquid surface was nearly twice that of the bulk free energy of solvation.[102] Study of the uptake of ammonia by aqueous solutions as a function of pH using DTFR experiments found a mass accommodation coefficient (the fraction of gas collisions with a surface that result in uptake) between 0.08 at 290 K and 0.35 at 260 K.[103] Evidence for the formation of a surface complex involving ammonia was also observed at high pH values. Intriguingly, a study of the pH of the water/air interface following exposure to gaseous NH_3 found a measureable increase in the local pH at the surface that was sustained for several minutes before equilibration with the bulk liquid.[49]

The properties of ammonia at the liquid/vapor interface have also been investigated extensively by theoretical methods, yielding significantly different results depending on the methods employed (e.g., including or excluding polarizability, molecular dynamics vs. embedded quantum mechanical methods). Several studies found a potential minimum for ammonia at the liquid/vapor interface ranging in magnitude from 2-8 kJ/mol,[104-106] whereas other calculations found no evidence of a potential minimum.[107,108] Simulations of ammonia-water solutions showed evidence that NH_3 is concentrated at the interface, whereas NH_4^+ is depleted in the interfacial region.[105,109,110]

Although the adsorption of ammonia at the water/air interface has been the subject of many investigations, further experimental studies are required to yield insight into the

intriguing behavior of this molecule in the interfacial region. In this study, we explore the potential of NH_3 uptake at the liquid/vapor interface to initiate base-catalyzed reactions of surface-active species. A solution containing a cleavable surfactant, hexadecyl betaine (HDB, Scheme 2.1), is analyzed by forming a quiescent droplet with a surfactant layer of HDB at the water/air interface, exposing it to NH_3 vapor, and sampling by FIDI-MS. These experiments indicate that the uptake of gaseous ammonia by a liquid surface leads to a localized increase in pH, inducing based-catalyzed reactions specifically at the liquid/vapor interface. A simple model of NH_3 uptake at the water/air interface in concert with reaction and diffusion within a droplet provides further evidence for an increase in pH near the droplet surface.

Scheme 2.1. Base-Catalyzed Dissociation of the Cleavable Surfactant Hexadecyl Betaine (HDB)

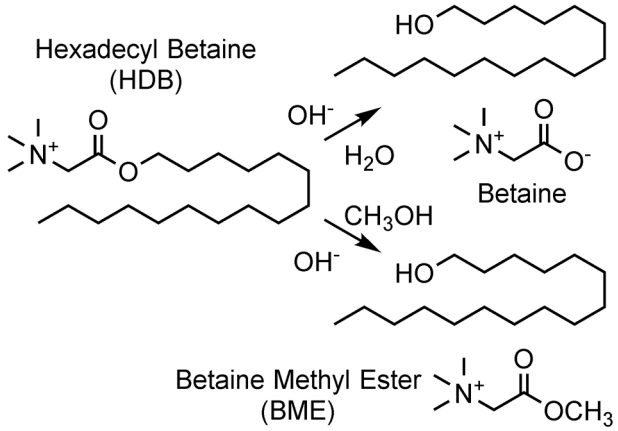

2.3 Materials and Methods

2.3.1 Materials

High-purity water was purchased from EMD Millipore (Billerica, MA). Ammonium acetate, concentrated ammonium hydroxide (28-30% by weight), and high-purity methanol

were obtained from J.T. Baker Avantor (Center Valley, PA). Hexadecyl betaine (2-(hexadecyloxy)-N,N,N-trimethyl-2-oxoethan-1-aminium chloride), dodecanoic acid, dodecyltrimethylammonium bromide (DTA), and ammonium bicarbonate were obtained from Sigma-Aldrich (St. Louis, MO) and used without further purification. New stock solutions of HDB were prepared daily at a concentration of 10 mM to prevent degradation. Stock solutions of 10 mM DTA and dodecanoic acid stored at −20° C and thawed for sample preparation. Hydrion short-range pH paper was obtained from Micro Essential Laboratory (Brooklyn, NY) to measure the pH of FIDI droplets following exposure to gaseous ammonia.

2.3.2 Field-Induced Droplet Ionization Mass Spectrometry (FIDI-MS)

Figure 2.1 shows the two experimental arrangements utilized for FIDI-MS experiments. The FIDI apparatus coupled to an LCQ mass spectrometer (Figure 2.1a) has been described in detail in a prior study,[83] and slight modifications to this design were implemented to couple the source to an LTQ-XL mass spectrometer (Thermo-Fisher, Waltham, MA), as shown in Figure 2.1b. In both designs, a droplet of ~1.6 mm in diameter (2.5 μL volume) is formed on the end of a 28-gauge stainless steel capillary by injection from an external syringe pump. This capillary is positioned equidistantly between two parallel plate electrodes separated by 6.3 mm. Following a 1 min delay period for droplet equilibration and formation of a surface surfactant layer, NH_3 vapor is leaked into the region via two gas inlets on either side of the droplet. The gas flow is maintained for a variable period of time up to 60 s, and the droplet is then subjected to a strong electric field by application of a high voltage to the back parallel plate electrode; the metal capillary on which the droplet

is hanging is also biased such that it is on an equipotential of the applied field. The strong electric field results in the ejection of highly charged, micron-sized progeny droplets,[85] which enter the atmospheric pressure inlet of the mass spectrometer and undergo evaporation and Rayleigh discharge to yield gas-phase ions in a manner similar to the mechanism of electrospray ionization.[111] The FIDI source designed for the LCQ (Figure 2.1a) employs a copper mesh as the high voltage electrode and the inlet of the mass spectrometer as the ground electrode. The FIDI source modified for use with the LTQ-XL (Figure 2.1b) utilizes two stainless steel plates mounted on ceramic rods (Kimball Physics, Wilton, NH) as the high voltage and ground electrodes. Experiments on droplets of 50/50% (v/v) methanol/water were performed with use of the LCQ, and those on purely aqueous droplets were performed with use of the LTQ. For each time point, at least four spectra were collected from separate droplets and averaged to give the presented time-resolved data. Following sampling by FIDI-MS, each droplet was collected on short-range pH paper (range 5.5-8.0, increments of 0.3 pH units), and the pH was determined by noting the change in color of the paper.

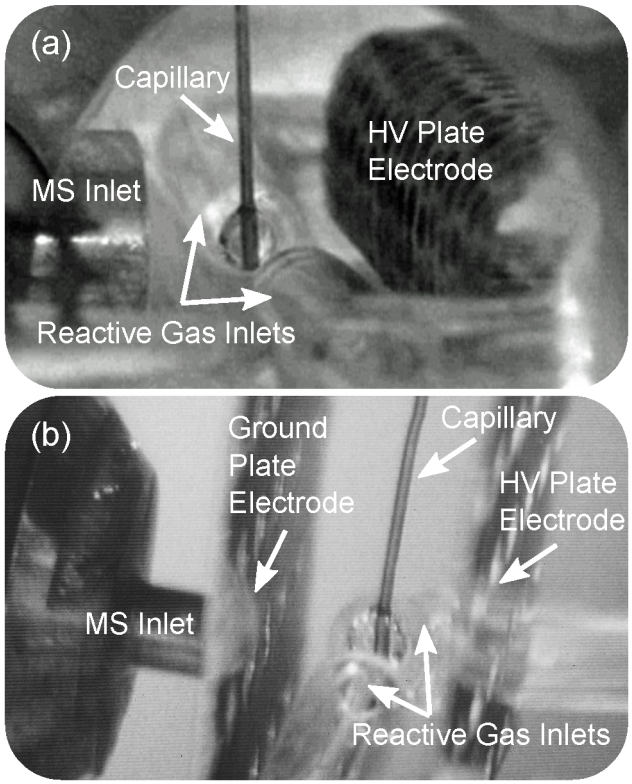

Figure 2.1. Experimental apparatus for monitoring interfacial reactions by FIDI-MS. Experiments performed with the LCQ mass spectrometer (a) utilized a copper mesh for the high voltage (HV) electrode and the MS inlet as a ground electrode, whereas experiments performed with the LTQ mass spectrometer (b) utilized stainless steel plates for the ground and HV electrodes.

2.3.3 Generation of Gaseous Ammonia

Two approaches were utilized to generate a flow of gaseous ammonia for droplet exposure. For experiments on droplets of 50/50% (v/v) methanol/water, a 32 mL/min flow of nitrogen was directed over the headspace above 3 mL of a ~150 mM ammonium hydroxide solution in the base of a U-shaped flow tube. For experiments on aqueous droplets, nitrogen gas was flowed through a fritted bubbler (64834-U, Sigma-Aldrich) containing 10 mL of 15 mM ammonium hydroxide at a rate of 50 mL/min. Gas flow rates were governed by a mass flow controller calibrated for nitrogen (πMFC, MKS Instruments,

Andover, MA). Flow rates and concentrations were optimized to ensure that the gas flow did not induce major changes in the bulk pH of droplets.

2.3.4 Sonic Spray Ionization

A sonic spray ionization (SSI) source was utilized in this work to study the kinetics of hydrolysis of HDB in buffered aqueous solution. The apparatus is constructed from a 1/16 in. tubing tee (Swagelok, Solon, OH) as described in detail in a previous study by Cooks and co-workers.[112] The source was operated with a nitrogen nebulizing gas flow rate of ~5 L/min and a sample infusion rate of 5 µL/min. An LTQ-XL was utilized for detection with the same instrumental parameters employed in FIDI-MS experiments to minimize differences in ion abundance between the two methods. Solutions of 100 µM HDB in either 50 mM ammonium bicarbonate or 25 mM ammonium acetate with pH adjusted by addition of acetic acid or ammonium hydroxide were prepared directly prior to analysis.

2.3.5 Model of NH_3 Uptake in Aqueous Solution

To better evaluate the interplay of uptake, diffusion, and reaction in these experiments, a simple model was developed to study the uptake of NH_3 vapor by aqueous droplets. The experimental system is modeled as a spherically symmetric droplet 1 mm in diameter. The Nernst-Planck diffusion model in the dimension r over time t is utilized to describe the movement of dissolved species in solution,[113-116]

$$\frac{\partial c_i}{\partial t} = r^{-2}\frac{\partial}{\partial r}\left[r^2\left(\sum_{k=1}^{N_s} D_{ik}\frac{\partial c_k}{\partial r}\right)\right] + j_i \qquad (2.1)$$

where c_i is the concentration of each species, N_s is the number of species, and j_i represents the rate of addition or depletion of a species via chemical reaction. The diffusion coefficient

of species i modified by the concentration gradient of other dissolved species k, represented by D_{ik}, is given by

$$D_{ik} = D_i \delta_{ik} - \frac{z_i z_k D_i D_k c_i}{\sum_{k=1}^{N_s} z_k^2 D_k c_k} \quad (2.2)$$

where D_i is the diffusion coefficient of species i, δ_{ik} is the Kronecker delta function, and z_i is the charge of species i. This model accounts for the influence of electrostatic interactions on diffusion in the droplet. The diffusion constants utilized for each species are detailed in Table B.1.

In each simulation, the proton transfer reactions of ammonia were modeled along with the reactions of dissolved carbon dioxide,

$$\mathrm{NH_3 + H_2O \rightleftharpoons NH_4^+ + OH^-} \quad (2.3)$$

$$\mathrm{NH_3 + H_3O^+ \rightleftharpoons NH_4^+ + H_2O} \quad (2.4)$$

$$\mathrm{2\ H_2O \rightleftharpoons H_3O^+ + OH^-} \quad (2.5)$$

$$\mathrm{CO_2 + H_2O \rightleftharpoons H_2CO_3} \quad (2.6)$$

$$\mathrm{H_2CO_3 + H_2O \rightleftharpoons HCO_3^- + H_3O^+} \quad (2.7)$$

$$\mathrm{HCO_3^- + OH^- \rightleftharpoons CO_3^{2-} + H_2O} \quad (2.8)$$

The rate constants for the forward and reverse reactions used in the model are listed in Table B.2.

The initial conditions of the simulation are calculated assuming a pure water droplet in equilibrium with 400 parts per million (ppm) gas-phase CO_2 and no dissolved NH_3, giving a uniform initial droplet pH of 5.6, as detailed in Table B.3. The system boundary conditions are modeled by[103,117]

$$\frac{\partial c_i(r=0)}{\partial r} = 0 \tag{2.9}$$

$$\frac{\partial c_i(r=0.5)}{\partial x} = \left(\frac{\alpha_i}{D_{i,\,\mathrm{H_2O}}\sqrt{2\pi M_i RT}}\right)\left(P_{i,g} - \frac{c_i(r=0.5)}{H_i}\right) \tag{2.10}$$

where α_i is the mass accommodation coefficient of species i, M_i is the molar mass, R is the gas constant, T is the temperature (K), $P_{i,g}$ is the gas-phase pressure (Pa), and H_i is the Henry's law constant (mol Pa^{-1} m^{-3}), as given in Table B.4. Physically, these conditions correspond to analyte uptake at the liquid surface that is a function of the diffusion constant in solution ($D_{i,\,\mathrm{H_2O}}$), the number of gas-phase molecules impinging upon the surface ($\sqrt{2\pi M_i RT}$),[20] the fraction of impinging molecules adsorbed by the solution (α_i), and the difference between the gas-phase analyte partial pressure ($P_{i,g}$) and the equilibrium vapor pressure above the solution ($c_i(r = 0.5)/H_i$). The gas-phase pressure of all species except NH_3 and CO_2 are assumed to be zero (i.e., $\partial c_i(r = 0.5)/\,\partial r = 0$). The effect of a gas-phase concentration gradient induced as a result of uptake into the liquid, the preference of molecules for the interfacial region, and the convective transport of analytes are not modeled in this simplified system. Calculations were performed using the *pdepe* function in the MATLAB programming environment (MathWorks, Natick, MA).

2.4 Results and Discussion

2.4.1 Kinetics of HDB Hydrolysis Monitored by SSI

As shown in Scheme 2.1, the ester bond of HDB hydrolyzes under basic conditions via nucleophilic attack at the carbonyl by a hydroxide ion to yield hexadecanol and betaine. In the presence of methanol, betaine methyl ester (BME) is also formed in high yield. To

assess the kinetics of HDB hydrolysis, the reaction in buffered aqueous solution was monitored at pH 7, 8, and 9 by sonic spray ionization (SSI), as shown in Figure 2.2. Although SSI does not yield quantitative ion intensities due to preferential ionization phenomena common in spray ionization techniques,[111] SSI can be utilized to qualitatively assess the hydrolysis kinetics of HDB. Little dissociation of HDB was observed at pH 7 after 40 minutes, whereas half-lives of approximately 22 and 2 minutes were determined at pH 8 and 9, respectively. Strong agreement was obtained between experiments utilizing 50 mM ammonium bicarbonate and 25 mM ammonium acetate as buffers. These results indicate a strong pH dependence for dissociation of betaine ester surfactants, in agreement with a prior study.[118]

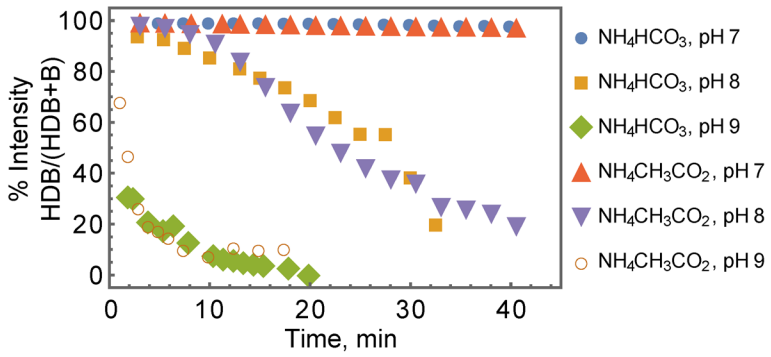

Figure 2.2. Dissociation of hexadecyl betaine (HDB) to betaine (B) at pH 7, 8, and 9. Plotted is the % intensity of HDB divided by the total intensity of betaine and HDB monitored by SSI-MS as a function of time. Solutions were prepared in either 50 mM NH_4HCO_3 or 25 mM $NH_4CH_3CO_2$ with pH adjustment by addition of acetic acid or ammonium hydroxide.

2.4.2 Investigation of NH_3-Catalyzed Reactions at the Water Surface

FIDI-MS studies of reaction at the liquid/vapor interface upon NH_3 uptake were performed in water alone and in water/methanol mixtures. Water/methanol (50/50% v/v) droplets of 2.5 µL in volume containing 100 µM HDB were exposed to a flow of gaseous NH_3 generated by a flow of nitrogen above a 150 mM NH_4OH solution at a rate of 32 mL/min for 0-60 s. Although the gas flow contains a significant concentration of NH_3, the flow is diluted upon exit from the reactive gas inlets, as the pull of air into the adjacent mass spectrometer inlet is approximately 1 L/min, resulting in a much higher flow of laboratory air in the vicinity of the droplet. Measurement of droplet pH following exposure to gaseous NH_3 using sensitive pH paper did not show a significant increase in the bulk pH of the droplets ($pH \leq 6.4$). Figure 2.3a shows the results of NH_3 exposure experiments for 50/50% (v/v) water/methanol droplets containing 100 µM HDB. Over the course of 60 s of exposure, the relative intensity of HDB is greatly reduced, and the product betaine methyl ester (BME) is observed with high intensity. The efficiency of this reaction without a significant change in the bulk pH suggests that this reaction occurs as a result of processes unique to the water/air interface.

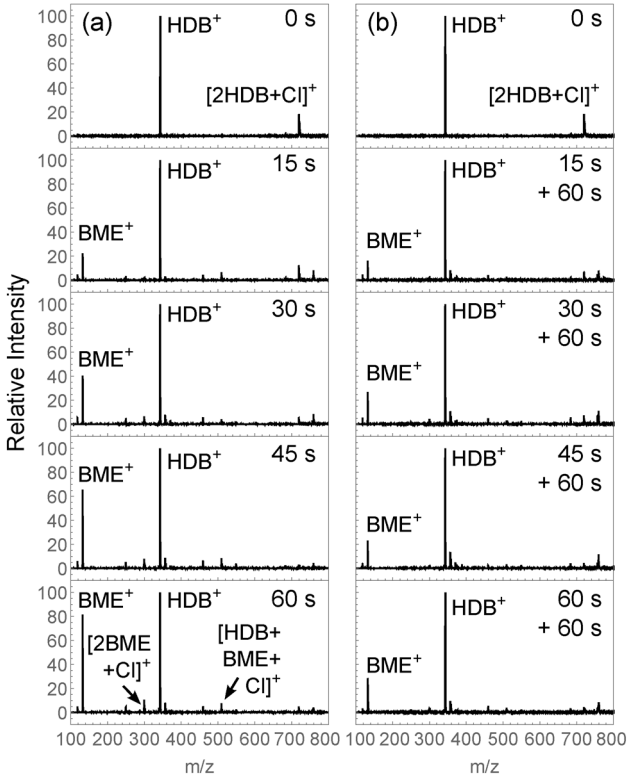

Figure 2.3. Exposure of aqueous HDB to ammonia vapors; (a) 100 μM HDB in 50/50 water/methanol is exposed to ammonia vapors at a flow rate of 32 mL/min; (b) 60 s after the initial FIDI sampling, each droplet is sampled a second time, and the results suggest diffusion of the product BME, significantly more hydrophilic than HDB, into solution.

If the dissociation of HDB occurs selectively at the liquid/vapor interface, then the reaction should cease in the absence of gaseous NH_3, and the BME product, which is hydrophilic and unlikely to localize to the droplet surface, should diffuse into solution until it reaches an equilibrium concentration throughout the droplet volume. Assuming that the diffusion coefficient of BME is similar to that of betaine ($\sim 1 \times 10^{-5}$ cm^2 s^{-1})[119], a substantial decrease in BME concentration near the liquid surface should be observed within 60 s in the case of an interfacial process. To probe this hypothesis, each droplet was sampled a second time by FIDI-MS following 60 s of equilibration with the reactive gas flow shut

off, yielding the spectra shown in Figure 2.3b. At short times (15-30 s of gas exposure), little difference in the intensity of BME is observed following the equilibration period. This result alone is significant, as it indicates that the reaction is not driven by a change in bulk pH, which would cause hydrolysis to continue in the absence of gaseous NH_3. At longer time points (45-60 s of gas exposure), there are clear differences in the relative abundance of BME. At these later exposure times, there is significantly more of the hydrolysis product BME at the interface, and the diffusion away from the surface is therefore more rapid and noticeable. Notably, the diffusion of products from the interface may be somewhat aided by the mixing of the droplet as a result of the first FIDI sampling, but the observation that BME does not increase in intensity following NH_3 exposure suggests the reaction occurs selectively near the droplet surface.

Dissociation of dissolved HDB upon exposure to gaseous NH_3 was also investigated in purely aqueous solution. Since hydrolysis of HDB produces hexadecanol (Scheme 2.1), which is highly insoluble in water, the concentration of HDB was reduced to 50 µM. Higher concentrations were observed to lead to loss of droplets from the capillary due to a decrease in surface tension, likely as a result of substantial concentrations of hexadecanol at the droplet surface. In addition, the zwitterionic betaine product generated in aqueous solution is challenging to detect by FIDI-MS, especially in comparison to the highly surface-active HDB parent ion, and the loss of HDB was therefore monitored with respect to the nonreactive dodecytrimethylammonium ion (DTA), added at a concentration of 7.5 µM. Dodecanoic acid was also added to the sample at a concentration of 100 µM to decrease the surface tension of the aqueous sample and therefore allow for FIDI-MS sampling.

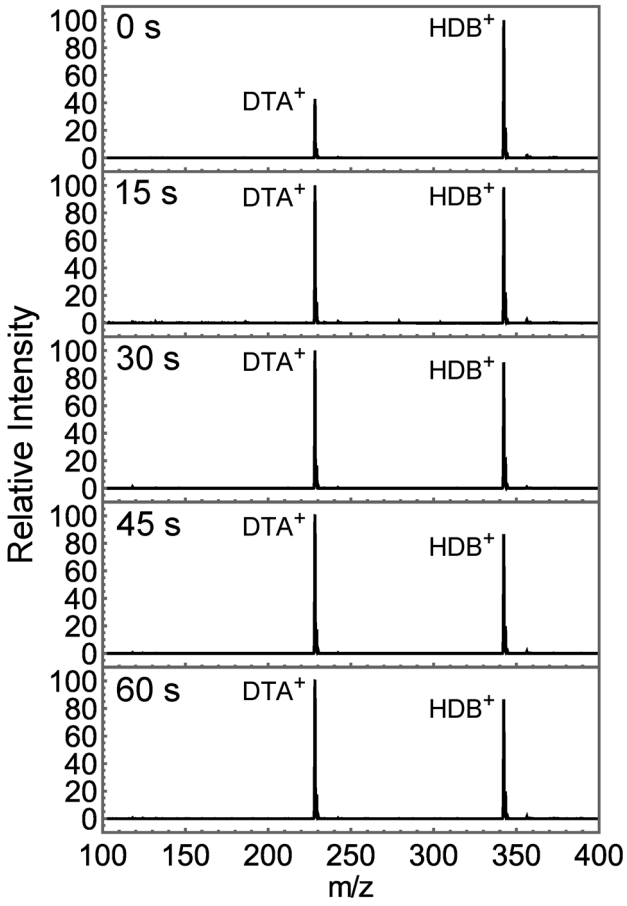

Figure 2.4. FIDI-MS of aqueous HDB solutions exposed to NH_3. Samples of 50 μM HDB, 100 μM DDA, and 7.5 μM DTA were exposed to gas-phase NH_3 generated by a flow of 50 mL/min of N_2 through a fritted bubbler containing 10 mL of 15 mM NH_4OH. The relative intensity of HDB with respect to DTA decreases rapidly in the first 15 s and then slowly thereafter.

The FIDI-MS spectra collected following the exposure of aqueous HDB to NH_3 are shown in Figure 2.4. Over the course of 60 s of exposure, the relative intensity of HDB with respect to DTA is found to decrease significantly, with the most substantial change occurring in the first 15 s of NH_3 exposure. The bulk pH of the droplet was also measured following each experiment and was not found to increase substantially ($pH \leq 6.4$). As in the water/methanol solutions, these results suggest that the dissociation of the surfactant at

the liquid/vapor interface is not initiated by a change in the bulk pH but rather by a base-catalyzed reaction specific to the interface.

2.4.3 Mechanism for an Enhanced Dissociation Rate at the Interface

A theoretical model of ammonia uptake coupled with diffusion and reaction in aqueous solution was developed to complement the experimental observations of base-catalyzed reactions at the liquid/vapor interface. The model accounts for the presence of dissolved carbonic acid in equilibrium with gas-phase CO_2 and monitors the concentration of analytes throughout a droplet of radius 0.5 mm following uptake of NH_3 at the water/air interface for 0-60 s. Shown in Figure 2.5 are the calculated pH values in solution for varying gas-phase concentrations of NH_3. At a gas-phase NH_3 concentration of 1×10^{10} molecules cm^{-3} (Figure 2.5a), an increase of pH from 5.6 to 6.7 near the surface of the droplet is calculated without a large change in the bulk pH of solution. This effect is even more pronounced for a gas-phase concentration of 1×10^{11} molecules cm^{-3} (Figure 2.5b), which yields an increase in surface pH to 7.6 compared to a bulk pH increase from 5.6 to 6.5. The pH near the surface remains above 7 throughout the 60 s modeling time. At higher concentrations of gas-phase NH_3 (1×10^{12} molecules cm^{-3}, Figure 2.5c), a large increase in the pH near the surface is also observed, but the pH in bulk solution is rapidly increased to greater than 7.

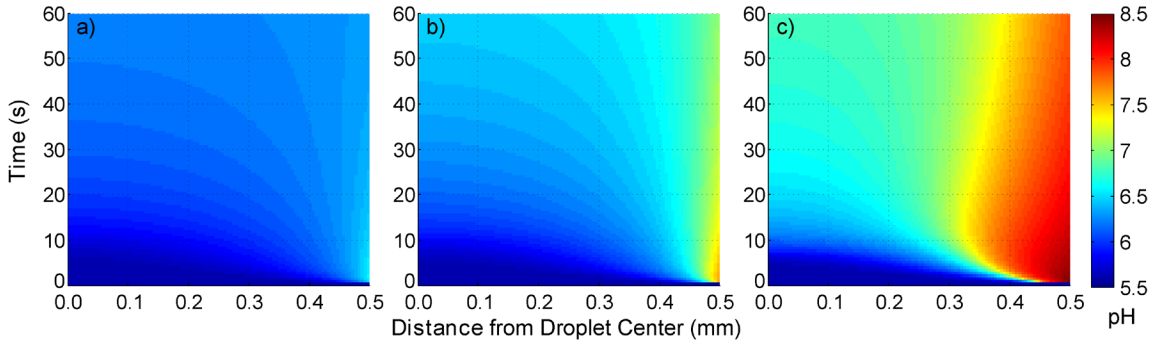

Figure 2.5. Modeling of uptake, reaction, and diffusion of ammonia within an aqueous droplet of 0.5 mm radius in equilibrium with gaseous carbon dioxide; plotted is the pH as a function of depth over sixty seconds of exposure to gas-phase NH_3 at a concentration of (a) 1×10^{10}, (b) 1×10^{11}, and (c) 1×10^{12} molecules cm^{-3}.

The modeled transient change in pH near the droplet surface occurs as a result of the difference between the reaction rate of ammonia with water to yield the hydroxide ion and the rate of conversion of dissolved carbon dioxide to carbonic acid, which acts as a buffer to maintain the initial pH of the solution. As NH_3 enters the liquid, it reacts quickly with water to increase the pH locally according to reactions 2.3 and 2.4 ($k_{2.3forward}$= 5.0×10^5 s^{-1}, $k_{2.4forward}$ = 4.3×10^{10} M^{-1} s^{-1}).[120,121] The depth at which this reaction occurs is limited by the diffusion rate of the ammonia within the droplet. As the concentration of the hydroxide ion increases, the rate of reaction between the bicarbonate and hydroxide ions also increases, regulating the increase in pH by reaction 2.8. The bicarbonate is quickly replenished by the reaction of carbonic acid with water (reaction 2.7). However, once the carbonic acid is depleted, the local buffering capacity of the liquid is limited by the rate of conversion of dissolved carbon dioxide to carbonic acid (reaction 2.6), a significantly slower process ($k_{2.6forward}$ = 0.04 s^{-1}).[122] Eventually, the concentrations of CO_2 (aq) and dissolved carbonic acid reach equilibrium once again, resulting in a buffering effect that

prevents a significant increase in droplet pH at the equilibrium concentration of dissolved NH_3. Nevertheless, an interfacial pH increase is still observed due to the transient increase in hydroxide ion concentration that occurs much more quickly than the replenishment of the buffering species. This result supports the experimental observation that dissociation of a base-cleavable surfactant can be achieved in an aqueous droplet without an increase in bulk pH.

The increase in dissociation of HDB detected experimentally may also be the result of processes occurring at the droplet surface by the formation of an ammonia surface complex. Ammonia is known to be enriched in concentration at the water/air interface in comparison to bulk solution at high concentrations.[100,101] Donaldson experimentally measured the Gibb's energy of adsorption to the surface to be −19.1 kJ/mol, as compared to a bulk free energy of solvation of −10.1 kJ/mol.[102] Shi and co-workers also found kinetic evidence for the formation of a surface complex of NH_3 during uptake from the gas phase, although such complexes were only observed at high pH.[103] A study by Clifford and Donaldson observed that the pH at the surface of liquid water exposed to gas-phase NH_3 could exist in disequilibrium with bulk solution for several minutes, but the differential was only on the order of 0.1 pH units.[49] However, a similar phenomenon may be present in these experiments, resulting in an increased rate of dissociation at the surface.

2.5 Conclusions

The process of uptake of NH_3 at the water/air interface has been investigated in depth previously by both theoretical and experimental studies. These studies have greatly enhanced the current understanding of the uptake process, establishing that uptake

proceeds by critical cluster formation,[63,102] indicating the presence of a thermodynamic minimum at the interface,[102] and constraining the mass accommodation coefficient.[103,123] However, further investigation is necessary to fully comprehend the complex interplay of adsorption, diffusion, and proton transfer reactions occurring in the interfacial region. This study utilizes the model system of a base-cleavable surfactant enriched in concentration at a liquid surface to demonstrate that base-catalyzed reactions can occur specifically at the liquid/vapor interface as a result of exposure to NH_3. Such reactions are observed to occur on droplet surfaces without significant modulation of the bulk solution pH, and multi-sampling FIDI-MS experiments suggest that the reactions do not continue upon cessation of base exposure, supporting the assertion that these reactions occur specifically in the interfacial region. A simple model of uptake coupled with diffusion suggests that a transient increase in pH near the liquid surface can occur upon exposure to gas-phase NH_3. A similar phenomenon has also been observed previously by Clifford and Donaldson.[49] Additional experimental and theoretical studies are required to fully elucidate the process of interfacial uptake, but these results demonstrate the ability of FIDI-MS to investigate novel processes occurring at interfaces that may have otherwise been inaccessible.

Chapter 3

Real-Time Studies of Iron Oxalate-Mediated Oxidation of Glycolaldehyde as a Model for Photochemical Aging of Aqueous Tropospheric Aerosols

3.1 Abstract

The complexation of iron (III) with oxalic acid in aqueous solution yields a strongly absorbing chromophore that undergoes photodissociation with high quantum yield to give iron (II) and the carbon dioxide anion radical. Importantly, this complex absorbs near-UV radiation ($\lambda > 350$ nm), making it a potentially powerful source of oxidants in aqueous tropospheric chemistry. Although this photochemical system has been studied for several decades, the mechanistic details associated with its role in the oxidation of dissolved organic matter within cloud water, fog, and aqueous aerosol remain largely unknown. This study utilizes glycolaldehyde as a model organic species to study the oxidation pathways and evolution of organic aerosol initiated by the photodissociation of aqueous iron (III) oxalate complexes. Hanging droplets (radius 1 mm) containing iron (III), oxalic acid, glycolaldehyde, and ammonium sulfate (pH ~ 3) are exposed to irradiation at 365 nm and sampled at discrete time points utilizing field-induced droplet ionization mass spectrometry (FIDI-MS). Glycolaldehyde is found to undergo rapid oxidation to form glyoxal, glycolic acid, and glyoxylic acid, but the formation of high-molecular-weight oligomers is not observed. These results suggest that photodissociation of iron (III) oxalate can lead to the formation of volatile oxidation products in tropospheric aqueous aerosol.

3.2 Introduction

Tropospheric aqueous-phase chemistry plays a key role in the aging of dissolved organics in the atmosphere.[4-6,124,125] Aqueous phase processing may occur as a result of "dark" reactions such as acid catalysis, hydration, and oligomerization,[126,127] or they may result from photochemical excitation of dissolved light-absorbing species.[128-130] One of the key components directing the aging of dissolved organics is the availability of oxidative species such as the hydroxyl radical (OH) and hydrogen peroxide (H_2O_2), which may be present by direct generation in solution or by uptake from the gas phase.[131] Many laboratory studies have investigated SOA production initiated by photolysis of dissolved H_2O_2.[132-135] There is increasing evidence, however, that processes involving the photolysis of photoactive organic and organometallic compounds may also be important sources of highly reactive aqueous oxidants.[129,136-138]

Transition metal ions present in cloudwater or aqueous aerosol are known to undergo photo-initiated electron transfer processes that can be a significant source of oxidative species.[6,90,139] Iron, the most abundant transition metal ion in tropospheric particles, can be found in aerosol originating from sea spray,[140] mineral dust,[90] and anthroprogenic emissions.[93] Measured concentrations of iron in fog waters range from micromolar or less in rural areas to tens of micromolar in highly polluted environments.[141] As a result of these substantial concentrations, iron can play an important role in the aqueous-phase tropospheric oxidation of organics. The reactions of dissolved iron-hydroxy complexes, or the Fenton reactions, are a well-characterized source of atmospheric oxidants.[91,92,142] The direct reaction of hydrogen peroxide with iron (II) yields hydroxyl radicals in the dark

Fenton reaction (3.1), whereas the photo-Fenton reaction yields hydroxyl radicals by photolysis of the iron (III) hydroxy complex (3.2 and 3.3).

$$Fe^{2+} + H_2O_2 \rightarrow Fe^{3+} + OH^{\bullet} + OH^{-} \quad (3.1)$$

$$Fe^{3+} + 2H_2O \rightleftharpoons Fe(OH)^{2+} + H_3O^{+} \quad (3.2)$$

$$Fe(OH)^{2+} \xrightarrow{h\nu} Fe^{3+} + OH^{\bullet} \quad (3.3)$$

Several groups have recently explored the impact of iron photochemistry on SOA formation. Chu and co-workers studied the effects of iron (II) sulfate and iron (III) sulfate seed aerosol on SOA formation at 50% RH and found that iron (II) complexes inhibited SOA formation, whereas iron (III) had little effect on SOA formation.[143] They attributed the effect of iron (II) to the reduction of organic condensate by the iron species and subsequent disruption of oligomerization processes. Nguyen and co-workers investigated the uptake and oxidation of glycolaldehyde in aqueous aerosol containing hydrogen peroxide and iron complexes.[91] They found that the photo-Fenton reaction significantly increased the degree of oxidation in aerosol particles when compared with H_2O_2 photolysis alone (ratio of O/C=0.9 with iron and H_2O_2 vs. O/C=0.5 with H_2O_2).

Although laboratory experiments have demonstrated that photo-Fenton chemistry can lead to significant oxidation of organics,[144-146] the role of such processes in ambient aerosol is not clear, as the reactions are highly dependent on pH, iron concentration, and the concentration of other ligands that readily complex with iron.[92,147,148] Notably, the formation of stable complexes between iron and dicarboxylate ligands can have a significant impact on the photochemical reaction pathways. Complexation between the oxalate anion, one of the most abundant low-molecular weight organic compounds found

in aqueous aerosol,[93,149-151] and iron has long been known to generate significant yields of oxidative species by photochemical reduction of iron. Initially studied as a chemical actinometer,[152,153] seminal work by Zuo and Hoigné demonstrated that photolysis of iron oxalate complexes could lead to the generation of oxidative species under atmospherically relevant conditions.[92]

The proposed pathway for the photochemical generation of oxidative species from iron (III) oxalate complexes is shown in reactions 3.4-3.10 below. Depending on the pH, ionic strength, and concentration of iron and oxalate, three complexes are formed: $Fe(C_2O_4)^+$, which has low photochemical reactivity,[154] and $Fe(C_2O_4)_2^-$ and $Fe(C_2O_4)_3^{3-}$, both of which undergo photochemical reduction of iron with high quantum yield.[147,155] The mechanism of photochemical dissociation of $Fe(C_2O_4)_3^{3-}$ has been investigated in detail, with two groups presenting evidence for either intermolecular electron transfer (3.4a) or intramolecular electron transfer (3.4b) as the primary reaction pathway.[156-159] The mechanism of dissociation of $Fe(C_2O_4)_2^-$ has not been studied extensively but is also expected to yield the oxalate anion radical, which rapidly dissociates to CO_2 and $CO_2^{\bullet-}$ (reactions 3.5 and 3.6).[92] The subsequent reaction of $CO_2^{\bullet-}$ with O_2 leads to the eventual formation of H_2O_2 (reactions 3.7-3.9), which can then interact directly with Fe^{2+} (reaction 1) or with FeC_2O_4 (reaction 3.10) to produce OH.[160]

$$Fe(C_2O_4)_3^{3-} \xrightarrow{h\nu} Fe(C_2O_4)_2^{2-} + C_2O_4^{\bullet-} \quad (3.4a)$$

$$Fe(C_2O_4)_3^{2-} \xrightarrow{h\nu} Fe(C_2O_4)_2^{-} + 2CO_2^{\bullet-} \quad (3.4b)$$

$$Fe(C_2O_4)_2^{-} \xrightarrow{h\nu} Fe^{2+} + C_2O_4^{2-} + C_2O_4^{\bullet-} \quad (3.5)$$

$$C_2O_4^{\bullet-} \rightarrow CO_2^{\bullet-} + CO_2 \quad (3.6)$$

$$CO_2^{\bullet-} + O_2 \rightarrow CO_2 + O_2^{\bullet-} \quad (3.7)$$

$$O_2^{\bullet-} + H_3O^+ \rightarrow HO_2^{\bullet} + H_2O \quad (3.8)$$

$$2HO_2^{\bullet} \rightarrow H_2O_2 + O_2 \quad (3.9)$$

$$FeC_2O_4 + H_2O_2 \rightarrow FeC_2O_4^+ + OH^{\bullet} + OH^- \quad (3.10)$$

Although the mechanism and kinetics of dissociation of iron (III) oxalate complexes have been examined in detail, much less information is available on the oxidation of atmospherically relevant compounds by this photochemical system. Zuo and Zhan found that the presence of iron (III) oxalate complexes increases the rate of oxidation of sulfur dioxide compared to iron alone under atmospherically relevant conditions.[161] In field sampling studies, Sorooshian et al. found an inverse correlation between concentrations of dissolved iron and oxalate in stratocumulus cloudwater above the northeastern pacific ocean, suggesting that ferrioxalate photochemistry may play an important role in determining cloudwater composition under certain conditions.[93] These studies serve as initial demonstrations of the potential importance of such reactions in aqueous tropospheric chemistry, but further laboratory and field studies are necessary to better discern the complex interplay of reactions influencing the oxidation of dissolved organic compounds.

Glycolaldehyde serves as an excellent model system to study the influence of liquid-phase ferrioxalate photochemistry on the oxidation of dissolved organics. A major product of isoprene oxidation, glycolaldehyde is produced with an estimated global flux of greater than 42 Tg C yr^{-1}.[133,162,163] The abundance of glycolaldehyde, along with its high solubility,[164] means that its oxidation processes may play a significant role in the formation of SOA in aqueous aerosol.

This study explores the photochemically initiated reaction pathways involved in the oxidation of aqueous glycolaldehyde in the presence of ferrioxalate complexes. Real-time studies of photochemical reactions in microliter droplets utilizing field-induced droplet ionization mass spectrometry (FIDI-MS)[83,84] provide insight into the changes in chemical composition of this model system upon UV irradiation.

3.3 Materials and Methods

3.3.1 Materials

High-purity water and ACS-grade sulfuric acid were obtained from EMD Millipore (Billerica, MA). Concentrated ammonium hydroxide (28-30% by weight) and ACS-grade iron (iii) chloride 6-hydrate were obtained from J.T. Baker Avantor (Center Valley, PA). All other chemicals were purchased from Sigma-Aldrich (St. Louis, MO). Stock solutions were prepared in concentrations of 10-100 mM and stored at −20° C with the exception of iron (iii) chloride stock solutions, which were prepared fresh daily at a concentration of 50 mM in a 5 mM solution of H_2SO_4.

3.3.2 Field-Induced Droplet Ionization Mass Spectrometry

The FIDI-MS source employed in this study is based upon an initial design described by Grimm and co-workers.[83] The general design and features of the updated source are described here, with further details given in Appendix A. A hanging droplet of 1.5-2 mm in diameter (2-4 µL) is suspended on the end of a stainless steel capillary between two parallel plate electrodes separated by 6.3 mm (Figure 3.1c). The parallel plates are mounted to a translation stage to allow alignment of an aperture in the electrically grounded plate with the atmospheric pressure inlet of an LTQ-XL mass spectrometer (Thermo-Fisher,

Waltham, MA). The capillary is mounted on a separate translation stage to provide for placement of the droplet midway between the two plates in alignment with the inlet of the LTQ-XL. A droplet is formed from liquid fed through the capillary using a computer-controlled motorized syringe pump. Mass spectrometric sampling of the hanging droplet is accomplished by application of a pulsed high voltage (typically 3-5 kV, 100 ms duration) to the back parallel plate and to the suspended capillary at half the magnitude applied to the back plate to maintain field homogeneity between the front and back plate. When a sufficiently high voltage is applied, the electrical forces overcome the surface tension of the droplet, resulting in the bipolar ejection of highly-charged progeny droplets of less than 1 μm in diameter from the opposite ends of the suspended droplet.[84,85] Charged droplets of a specific polarity enter the transfer capillary of the mass spectrometer, resulting in the detection of gas-phase ions in a manner similar to electrospray ionization.[111] Sampling of either positive or negative ions is achieved by switching the polarity of the high voltage applied to the back plate and capillary. The pulsed high voltage is controlled by a custom power supply and LabView software described elsewhere.[165]

The entire FIDI source is mounted within a custom enclosure that provides control of the environment in which the droplet is suspended, as shown in Figure 3.1a,b. The enclosure is equipped with a fused silica window to allow for the study of photochemical reactions and for visual droplet monitoring during experiments. To study the photochemistry of suspended droplets in the absence of oxygen, the chamber was flushed with nitrogen at a flow rate of 1.2 L/min for ~10 minutes prior to sampling, and the flow of nitrogen was maintained throughout the experiment; the sample was also degassed by bubbling with nitrogen. For all other experiments undertaken in this work, the enclosure was left open to

laboratory air. Photochemical reactions in the hanging droplet are accomplished by irradiation with 365 nm light with a radiant flux of approximately 5 mW generated by a fiber optic-coupled LED (FCS-0365-000, Mightex Systems, Pleasanton, CA). The light is focused onto the droplet using a collimating lens (74-UV, Ocean Optics, Dunedin, FL) and a spherical focusing lens. Based upon the estimated focal spot size (3 mm radius), the droplet size (1 mm radius), and the estimated radiant flux based on manufacturer ratings, the photon flux encountering the hanging droplet is estimated to be 3×10^{16} photons cm^{-2} s^{-1}, approximately two orders of magnitude greater than the solar actinic flux at 365 nm with a 30° solar zenith angle.[166]

Photochemical experiments employing FIDI-MS were performed in solutions containing 0.5 mM H_2SO_4, 100 µM NH_3, 50 µM $FeCl_3$, 250 µM oxalic acid, and 250 µM glycolaldehyde. Control experiments were also performed by excluding iron, oxalic acid, or glycolaldehyde from the mixture and observing the impact on the photochemistry. In a typical experiment, a droplet of the solution was formed on the end of the capillary and allowed to rest for 1 minute prior to exposure to 365 nm radiation. Individual droplets were then sampled by application of a high voltage pulse after 0, 1, 2, and 3 min of irradiation. The presented spectra are averaged from four experiments on discrete droplets at each time point. Between experiments, the sample line was rinsed thoroughly with 10 mM H_2SO_4 and was also allowed to soak overnight in this solution to prevent the accumulation of iron precipitates.

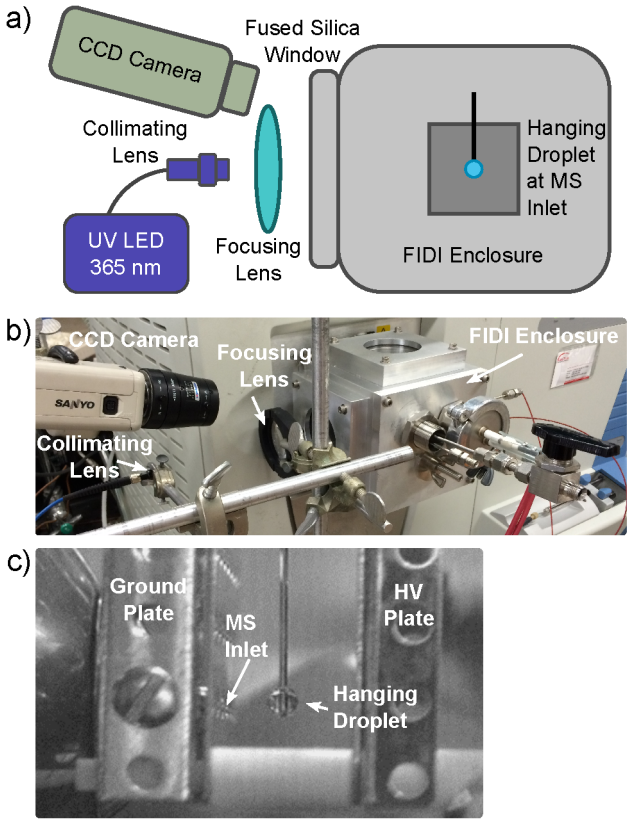

Figure 3.1. Experimental apparatus for studying photochemistry utilizing FIDI-MS. The primary components of the system are depicted schematically in (a) and shown as utilized in the laboratory in (b). A CCD camera image of the FIDI region is shown in (c).

3.4 Results and Discussion

3.4.1 Oxidation of Glycolaldehyde by Iron (III) Oxalate Photochemistry

Figure 3.2 shows the FIDI-MS spectra of hanging droplets containing iron (III) oxalate complexes and glycolaldehyde exposed to irradiation at 365 nm for 0-3 minutes. The HSO_4^- anion and its dimer are the most prominent ions in the spectrum due to the high concentration of sulfate in solution (0.5 mM) utilized to achieve a pH of ~3. Oxalic acid (Ox) is also detected prior to irradiation (0 min) as a monomer, homodimer, and heterodimer with hydrogen sulfate (m/z 89, 179, and 187, respectively), and the dimer of

glycolaldehyde hydrate (Glycol+H_2O) with hydrogen sulfate is also observed at m/z 175. The $Fe(C_2O_4)_2^-$ ion, predicted by equilibrium calculations to be the dominant complex of iron (III) in the sample (Figure 3.3), is detected at m/z 232.

Upon irradiation, the $Fe(C_2O_4)_2^-$ complex and oxalic acid ions are rapidly depleted, and new ions are observed at m/z 173, 175, and 191. These photochemical oxidation products are assigned to glycolic acid (Glyc, m/z 173), glyoxylic acid (Glyox, m/z 171), and glyoxal hydrate (m/z 191), all observed as adducts with hydrogen sulfate. Formic acid is also observed as a dimer with hydrogen sulfate at m/z 143 with low intensity after 3 min of irradiation. It is possible that these ions represent the formation of organosulfate compounds rather than noncovalent complexes, but the free glycolic acid and glyoxylic acid ions (m/z 73 and 75, respectively) also increase in intensity over the course of the experiment, suggesting that the observed species are likely adducts formed during gas-phase ion generation.[134] The formation of these product ions is not observed in control experiments in which iron, glycolaldehyde, or oxalic acid is excluded from the reaction mixture (Figures 3.4 and 3.5).

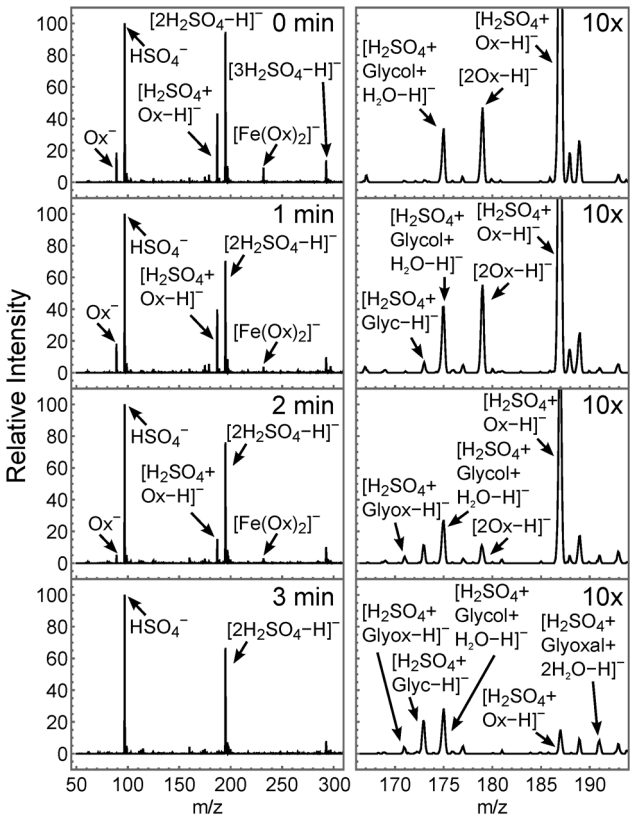

Figure 3.2. Monitoring the photochemistry of aqueous glycolaldehyde and iron (III) oxalate complexes by FIDI-MS. The left column shows the full spectrum, and the right column highlights the region where glycolaldehyde and its oxidation products are detected (10x zoom). The depletion of $Fe(C_2O_4)_2^-$ and oxalic acid (Ox) are clearly observed over the course of three minutes, and the oxidation of glycolaldehyde (glycol) to glycolic acid (glyc), glyoxylic acid (glyox), and glyoxal is observed.

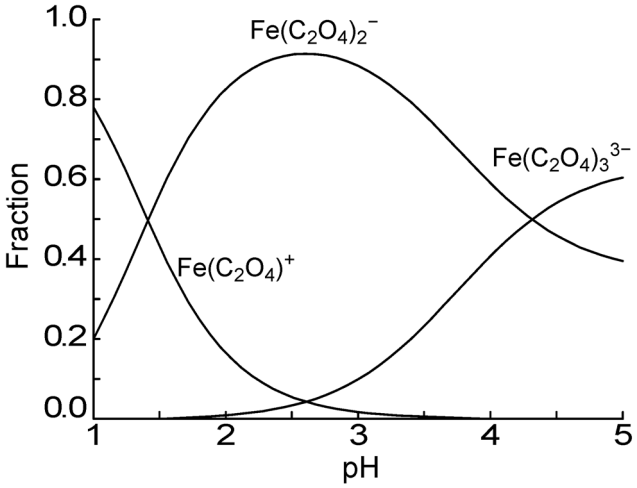

Figure 3.3. Speciation of soluble iron (III) as a function of pH under conditions utilized for FIDI-MS experiments. Solution conditions: [Fe^{3+}] = 50 µM, [Cl^-] = 150 µM, [$H_2C_2O_4$] = 250 µM, [H_2SO_4] = 0.5 mM, [NH_3] = 100 µM. Fractions were calculated using the MEDUSA program (*MEDUSA-Make Equilibrium Diagrams Using Sophisticated Algorithms, Puigdomenech, I. Royal Institute of Technology 100 44 Stockholm, Sweden; 2010*).

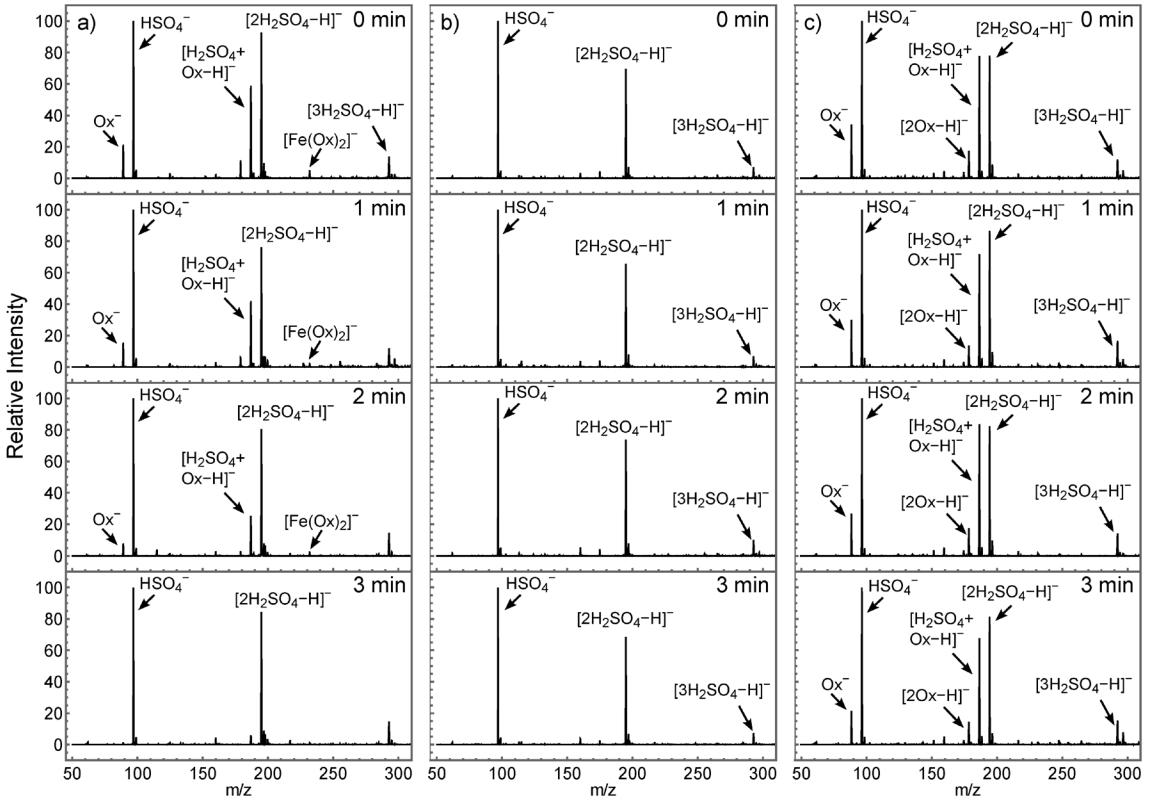

Figure 3.4. Control experiments for the oxidation of glycolaldehyde by photodissociation of iron (III) oxalate complexes; (a) iron (III) and oxalic acid only (no glycolaldehyde added), (b) iron (III) and glycolaldehyde only (no oxalic acid added), (c) glycolaldehyde and oxalic acid only (no iron added).

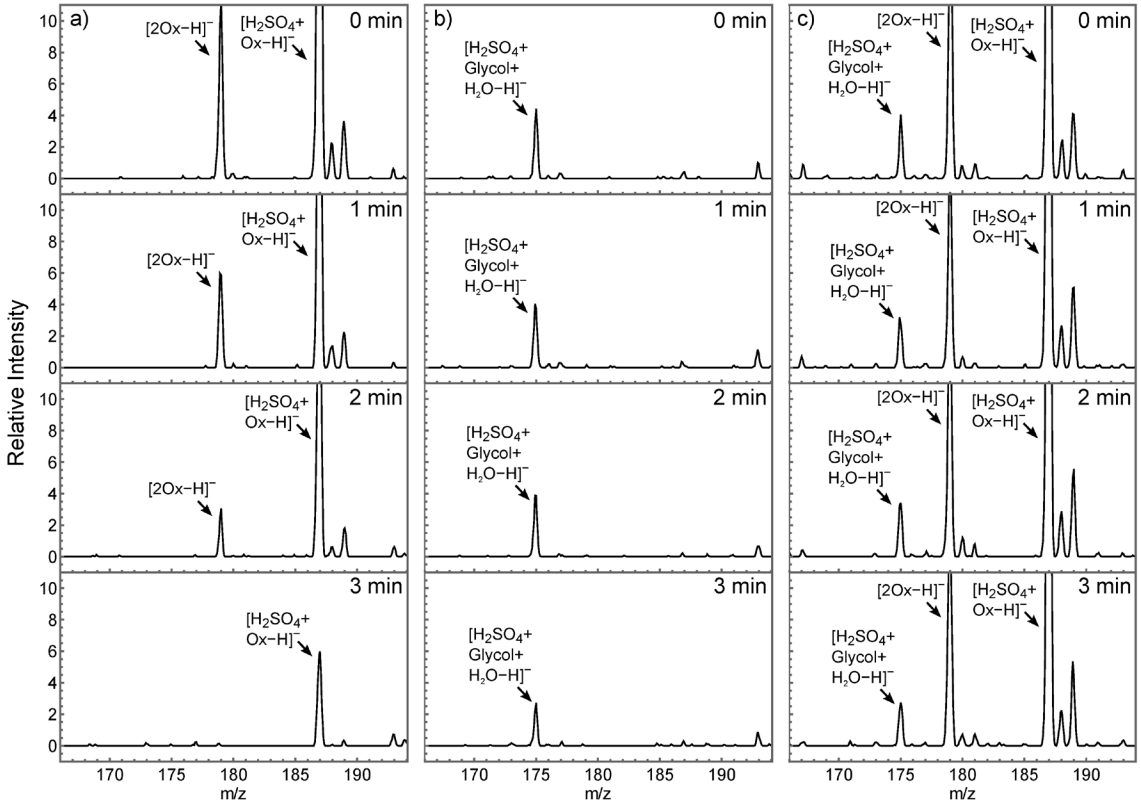

Figure 3.5. Control experiments for the oxidation of glycolaldehyde by photodissociation of iron (III) oxalate complexes, zoom on product region; (a) iron (III) and oxalic acid only (no glycolaldehyde added), (b) iron (III) and glycolaldehyde only (no oxalic acid added), (c) glycolaldehyde and oxalic acid only (no iron added).

The observed chemistry of the glycolaldehyde-ferrioxalate systems is summarized in Scheme 3.1. As described in reactions 3.4-3.10, photodissociation of iron oxalate complexes leads to the formation of hydroxyl radicals that oxidize glycolaldehyde to form glyoxal and glycolic acid. Further oxidation yields formic acid and glyoxylic acid from glycolaldehyde and glycolic acid, respectively. Glyoxylic acid may then undergo one final oxidation process to regenerate oxalic acid, whereas formic acid oxidation leads to the formation of carbon dioxide. The observed oxidation pathways are similar to those observed by Perri and co-workers for the oxidation of aqueous glycolaldehyde by hydroxyl radicals produced by H_2O_2 photolysis initiated by a 254 nm Hg lamp.[133] Perri and co-workers also detected higher molecular weight oligomers in significant abundance and identified malonic and succinic acid as two of the major oligomerization products. Further study by Ortiz-Montalvo and co-workers identified malic and tartaric acids as additional oligomerization products.[167] Similarly, in a study of aerosol formation from reactive uptake of glycolaldehyde on seed aerosol doped with iron and H_2O_2, Nguyen and co-workers proposed that oligimerization products of glycolaldehyde contributed to the high observed O/C ratios of aerosol organics. In contrast, the FIDI-MS experiments presented in this study did not detect the formation of any oligomers in significant abundance. The comparatively high flux of oxidative species produced by the photodissociation of iron (III) oxalate complexes may favor sequential oxidation over oligomerization under the conditions utilized in this study.

Scheme 3.1. Oxidation Pathway of Glycolaldehyde in the Presence of Iron (III) Oxalate Complexes

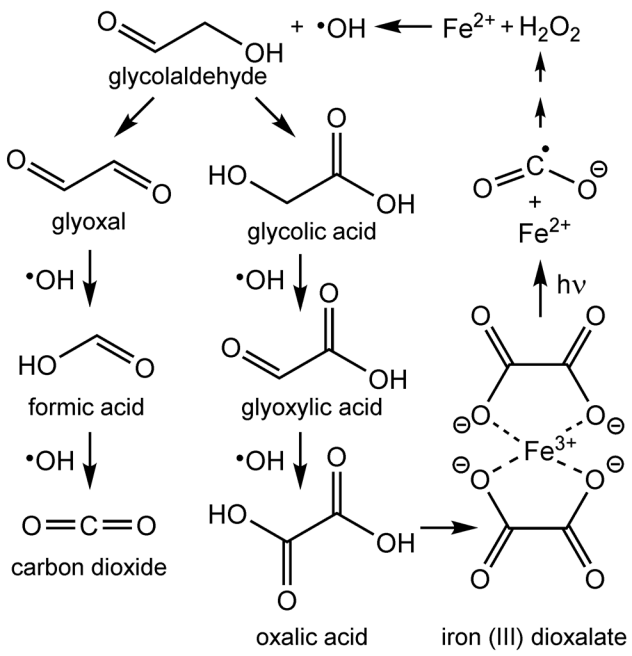

3.4.2 Iron Oxalate Photochemistry Under Deoxygenated Conditions

The photochemistry of the iron (III) oxalate and glycolaldehyde system was also investigated in the absence of oxygen by purging both the sample solution and the reaction chamber with nitrogen gas. As shown in Figure 3.6, little change in the composition of the droplets is observed during irradiation under such conditions. In contrast to the nearly complete depletion of oxalate in the presence of oxygen, the ions associated with oxalic acid are only marginally reduced in intensity over the course of the reaction. In addition, the intensity of the $Fe(C_2O_4)_2^-$ ion is significantly diminished after 1 min of irradiation, and minimal signal from oxidation products of glycolaldehyde is observed.

The absence of glycolaldehyde oxidation products in deoxygenated solutions is readily explained by the necessity of oxygen for the generation of hydroxyl radicals as detailed in reactions 3.4-3.10. The small amount of oxidation observed is attributed to trace concentrations of oxygen gas in the reaction chamber. The presence of oxygen is also necessary for the regeneration of iron (III) following photo-initiated reduction. Weller and co-workers recently measured a quantum yield of 0.8 ± 0.1 for iron (II) formation under conditions similar to those utilized in this study, indicating that iron (III) should be rapidly depleted in the absence of oxygen.[147] Consistent with this result, we do not observe the $Fe(C_2O_4)_2^-$ ion following irradiation in a nitrogen atmosphere. Similarly, little change in the intensity of oxalate ions is observed, as only 20-30% of the oxalic acid can be dissociated before all of the iron present is reduced. Zuo and Hoigné also observed that nearly all of the iron (III) was reduced to iron (II) rapidly in deoxygenated solutions, whereas in oxygenated solutions a steady state was reached once approximately 70% of the iron (III) was reduced.[92]

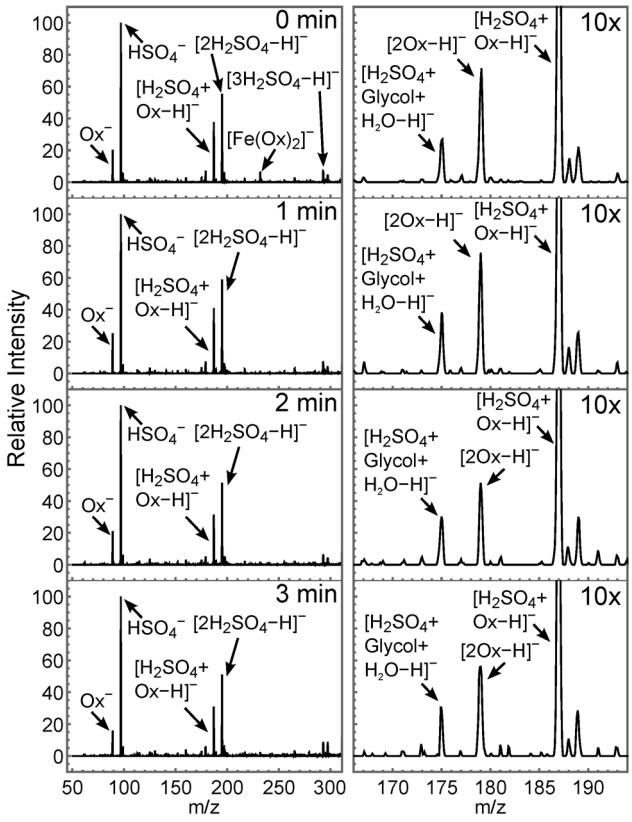

Figure 3.6. Photochemistry of deoxygenated solutions of iron (III) oxalate and glycolaldehyde. The full spectrum is shown on the left, and the right column shows a 10x zoom on the region of detection for glycolaldehyde and its oxidation products. In the absence of dissolved oxygen, little oxidation of glycolaldehyde is observed, and oxalate is not depleted over the course of the experiment. The $Fe(C_2O_4)_2^-$ ion is substantially depleted after 1 min of irradiation.

3.5 Conclusions

The photochemical dissociation of iron (III) oxalate complexes has been studied for over a half-century, yet new research into this chemical system continues to yield insight into both the fundamental mechanism of dissociation and its coupling to complex chemical systems. In the context of aqueous tropospheric chemistry, there is still a great deal of uncertainty as to the role this species might play in the aging of aqueous SOA. This study presents initial investigations into the oxidation of dissolved organics by photodissociation of complexes of iron (III) oxalate using glycolaldehyde as a model compound. Studies of photolysis in suspended microliter droplets by FIDI-MS show that glycolaldehyde is readily oxidized to glycolic acid, glyoxylic acid, and glyoxal upon 365 nm photodissociation of iron oxalate complexes. These results are in good agreement with previous studies of aqueous glycolaldehyde oxidation by Turpin and co-workers.[133,134,167] The formation of oligomers in significant abundance is not observed, which is attributed to the rapid oxidation of organic species, leading to the generation of CO_2 or regeneration of oxalic acid. These results suggest that, under the appropriate conditions, the presence of iron and oxalate in aqueous tropospheric aerosol can lead to significant oxidation of dissolved organic material. Because of the high flux of near-UV photons in the troposphere, these reactions are expected to lead to the rapid generation of oxidizing species and the depletion of oxalic acid in the presence of iron, in agreement with recent field studies.[93] Further laboratory investigations into the role of iron (III) oxalate photochemistry in reactive uptake, along with additional field measurements, are necessary to better constrain the role of such complexes in aqueous tropospheric photochemistry.

Chapter 4

Mass Spectrometric Sampling of a Liquid Surface by Nanoliter Droplet Generation from Bursting Bubbles and Focused Acoustic Pulses: Application to Studies of Interfacial Chemistry

(Reproduced in part with permission from Thomas, D. A.; Wang, L.; Goh, B.; Kim, E. S.; Beauchamp, J.L. *Anal. Chem.* **2015**, *87*, 3336-3344. http://dx.doi.org/10.1021/ac504494t

4.1 Abstract

The complex chemistry occurring at the interface between liquid and vapor phases contributes significantly to the dynamics and evolution of numerous chemical systems of interest, ranging from damage to the human lung surfactant layer to the aging of atmospheric aerosols. This work presents two methodologies to eject droplets from a liquid water surface and analyze them via mass spectrometry. In bursting bubble ionization (BBI), droplet ejection is achieved via the formation of a jet following bubble rupture at the surface of a liquid to yield 250 μm diameter droplets (10 nL volume). In interfacial sampling by an acoustic transducer (ISAT), droplets are produced by focusing pulsed piezoelectric transducer-generated acoustic waves at the surface of a liquid, resulting in the ejection of droplets of 100 μm in diameter (500 pL volume). In both experimental methodologies, ejected droplets are aspirated into the inlet of the mass spectrometer, resulting in the facile formation of gas-phase ions. We demonstrate the ability of this technique to readily generate spectra of surface-active analytes, and we compare the spectra to those obtained by electrospray ionization. Charge measurements indicate that the ejected

droplets are near-neutral (<0.1% of the Rayleigh limit), suggesting that gas-phase ion generation occurs in the heated transfer capillary of the instrument in a mechanism similar to thermospray or sonic spray ionization. Finally, we present the oxidation of oleic acid by ozone as an initial demonstration of the ability of ISAT-MS to monitor heterogeneous chemistry occurring at a planar water/air interface.

4.2 Introduction

Although several techniques have been utilized to achieve mass spectrometric analysis of molecular species at the liquid/vapor interface, there remains a need for further development in sampling methodology. For example, the analysis of planar liquid surfaces is not readily achieved employing FIDI-MS. This report introduces two alternative methods for mass spectrometric sampling from liquid surfaces: bursting bubble ionization (BBI) and interfacial sampling with an acoustic transducer (ISAT). As shown in Figure 4.1, both techniques achieve surface sampling by the ejection of droplets (0.5-10 nL volume) from the surface of the bulk solution. In BBI, these droplets are formed by a liquid jet following bubble bursting at the liquid/vapor interface, whereas in ISAT they are ejected by constructive interference of acoustic waves focused at the liquid surface.

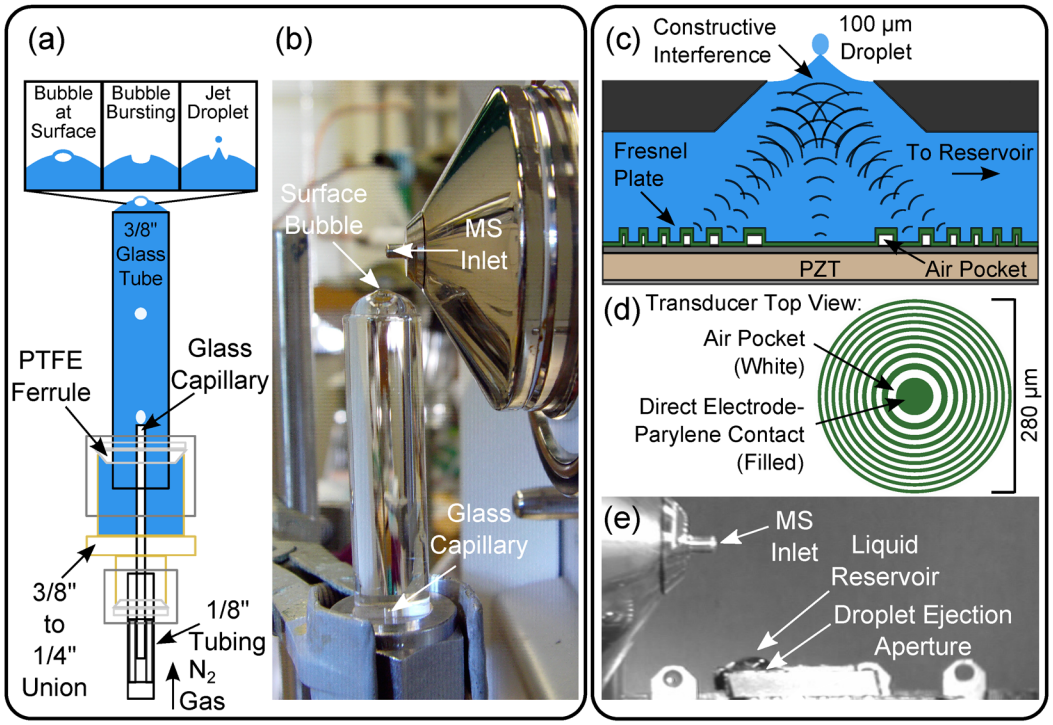

Figure 4.1. Apparatus for bursting bubble ionization (BBI) and interfacial sampling with an acoustic transducer (ISAT). The device used for BBI, which produces droplets of ~250 µm in diameter, is represented schematically in (a) and is shown interfaced with the mass spectrometer in (b). A cross section of the components of the ISAT device and an overhead view of the transducer pattern are outlined in (c) and (d), respectively. The interfacing of the device with the mass spectrometer is shown in (e).

The processes involved in bubble bursting at the water/air interface have been studied extensively for over five decades, largely in relation to their role in the generation of sea spray aerosol.[168-172] In addition, an interest in detailing the complex fluid mechanics involved in bubble bursting has led to several numerical studies.[173-176] As a bubble rises through a liquid, it may collect hydrophobic or surfactant molecules at its liquid/vapor interface, leading to enrichment of these compounds at the liquid surface.[177-182] At the liquid/vapor interface, the bubble forms a thin film layer and remains partially submerged

in the liquid. As water drains from the film, the bubble becomes unstable and bursts, yielding small film droplets and leaving a cavity in the water that was previously occupied by the bubble.[183] Liquid at the surface rapidly flows in from a radial direction to fill this cavity, collecting at the center to rise up and generate a jet that ejects one or more droplets from its tip as it becomes unstable (Figure 4.1a).[172,173,175,184] Measurement of the charge on film droplets produced in pure water reveals that they typically possess a net negative charge, suggesting that formation of the film layer leads to charge separation at the liquid/vapor interface via disruption of the electrical double layer.[10] Experiments indicate that the charge on the significantly larger jet droplets is highly dependent on experimental conditions, including bubble rise time, liquid composition, ionic strength, and bubble size.[185] In addition, observations indicate that liquid in the jet droplet predominately originates in the interfacial region, suggesting that this droplet may be enriched in molecules with preference for the interface.[186,187]

Droplet ejection from a liquid surface may also be accomplished via focused acoustic pulses.[188,189] The ISAT device utilizes an acoustic transducer patterned in concentric, annular rings that generate constructive interference of acoustic waves at a single focal point on the liquid surface, similar to the diffractive focusing of light with a Fresnel zone plate (Figure 4.1c,d).[190-192] Previous experiment and theory on acoustic droplet ejection show that a liquid cone rises from the surface at the acoustic radiation focal point due to the pressure exerted on the surface, and a droplet is produced at the cone tip when this pressure surmounts the surface tension.[188,190,193] The size of the focal point, and the resulting droplet size, can be adjusted by utilizing different harmonics of the piezoelectric resonant frequency to achieve initial droplet sizes ranging from 10-100 μm in diameter,

with volumes as small as 0.5 pL.[194] This device provides droplets of uniform size that are formed in a manner that incorporates surface-active molecules from the liquid reservoir.

This report details the use of both of these methods for the generation and mass spectrometric analysis of gas-phase ions from droplets ejected from a liquid surface. The presented experiments demonstrate the ability of these methods to readily detect surfactants and other molecules with nominal surface activity, compare these techniques to electrospray ionization (ESI), and suggest possible ionization mechanisms that lead to the detected gas-phase ions. It is found that these experimental methodologies are highly selective for the detection of surface-active species, which are often observed as solvent-ion adducts, consistent with a low-energy ionization process. We also utilize the ISAT device to monitor the oxidation of oleic acid by ozone as an initial demonstration of the ability of this technique to observe interfacial chemistry at a planar water/air boundary.

4.3 Experimental Methods

4.3.1 Materials

High performance liquid chromatography (HPLC)-grade methanol was purchased from J.T. Baker Avantor (Center Valley, PA), and high-purity water was purchased from EMD Millipore (Billerica, MA). All other chemicals were purchased from Sigma-Aldrich (St. Louis, MO). Stock solutions were prepared in concentrations of 5-10 mM in water or methanol using volumetric glassware. Experimental samples were then prepared by dilution of these stock solutions with use of micropipettes. Samples for BBI and ISAT were prepared in 100% water, and those for ESI were prepared in 80/20% (v/v) water/methanol due to the requirement of a lower surface tension in this experimental methodology.

4.3.2 Mass Spectrometry

All experiments were performed with use of an LTQ-XL ion trap mass spectrometer (Thermo-Fisher, Waltham, MA). ESI was performed utilizing the standard instrument electrospray source. Interfacing of ionization sources with the atmospheric pressure inlet was accomplished by removal of the spray cone for better access to the transfer capillary. Positive mode spectra were collected with a capillary temperature of 180º C, a capillary voltage of 19 V, and a tube lens voltage of 175 V. In negative mode, a capillary offset of -45 V and a tube lens voltage of -139 V were utilized.

4.3.3 Bursting Bubble Ionization (BBI)

As illustrated in Figure 4.1a, the BBI apparatus consists of a borosilicate glass tube (1/2 in. OD, 3/8 in. ID) connected via a PTFE ferrule to a 1/2 in. to 1/4 in. reducing union (Swagelok, Solon, Ohio). On the opposite side of the reducing union, a segment of 1/4 in. OD polyethylene tubing approximately 1.5 in. in length is connected. Sheathed inside of this tubing and passing through the reducing union is a glass capillary 1.6 mm in diameter with a 0.25 mm wall thickness (Kimble-Chase, Vineland, NJ). The volume of the large glass tube is filled with the sample of interest, and nitrogen gas is flowed through the inner glass capillary via a leak valve (Series 203, Brooks Granville-Phillips, Chelmsford, MA) at a flow rate optimized to form a single bubble of ~2.5 mm in diameter that rises to the liquid/vapor interface every 15 s. The apparatus is placed approximately 7-10 mm beneath the inlet to the mass spectrometer (Figure 4.1b), and bubble bursting generates a jet droplet of ~250 μm in diameter that is aspirated by the LTQ capillary inlet, resulting in the

detection of ions by the mass spectrometer. The data presented in this paper consist of an average of 5 sampling events, each from a distinct jet droplet.

4.3.4 Interfacial Sampling by an Acoustic Transducer (ISAT)

The fabrication of the self-focusing acoustic transducer used for droplet generation in this work has been described previously.[190,191,193,194] The device consists of a lead zirconate titanate piezoelectric transducer (PZT) with top and bottom nickel electrodes adhesively bonded to a microfluidic device consisting of a droplet generation chamber coupled to a liquid reservoir to maintain the water height at the focal point of the acoustic waves. As shown schematically in parts c and d of Figure 4.1, a series of annular rings (Fresnel half-wave bands) consisting of air pockets under a layer of parylene D are patterned on the base of the droplet generation chamber. The air pockets reflect acoustic waves due to impedance mismatch, whereas direct contact between the parylene and the transducer electrode allows for the transmission of the acoustic waves to the liquid. Constructive interference of the transmitted acoustic waves at a focal point on the surface of the liquid results in droplet ejection. To achieve directional ejection toward the mass spectrometer inlet, a slightly modified design that introduces an unbalanced acoustic body force at the focal point was employed.[193] A radiofrequency (rf) generator was coupled to a switch to generate short rf pulses of ~10 μs in duration, which were subsequently passed through an rf amplifier and used to drive the PZT at a pulse frequency of 1-120 Hz. The device utilized was designed to operate with a focal length of 800 μm and a transducer frequency of approximately 20 MHz, the fundamental frequency, with droplet size limited by the wavelength of the acoustic waves in water (~80 μm).[188,194] The experimental amplitude and frequency of the

waveform applied to the transducer were optimized to achieve droplet ejection from solution into the mass spectrometer, and the droplets generated were observed to be approximately 100 μm in diameter, corresponding to a volume of 0.5 nL. The apparatus was placed on a metal breadboard mounted to the front of the LTQ approximately 15 mm below the inlet as shown in Figure 4.1e, and droplets ejected from the surface were aspirated into the inlet of the mass spectrometer, resulting in the detection of gas-phase ions. Approximately 10-20 droplet sampling events at a rate of 1-10 Hz were averaged to generate a spectrum. For time-dependent reaction monitoring, each spectrum represents a single droplet sampling.

4.3.5 Droplet Charge Measurements

To measure droplet net charge, droplets were impacted and collected on a stainless steel plate connected to an electrometer (Model 6514, Keithley, Cleveland, OH), and the resulting current was monitored. The plate and droplet ejection apparatus were surrounded by a copper mesh to minimize interference from laboratory equipment. For the BBI experiments, the frequency of droplet ejection was too low to detect any current. A charge measurement setup was also attempted in which the charge induced on a second, electrically isolated plate was measured following droplet adhesion to the first plate, but this setup failed to yield any detectable charge on the droplets. To measure the charge on droplets generated by ISAT, the device was operated at a frequency of 60-120 Hz to provide a measurable current.

4.3.6 Ozone-Initiated Oxidation at ISAT Liquid Surface

The reaction of ozone at the surface of a planar liquid was monitored by exposing the surface of the ISAT device to a flow of the reactive gas. Ozone was generated by flowing laboratory compressed air through a glass vial containing a pencil-style ultraviolet lamp (Oriel 6035, Newport, Irvine, CA) at a rate of ~0.5 L min^{-1}. The liquid surface at the ejection aperture of the ISAT device was exposed to the gas flow via an effusive gas source. Measurement of the time-dependent oxidation of a molecule of interest was then achieved by the ejection of droplets from the ISAT device and subsequent detection as outlined above.

4.4 Results and Discussion

4.4.1 Detection of Surface-Active Species

Figure 4.2 shows the BBI and ISAT spectra for several analytes possessing high surface activity, prepared at a concentration of 50-100 μM in water. The dodecyltrimethylammonium (DDTMA, Figure 4.2b), dodecyl sulfate (DS, Figure 4.2c), and oleic acid (OA, Figure 4.2d) ions possess a hydrophobic hydrocarbon tail and hydrophilic charged headgroup that confer surfactant properties, causing these molecules to preferentially localize to the liquid/vapor interface. The peptide bradykinin (RPPGFSPFR, Figure 4.2a) possesses two terminal hydrophilic arginine residues connected by predominately hydrophobic amino acid residues that may result in surface activity for the molecule. Detection of ions in both positive mode (bradykinin, DDTMA) and negative mode (DS, OA) demonstrate that these sampling methods are capable of generating gas-phase ions of either polarity. In addition, it was observed that ions of either

polarity could be detected in sampling events from the same solution, especially in BBI. For all samples, the two techniques are capable of analyte detection with good signal-to-background ratios.

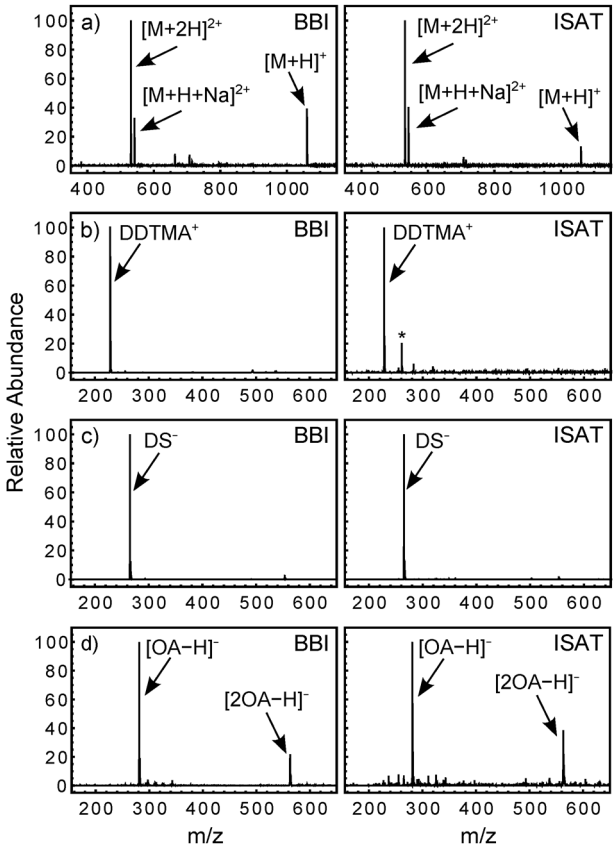

Figure 4.2. Detection of positively- and negatively-charged surface-active analytes using BBI (left column) and ISAT (right column): (a) 50 µM bradykinin, (b) 50 µM dodecyltrimethylammonium bromide (DDTMAB), (c) 100 µM sodium dodecyl sulfate (SDS), and (d) 50 µM oleic acid (OA). Asterisk in 2b indicates a contaminant present in the ISAT device (m/z 261). Surface-active species of positive (a, b) and negative (c, d) charge are readily detected in both methods, with similar spectra obtained by either technique.

4.4.2 Preferential Ionization of Surface-Active Species

The preferential ionization of surface-active compounds is a well-known phenomenon occurring in ESI.[111] To gain insight into the gas-phase ion generation process of the droplet ejection-based methodologies, the preferential ionization of surface-active analytes in BBI and ISAT spectra was analyzed and compared to results from ESI. Figure 4.3 shows the spectrum obtained by sampling an equimolar solution of sodium iodide and sodium bromide employing ESI, BBI, and ISAT. The BBI and ISAT methods tend to produce significantly more water adducts of bromide and iodide than ESI, with BBI yielding the largest abundance of these species. Given the low free energies associated with halide water adduct formation in the gas phase (~22 and ~30 kJ/mol for bromide and iodide, respectively),[195-197] it is possible that these adducts arise following gas-phase ion formation, as has been observed previously via the addition of solvent vapors to the sheath gas of an ESI source.[198] The comparatively large volume of droplets in BBI and ISAT will increase the vapor pressure of water within the capillary and vacuum transfer region of the mass spectrometer, resulting in increased adduct production. Alternately, the adduct formation may occur during the process of droplet evaporation and gas-phase ion generation.

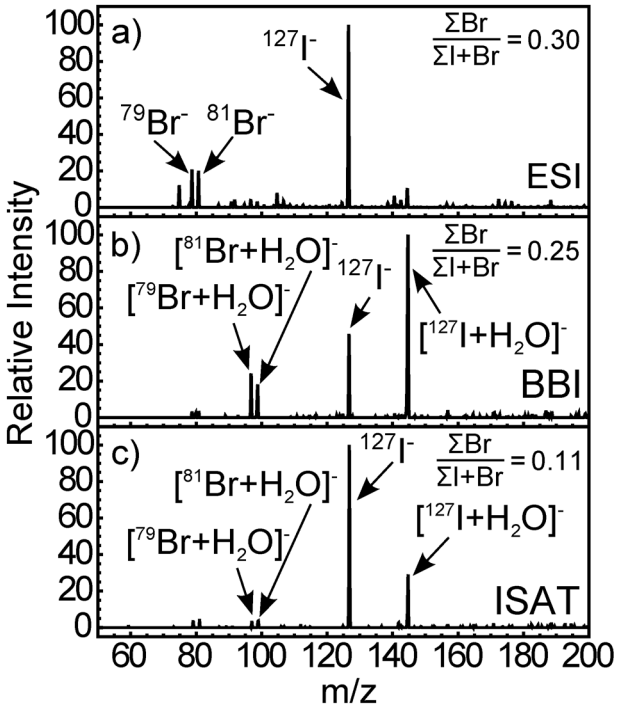

Figure 4.3. Preferential ionization of iodide over bromide in an equimolar solution (10^{-4} M) of the sodium salts. BBI and ISAT (b and c) yield a stronger response for iodide than bromide when compared with ESI (a), with ISAT yielding the largest difference in response between the two species. BBI and ISAT also tend to yield significantly more water adducts than ESI.

Also of note in the spectra of Figure 4.3 is a higher abundance of I^- over Br^-. This effect has been observed previously in ESI and is attributed to selective enrichment of iodide ions during the charged droplet discharge process, in which charged molecules preferentially localized to the liquid/vapor interface (i.e., those ions with less favorable solvation energies) are conducted along the surface of the droplet and serve as charge carriers in the progeny droplets.[199] Alternately, the difference in abundance in ESI may be explained by the ion evaporation model, in which the lower solvation energy of the iodide ion compared with that of the bromide ion results in preferential evaporation of iodide and thus a higher abundance of gas-phase ions of this species.[200] The preference of large, polarizable halide

ions for the liquid/vapor interface has also been noted in molecular dynamics simulations of alkali metal halide solutions.[11,15,32,34] The BBI and, to a more pronounced extent, ISAT spectra exhibit greater selectivity for iodide over bromide than ESI, which may be a result of either enrichment of molecules present at the liquid/vapor interface during droplet generation or differences in the ionization process that lead to altered preferential ionization of surface-active species. Similar results were observed for the preferential ionization of surface-active tetraethylammonium ions over the well-solvated cesium ions in an equimolar solution.

4.4.3 Charge Measurement of Ejected Droplets

The mechanism of gas-phase ion production in electrospray ionization requires the generation of charged droplets that undergo subsequent evaporation and Rayleigh discharge to yield progeny droplets carrying <5% of the volume and 20-30% of the charge of the parent droplet.[111,201-203] Transfer of ions to the gas phase is also observed in techniques where droplets are formed without the application of an electric field, such as sonic spray ionization (SSI), in which charged droplet formation is proposed to occur via statistical fluctuations of ion concentration during droplet formation and/or the segregation of charges during droplet breakup within the atmospheric pressure interface of the mass spectrometer.[72,112,204,205] To investigate the possible mechanisms involved in ion formation in BBI and ISAT, measurement of the charge on the ejected droplets was undertaken.

Droplets were ejected from a liquid surface using the ISAT device at a rate of 60 or 120 Hz and collected on a stainless steel plate connected to an electrometer to measure the generated current. As summarized in Table 4.1, these experiments indicate that ejected

droplets possess a small but measurable charge. The HPLC grade water may still contain a significant number of charge carriers other than the hydronium and hydroxide ions, as the liquid was not further purified, and plasticizers and other unidentified compounds could be detected in the mass spectrum by ISAT of pure water samples. The charge of surface-active molecules in the sample influences the net charge of the droplets generated, with the polarity of the measured current dictated by the charge of the analyte. For all samples examined in these experiments, less than 5×10^4 net charges per droplet were estimated, putting these droplets significantly below the Rayleigh limit for droplet discharge (<0.1%) at the initial droplet diameter.[111,206] To reach the Rayleigh limit by evaporation, a water droplet containing this number of charges would have to evaporate to approximately 1 μm in diameter. For comparison, if a stream of droplets of 100 μm in diameter were produced by ESI, they would be initially charged to approximately 80% of the Rayleigh limit, produce a current of 700 pA at an impact rate of 120 Hz, and undergo Rayleigh discharge at a droplet diameter of 88 μm.[201] As discussed below, the time scale of droplet transfer to the high vacuum region of the mass spectrometer is not sufficient for the droplets generated by ISAT to reach the Rayleigh limit via evaporation, suggesting alternate ionization mechanisms are operative under the experimental conditions.

Table 4.1. Measured Current for Droplets 100 μm in Diameter Produced by the ISAT device and Collected on a Stainless Steel Plate at Given Rate[a]

sample	droplet pulse rate (Hz)	measured current (pA)	charges/ droplet	% Rayleigh limit
HPLC grade water	60	0.1	1×10^4	0.02
100 μM CsI, 100 μM TEAB in water	120	0.5	3×10^4	0.06
50 μM SDS in water	120	−0.2	1×10^4	0.02

[a]Net charge per droplet and percentage of the Rayleigh limit are calculated.

4.4.4 Droplet Residence Time and Evaporation

The proposed mechanism for ion formation must be consistent with the temporal constraints imposed by the droplet sampling from the vapor phase through the inlet capillary of the mass spectrometer. The transfer time of a droplet through the mass spectrometer inlet capillary is dependent upon the gas flow rate through the inlet, which can be approximated using the Poiseuille equation,[205,207]

$$Q = \frac{\pi r^4}{8\eta L}\Delta P \qquad (4.1)$$

where ΔP represents the pressure difference across the inlet (759 Torr), r is the radius of the transfer capillary (250 μm), η is the dynamic viscosity of air (2.5×10^{-5} Pa s at 450 K),[208] L is the capillary length (100 mm), and Q is the volumetric flow rate. This equation yields a volumetric gas flow of 4.2×10^{-5} m^3 s^{-1}, or a gas velocity of ~200 m/s and a gas transfer time of ~0.5 ms, which agrees reasonably well with the gas flow at the MS inlet of ~1×10^{-5} m^3 s^{-1} determined with use of a Gilibrator (Sensidyne, St. Petersburg, FL). Although this approximation does not take into account the change in gas flow velocity

across the transfer tube, the transfer time was also found to be in good agreement with previous studies and serves as an order of magnitude estimate for gas transfer time.[205,209,210]

When the aspirated droplet initially enters the capillary, its velocity along the axis of the capillary is near zero, and the acceleration of the droplet to the carrier gas velocity requires a non-negligible amount of time. This rate of acceleration can be estimated from the drag force F_D exerted on the droplet by the flowing gas, given by[211]

$$F_D = C_D \frac{\pi}{8} \rho_g d^2 \left(v_{gas} - v_{droplet}\right)^2 \tag{4.2}$$

where C_D is the coefficient of drag (~0.44 at the high Reynolds numbers encountered in this system),[211] ρ_g is the gas density (~1 kg/m^3),[208] d is the droplet diameter, v_{gas} is the gas velocity, and $v_{droplet}$ is the droplet velocity. Neglecting the effects of turbulent flow, the timescale for droplet transit across the capillary can be estimated by accounting for the acceleration caused by the drag force on the droplet to yield the differential equation

$$m \frac{d^2x}{dt^2} = C_D \frac{\pi}{8} \rho_g d^2 \left(v_{gas} - \frac{dx}{dt}\right)^2 \tag{4.3}$$

For a droplet of diameter 100 µm, the calculated transit time across a 100 mm capillary is approximately 15 ms.

The rate of change of a droplet of diameter d due to evaporation is given by[211]

$$\frac{d(d)}{dt} = \frac{4 D_v M}{R \rho_d d} \left(\frac{p_\infty}{T_\infty} - \frac{p_d}{T_d}\right) \tag{4.4}$$

where M is the solvent molar mass, D_v is the diffusivity of the solvent vapor in air, ρ_d is the solvent density, and R is the gas constant. The solvent partial pressure well away from the droplet surface and at the droplet surface are represented by p_∞ and p_d, respectively, and

the corresponding temperatures are denoted by T_∞ and T_d. Integrating this equation yields the droplet evaporation rate as a function of time[211,212]

$$d^2 = d_0^2 + \frac{8D_v M}{R\rho_d}\left(\frac{p_d}{T_d} - \frac{p_\infty}{T_\infty}\right)t \qquad (4.5)$$

where d_0^2 is the initial droplet diameter. The solvent evaporation process is endothermic, lowering the temperature at the droplet surface, T_d, until equilibrium between evaporative cooling and heat conduction from the surrounding air is achieved. This steady state temperature can be calculated by[211]

$$T_d = T_\infty - \frac{D_v M \Delta H_{vap}}{R k_v}\left(\frac{p_d}{T_d} - \frac{p_\infty}{T_\infty}\right) \qquad (4.6)$$

where ΔH_{vap} is the solvent enthalpy of vaporization at temperature T_d and k_v is the thermal conductivity of the gas. Since many of the parameters in equation 4.6 are temperature-dependent, specifically D_v, p_d, ΔH_{vap}, and k_v, the equation must be solved for T_d iteratively until a self-consistent temperature is achieved. The solvent enthalpy of vaporization and equilibrium vapor pressure were taken from Yaws,[213] the diffusion coefficient of water in air was taken from Vargaftik *et al.*,[214] and the thermal conductivity of air was taken from Kadoya *et al.*[215] The value of p_∞ was approximated by the partial pressure of water vapor in air at 50% relative humidity at 298 K,[213] and T_∞ was set to the transfer capillary temperature (450 K). These parameters give an equilibrium droplet surface temperature, T_d, of 318 K, which was used for the calculation of the droplet diameter as a function of time according to equation 4.5, with solvent density at this temperature taken from *The CRC Handbook of Chemistry and Physics*.[208]

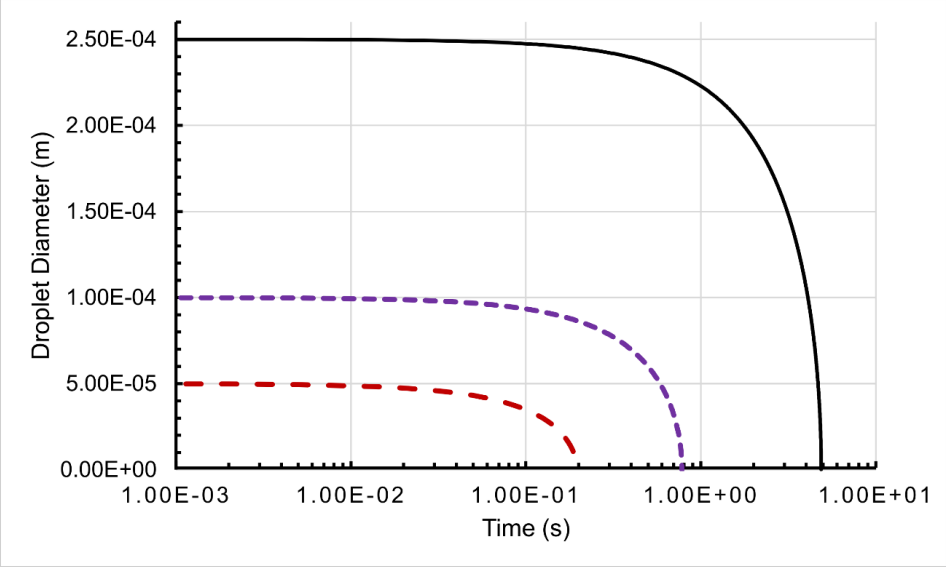

Figure 4.4. Calculated change in droplet diameter with time for droplets of diameter 50 µm (red, large dash), 100 µm (purple, small dash), and 250 µm (black, solid line) at a gas temperature of 450 K and a water vapor pressure of 1571 Pa (50% relative humidity at 298 K). The time axis is presented on a logarithmic scale. See text for details.

The graph of droplet diameter as a function of time calculated from equations 4.5 and 4.6 is shown in Figure 4.4 for droplets of diameter 50, 100, and 250 µm, which are found to evaporate in 200 ms, 780 ms, and 4.9 s, respectively. Thus, for the 100 and 250 µm diameter droplets utilized in this study, the evaporation time is longer than the calculated 15 ms residence time by several orders of magnitude.[201,205,212] In addition, the high Weber number conditions present within the transfer capillary suggest the droplet will undergo aerodynamic breakup into smaller droplets during transit.[205,216,217] Therefore, it is not likely that droplet evaporation to the Rayleigh limit followed by droplet discharge could produce the observed ions, and other ionization mechanisms must be explored.

4.4.5 Ionization Mechanism in BBI and ISAT

Given the relatively large diameter (100-250 μm) of droplets utilized in this study in comparison to the inner diameter of the transfer capillary (~1 mm), droplet nebulization via interaction with the heated walls of the capillary may contribute significantly to the ionization process. A similar phenomenon has been observed previously by Vestal and co-workers in thermospray ionization. In this technique, the eluent from a liquid chromatography column is flowed into a heated capillary, resulting in the nebulization and partial vaporization of the solvent.[218,219] This process generates charged droplets, most likely as a result of statistical fluctuations in ion concentration,[204] that subsequently follow the ESI mechanism.[220,221] A similar process may also occur in the solvent-assisted inlet ionization technique developed by Trimpin, McEwen, and co-workers.[222,223] In addition, Jarrold and co-workers found that highly charged droplets may be generated from larger, near-neutral droplets in sonic spray ionization via charge separation during the aerodynamic breakup of droplets.[205] Such processes may also be operative in other droplet generation techniques that do not rely on electric fields, including easy ambient sonic spray ionization (EASI) and ultrasonication-assisted spray ionization (UASI).[224-226] These putative mechanisms are compatible with the data presented in this work and account for the tendency of BBI and ISAT to yield water adducts (Figure 4.3) as well as the ability to observe positive and negative ions with identical sampling conditions.

4.4.6 Monitoring Heterogeneous Chemistry with ISAT

As an initial demonstration of the ability of the ISAT droplet ejection technique to monitor heterogeneous chemistry, we studied the time-dependent oxidation of oleic acid by ozone. This system is regarded as a benchmark to compare experimental methodologies for the study of interfacial oxidation.[27,83,227-230] As summarized in Scheme 4.1, oxidation of oleic acid proceeds via formation of a primary ozonide, followed by ring opening to the right or left to yield nonanal (**1**) or 9-oxononanoic acid (**2**), respectively, along with the corresponding Criegee intermediate. These intermediates may then proceed along numerous reaction pathways, including formation of secondary ozonides, peroxides, diperoxides, and α-acyloxyalkyl hydroperoxides, which may subsequently undergo decomposition or polymerization to yield a complex set of products.[227,228] Although measured yields are highly sensitive to experimental conditions, the most abundant products generally observed in oleic acid oxidation are nonanal (**1**) and 9-oxononanoic acid (**2**), with slightly lower abundances of nonanoic acid (**3**) and azelaic acid (**4**).[229,230] A previous study by Grimm and co-workers utilizing FIDI-MS to study the oxidation of oleic acid dissolved in 90/10 (v/v) dimethylformamide/methanol observed azelaic acid as the most abundant product detectable as an anion, suggesting that the solvent plays a crucial role in determining the favored reaction pathway.[83]

Scheme 4.1. Oxidation of Oleic Acid by Ozone and Subsequent Reaction Pathways

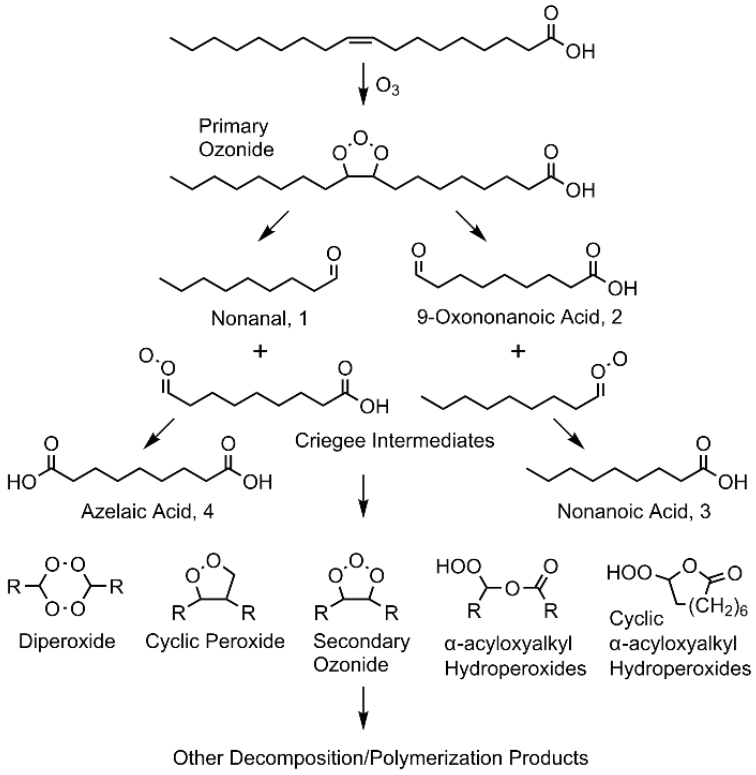

For study of the oxidation of oleic acid using the ISAT methodology, a solution containing oleic acid at a concentration of 100 μM and a small amount of sodium dodecyl sulfate (< 10 μM) as a nonreactive, surface-active reference species in water was loaded into the device. The liquid surface at the droplet ejection aperture was then exposed to a flow of air containing ozone generated by ultraviolet photodissociation of oxygen. Droplets were sampled from the surface at several time points during the experiment to monitor the progress of the reaction. As shown in Figure 4.5, the oleic acid anion is observed to decay in intensity over the course of the experiment, whereas the nonreactive dodecyl sulfate (DS) anion is detected even at long exposure times. The main product detected from oleic acid oxidation is 9-oxononanoic acid (9-ONA), in agreement with the majority of previous

studies of oleic acid oxidation.[230] Nonanal is also frequently reported as a major product of oleic acid oxidation but could not be detected by the mass spectrometer in negative mode due to the absence of a negatively charged functional group. Although the droplet formation process disturbs the structure of the interface in a manner that may influence what is subsequently observed in the mass spectrum relative to what originally comprised the surface, sequential sampling was still capable of observing the progression of oleic acid oxidation in this experiment.

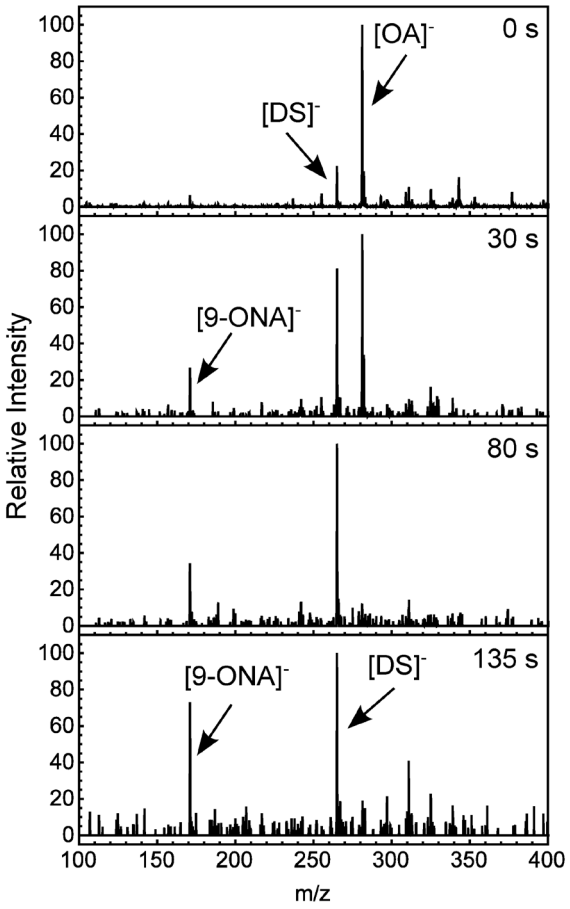

Figure 4.5. Time-dependent oxidation of oleic acid (OA) at a liquid surface by impinging gas-phase ozone, as monitored by ISAT-MS. A small amount of dodecyl sulfate (DS) serves as a nonreactive reference species at the interface. During the experiment, the oleic acid disappears from the spectra and is replaced by 9-oxononanoic acid (9-ONA).

4.5 Conclusions

Two new methods for the ejection of droplets from nominally planar surfaces are coupled with mass spectrometry to study the chemistry of liquid surfaces. Droplets are produced either by bubble bursting and subsequent jet formation or through the acoustic radiation pressure exerted on a liquid surface by focused acoustic waves. The droplets generated by these methodologies can be aspirated by the heated transfer capillary of a mass spectrometer, yielding gas-phase ions of both positive and negative polarity from surface-active analytes with high sensitivity. The ability to generate ions from near-neutral droplets on a time scale much shorter than that required for droplet evaporation to the Rayleigh limit suggests that droplet breakup, nebulization, and vaporization may occur within the heated transfer capillary to assist in the production of gas-phase ions.

The use of droplet ejection to study chemical reactions at liquid surfaces via mass spectrometry has many promising future applications. The ability to monitor the reactions of complex chemical systems occurring at liquid surfaces is highly complementary to the detailed structural information provided by surface-sensitive spectroscopic techniques.[42,231] The ISAT device in particular allows for the controlled generation of droplets from a planar liquid surface on demand, making this methodology readily amenable to the study of heterogeneous chemical reactions, such as the reaction of gas-phase hydroxyl radicals and ozone with surface-active analytes in solution.[7,48,83,229,232,233] We provide in this work results for the oxidation of oleic acid by ozone as an initial example of the ability of the ISAT device to monitor heterogeneous reactions at the liquid/vapor interface. The ISAT methodology may prove especially useful for the study

of planar liquid surfaces. For example, the ISAT apparatus may be integrated with a Langmuir-Blodgett trough to study the effect of surface pressure on the structure and reactivity of surface films, especially with respect to the spatial separation of analytes at increased pressures.[234-236] In addition, operation of an ISAT apparatus designed to function at higher harmonics can produce droplets as small as 10 μm in diameter (500 fL volume),[194] and optimization of this configuration for mass spectrometric sampling may lead to decreased disruption of the interfacial layer and will likely enhance specificity for sampling of species present at the liquid/vapor interface.

Chapter 5

Hydrogen Bonding Constrains Free Radical Reaction Dynamics at Serine and Threonine Residues in Peptides

(Reproduced in part with permission from Thomas, D. A.; Sohn, C. H.; Gao, J.; Beauchamp, J. L. *J. Phys. Chem. A* **2014**, *118*, 8380-8392. http://dx.doi.org/10.1021/jp501367w Copyright 2014 American Chemical Society.)

5.1 Abstract

Free radical-initiated peptide sequencing (FRIPS) mass spectrometry derives advantage from the introduction of highly selective low-energy dissociation pathways in target peptides. An acetyl radical, formed at the peptide N-terminus via collisional activation and subsequent dissociation of a covalently attached radical precursor, abstracts a hydrogen atom from diverse sites on the peptide, yielding sequence information through backbone cleavage as well as side-chain loss. Unique free radical-initiated dissociation pathways observed at serine and threonine residues lead to cleavage of the neighboring N-terminal C_α–C or N–C_α bond rather than the typical C_α–C bond cleavage observed with other amino acids. These reactions were investigated by FRIPS of model peptides of the form AARAAAXAA, where X is the amino acid of interest. In combination with density functional theory (DFT) calculations, the experiments indicate the strong influence of hydrogen bonding at serine or threonine on the observed free radical chemistry. Hydrogen bonding of the side chain hydroxyl group with a backbone carbonyl oxygen aligns the singly occupied π orbital on the β-carbon and the N–C_α bond, leading to low-barrier β-

cleavage of the N−C_α bond. Interaction with the N-terminal carbonyl favors a hydrogen-atom transfer process to yield stable *c* and $z^\bullet$ ions, whereas C-terminal interaction leads to effective cleavage of the C_α−C bond through rapid loss of isocyanic acid. Dissociation of the C_α−C bond may also occur via water loss followed by β-cleavage from a nitrogen-centered radical. These competitive dissociation pathways from a single residue illustrate the sensitivity of gas-phase free radical chemistry to subtle factors such as hydrogen bonding that affect the potential energy surface for these low-barrier processes.

5.2 Introduction

Over the last two decades, the use of mass spectrometry experiments for the sequencing of biological molecules has been a major field of research, especially in the area of protein analysis, where high resolution and unparalleled sensitivity make tandem mass spectrometry (MS/MS) experiments the method of choice.[237-241] Successful dissociation of peptides or proteins in the gas phase is essential for obtaining peptide sequence information, and collision-induced dissociation (CID) and infrared multiphoton dissociation (IRMPD) remain the most widely utilized approaches for inducing backbone cleavage even after several decades of research.[242-245] In these techniques, input energy is statistically redistributed throughout the degrees of freedom of the peptide, resulting predominantly in the cleavage of the amide linkage and generally yielding significant sequence coverage.[246] However, shortcomings of these methods become apparent in the examination of peptides containing aspartic and glutamic acid or proline residues, where cleavage is highly selective, as well as in the analysis of post-translational modifications (PTMs), which are typically lost as neutral fragments in low-energy pathways.[245,247]

Partially in response to these limitations, the past decade has seen the development of new techniques that rely on radical-induced dissociation to provide sequence information. These methods can generally be grouped by their utilization of either hydrogen-abundant or hydrogen-deficient radicals.[248] Hydrogen-abundant radical techniques include electron capture and electron transfer dissociation (ECD and ETD, respectively), which mainly effect cleavage of backbone N−C_α bonds through the capture of low-energy electrons, yielding N-terminal c and C-terminal z$^\bullet$ product ions.[244,249-251] The unexpected cleavage of the comparatively strong N−C_α bond has led to a large body of work investigating the mechanism of ETD and ECD,[249,252-258] with the Utah-Washington (UW) mechanism proposed independently by Simons and co-workers[259-267] and Tureček and co-workers[257,268-274] being the most prevalent explanation. This mechanism posits that N−C_α bond dissociation occurs by electron attachment to an amide π^* orbital, either by direct electron capture or by intramolecular transfer from a high n-Rydberg state, yielding an amide radical "superbase" anion, which rapidly undergoes N−C_α bond cleavage.[255,269] Though significant progress has been achieved in elucidating the mechanism of ECD and ETD, many questions about this intriguing process remain under debate, such as the initial site of electron capture or transfer and the order of N−C_α bond cleavage and proton transfer.[255,275-277] The success of these techniques, however, is not disputed; they provide extensive sequence coverage through predominantly nonselective backbone cleavage with retention of PTMs.[245,278-280] These attributes, along with the ability to selectively cleave disulfide bonds, make ECD and ETD excellent methods for a wide range of proteomic analyses, from identification of glycosylation sites to the analysis of disulfide linkages.[240,245,252,253,281,282]

Scheme 5.1. Generation of Peptide Free Radicals by N-Terminal Derivatization and Gas-Phase Collisional Activation

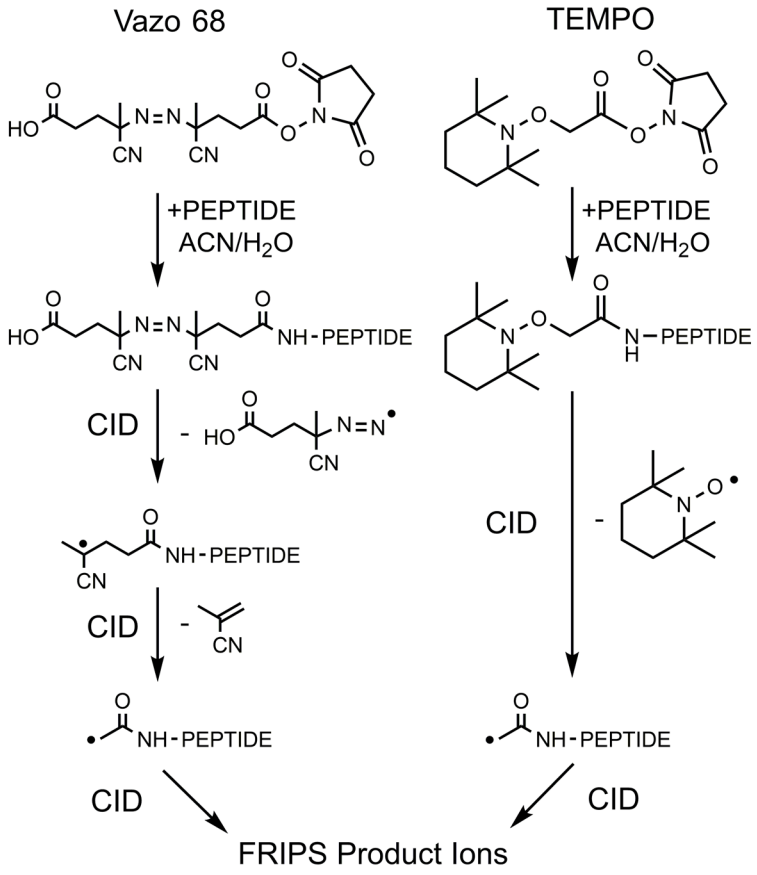

Parallel to the development and implementation of the hypervalent radical techniques, many research groups investigated methods for the formation of hydrogen-deficient radical peptides. Initially, these species were generated by UV photoionization of aromatic residues or CID of copper coordination complexes to generate copper-bound peptide radicals.[283] More recent work has established simple techniques for the generation of hydrogen-deficient peptide radicals, including CID of an array of peptide-metal complexes,[284-290] peptide irradiation with 157 nm light,[291-293] and photodissociation of carbon-iodine bonds.[294-296] To achieve regioselective free radical generation via collisional

activation, Porter and co-workers converted the lysine side chain to a peroxycarbamate moiety,[297,298] whereas O'Hair and coworkers utilized nitrosylation and nitrate ester formation at cysteine and serine residues, respectively.[299-303] In addition, Hodyss and co-workers developed the technique of free-radical-initiated peptide sequencing (FRIPS), in which a well-defined radical site is produced at the N-terminus of a peptide or protein by dissociation of a covalently bound free radical precursor through a low-energy pathway.[304] The initial free radical precursor developed for this experiment was based on the Vazo-68 free radical initiator, which was coupled to the N-terminus via an acetyl group. As shown on the left side of Scheme 5.1, a two-step gas-phase collisional activation resulted in the generation of an acetyl radical at the N-terminus of the peptide. Later work by Lee and co-workers as well as Sohn and co-workers employed processes involving use of the stable TEMPO (2,2,6,6-tetramethylpiperidine-1-oxyl) free radical,[305-308] which provides the advantage of requiring only a single stage of collisional activation for radical generation, as demonstrated on the right side of Scheme 5.1. The latter methodology is employed in the current investigation.

Scheme 5.2. Mechanism of Peptide Dissociation by Hydrogen-Deficient Free Radical Chemistry

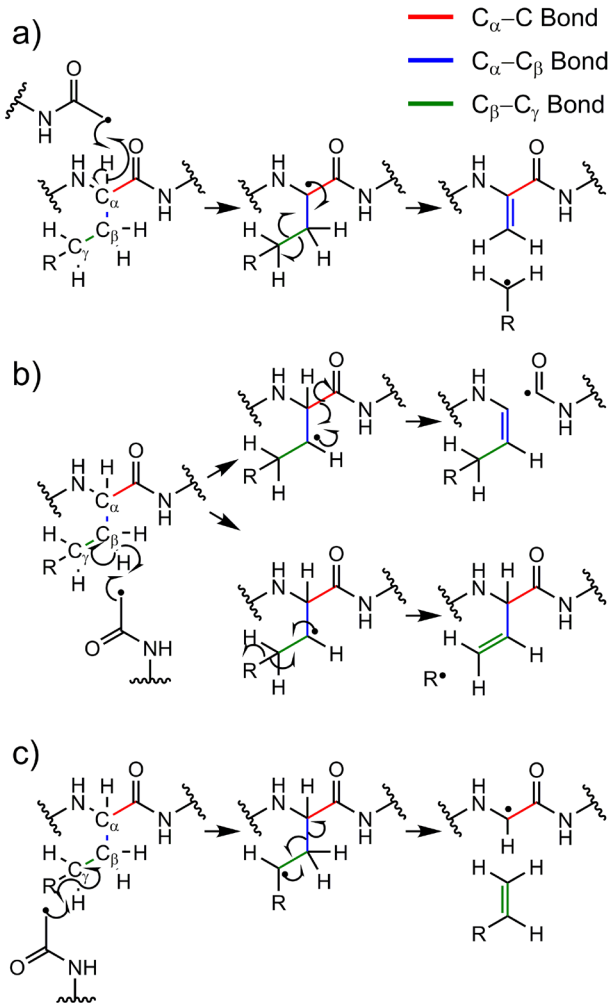

Unlike ECD and ETD, FRIPS and other hydrogen-deficient radical techniques produce primarily cleavage of C_α–C bonds and side-chain losses.[304,309,310] These products are formed by the abstraction of a hydrogen atom by the initial radical center from the backbone C_α or the side-chain C_β or C_γ position of a given amino acid residue followed by β-cleavage. As outlined in Scheme 5.2, the site of hydrogen atom abstraction generally determines the types of product ions formed. Hydrogen abstraction from C_α results in the loss of an odd-electron side-chain fragment through β-cleavage of the C_β–C_γ bond (Scheme

5.2a). The loss of an even-electron side-chain fragment results from C_γ–H abstraction through a similar process, giving a radical peptide ion (Scheme 5.2c). Backbone cleavage occurs following hydrogen abstraction from C_β, except at methionine residues, where the loss of a sulfhydryl radical is favored (Scheme 5.2b). This process is highly sensitive to amino acid side-chain chemistry, owing to subtle differences in dissociation energetics that modulate which product is favored. A study by Julian and co-workers using a noncovalently associated 18-crown-6 free radical precursor concluded that the amino acids generally fall into three main categories: (1) nonreactive residues (Ala, Gly, Pro), (2) backbone C_α–C bond cleavage residues (Asp, Asn, His, Tyr, Phe, Val, Trp), and (3) side-chain loss residues (Lys, Glu, Gln, Arg, Met, Cys, Ile, Leu).[311] The amino acid residues that primarily undergo side-chain loss or are largely unreactive tend to possess high bond dissociation energies (BDEs) for the C_β–H bond, whereas those that yield backbone C_α–C bond cleavage have comparable BDEs for the C_α–H and C_β–H bonds. This process is largely independent of the charge state of the precursor ion, as evidenced by the generation of similar product ions from either cations or anions,[311,312] suggesting that barriers for these processes are typically lower than those facilitated by a mobile proton to yield b- and y-type ions. In addition, there is evidence that C_β–H BDEs are not always sufficient to predict the observed product ions, as the initial radical position and the peptide or protein conformation can strongly influence observed dissociation pathways. For example, product ions are often formed at residues in close physical proximity to the site of radical formation in the low-energy peptide or protein conformations.[287,294,296,313,314] Alternately, the radical site may migrate multiple times (i.e., participate in several C–H abstraction processes) before achieving a configuration with a low barrier to bond cleavage.[306,315,316] These studies

indicate that the relative importance of competitive dissociation pathways are highly dependent on subtle factors that introduce small differences in activation energies.

The unique properties of hydrogen-deficient free radical chemistry have been shown to be especially useful for a wide range of specialized proteomics experiments, including the elucidation of phosphorylation sites,[317] the analysis of cysteine residues and disulfide linkages,[306,307,318] and the detection of D-amino acids.[319] The discovery of even more innovative applications of this technique is contingent upon a comprehensive knowledge of the underlying free radical reaction dynamics. To this end, the present study investigates the atypical dissociation pathways observed at serine and threonine residues in peptides. As reported by Julian and co-workers and Reilly and co-workers,[311,320] activation of hydrogen-deficient radical ions containing serine or threonine at the n^{th} residue from the N-terminus and m^{th} residue from the C-terminus results in the formation of $[a_{n-1}+H]^{\bullet}$ and z_m ions, as well as c_{n-1} and $[z_m-H]^{\bullet}$ ions. However, no compelling rationale has been proposed for the formation of these products in preference to the more commonly observed a_n and $x_{m+1}{}^{\bullet}$ ions. This work posits that the hydrogen bonding capabilities of the serine and threonine moieties lead to a number of novel dissociation pathways following hydrogen atom abstraction from either C_α or C_β. Specifically, a simple hydrogen bonding interaction alters the relative activation energies for competitive dissociation pathways by stabilizing the transition state, either by optimizing orbital overlap to yield π bond formation via $N-C_\alpha$ bond cleavage or through accessing a hydrogen atom transfer intermediate. The sensitivity of these low-barrier free radical dissociation pathways to alterations in the free energy landscape via noncovalent interactions is a key distinction between free-radical-initiated biomolecule dissociation and standard collisional activation methods.

5.3 Methods

5.3.1 Materials

The model peptides AARAAAAAA, AARAAMAHA, AARAAASAA, AARAAATAA, AARAASATA, AATAAARAA, and AARAAAT(OMe)AA (where T(OMe) denotes a methylated threonine residue) were purchased as crude synthesis products (minimum 70% purity) from Biomer Technology (Pleasanton, CA, USA). HPLC grade methanol, acetonitrile, and water were purchased from EMD Merck (Gibbstown, NJ, USA). For desalting, 10 μL pipet ZipTips with 0.6 μL C_{18} resin were purchased from Millipore Corp (Billerica, MA, USA). All other chemicals were purchased from Sigma-Aldrich (St. Louis, MO, USA).

5.3.2 Synthesis of TEMPO-Based FRIPS Reagent

The TEMPO-based FRIPS reagent recently developed by Sohn and co-workers in this group, based upon the procedure outlined by Lee and co-workers,[305] was synthesized and employed for free radical generation.[306] Full synthesis details can be found elswhere.[321] Briefly, the FRIPS reagent was synthesized starting with methyl 2-bromoacetate, to which the TEMPO (2,2,6,6-tetramethylpiperidine-1-oxyl) reagent was coupled to give methyl 2-(2,2,6,6-tetramethylpiperidin-1-yloxy)acetate. This compound was then converted to 2-(2,2,6,6-tetramethylpiperidin-1-yloxy)acetic acid by stirring in 2 M potassium hydroxide in tetrahydrofuran for 24 h. The free acid was then activated by mixing with trifluoroacetic-*N*-hydroxysuccinimide ester in dry *N*,*N*-dimethylformamide for 24 h to yield 2,5-dioxopyrrolidin-1-yl 2-(2,2,6,6-tetramethylpiperidin-1-yloxy)acetate, the desired TEMPO-based FRIPS reagent.

5.3.3 Peptide Conjugation

Approximately 20 μg of peptide and 100 μg of the TEMPO-based FRIPS reagent were dissolved in 20 μL of a 50 mM triethylammonium bicarbonate solution (pH 8.5) in 50/50% (v/v) acetonitrile/water. The conjugation of the radical precursor to the peptide was allowed to progress for 2 h before quenching the reaction by the addition of 10 μL 25% (w/w) hydroxylamine hydrochloride in H_2O to reverse any derivatization of the hydroxyl groups. The solvent was then removed with use of a centrifugal evaporator, and the peptide was resuspended in 0.1% (v/v) trifluoroacetic acid in H_2O. The solution was desalted using Millipore C_{18} ZipTips according to the manufacturer's instructions. The 5 μL elution solvent containing approximately 5 μg of peptide was brought to a final volume of 250 μL in a 50/50/0.1% (v/v) solution of methanol/water/formic acid and was electrosprayed directly into the mass spectrometer. The acquired mass spectrum demonstrated 95% or greater derivatization of the peptide with the FRIPS reagent for all peptides examined.

5.3.4 Mass Spectrometry

Experiments were performed on an LCQ Deca XP quadrupole mass spectrometer (Thermo-Fisher, Waltham, MA, USA). Peptide solutions were infused directly into the electrospray source of the mass spectrometer by a syringe pump at a flow rate of 3 μL/min. An electrospray voltage of 3.5 kV, capillary voltage of 41-42 V, capillary temperature of 275 °C, and tube lens voltage of -40 to -60 V were used. Other ion optics parameters were optimized by the autotune function in the LCQ tune program for maximizing the signal intensity. The precursor isolation window for MS^n experiments was set to 3.0 m/z, and the normalized collisional energy in the LCQ tune program was varied from 26% to 30%

according to residual precursor ion intensities. Spectra were recorded for 50 or 100 scans based upon signal intensity.

5.3.5 Computational Methods

Seven structures were chosen as simple model systems for the study of the dissociation pathways of threonine. The molecules 2-acetamido-3-hydroxy-*N*-methylbutanamide, 2-acetamido-3-methoxy-*N*-methylbutanamide, and 2-acetamido-3,*N*-methylbutanamide were utilized as models for threonine, *O*-methylthreonine, and valine, respectively. These structures were composed of amino acids with an additional N-terminal acetyl group and C-terminal methylated amine and were employed to investigate the energetics of N−C_α and C_α−C bond cleavage with an initial radical center at C_β (Figure 5.3a, b, d). The threonine and *O*-methylthreonine model structures were also optimized with a radical centered at C_α to examine loss of water or methanol from the side-chain (Figure 5.3c,e, respectively). Finally, the alanine-based structures 2-acetamidopropanimide and 2-acetamido-*N*-(prop-1-en-2-yl)propanamide were utilized for the examination of cleavage of the C_α−C bond beginning from a nitrogen-centered radical (Figure 5.3f, g).

Initial geometries for each molecule were generated by MC/MM conformer search with OPLS 2005 as the force field using Macromol 8.0 as implemented in Maestro 8.0 (Schrödinger Inc., Portland, OR, USA) under the Linux environment. All initial structures falling within 5 kcal/mol of the lowest-energy structure were recorded and examined. Conformation space of the radical for each system was searched by substitution of the carbon radical center with boron to simulate the trigonal bonding environment. Candidate structures from these simulations were then screened manually to avoid redundancy, and

the boron atom was replaced by a carbon radical site for further optimization utilizing density functional theory (DFT) with Jaguar 7.5 (Schrödinger Inc., Portland, OR, USA) at the B3LYP/6-31+G(d) level of theory. By monitoring the occurrence of imaginary vibrational frequencies, only nontransition state structures (i.e., no imaginary vibrational frequencies) were further optimized using a higher basis set at the B3LYP/6-311++G(d,p) level.

To obtain an initial potential energy surface for each reaction, the energetics of the bond dissociation process being examined were explored by geometry optimization at fixed bond distances (i.e., relaxed coordinate scan) with a step size of 0.1 Å at the B3LYP/6-31+G(d) level of theory. After visualization in Molden,[322] transition state structures were determined by a standard transition state search at the B3LYP/6-311++G(d,p) level of theory from the highest-energy conformer found, and observation of the correct transition state was confirmed by IRC calculations. Generally, only the transition state for cleavage of the bond of interest was found, as well as the energies of the products. Small barriers due to rotations about a bond or noncovalent interactions were not investigated, except in the case where the transition state for bond cleavage was separated from the enthalpy of reaction by a noncovalent complex of the product ions.

The single point energy for each structure was also calculated using the M05-2X and M06-2X density functionals with the 6-311g++G(d,p) basis set. The two new-generation meta-hybrid functionals other than B3LYP were chosen for their ability to reliably predict the energetics of organic radical reactions, as well as their strong performance in assessing hydrogen bond interactions and dipole moments.[323-325] Thermochemical corrections (zero point energy plus thermal internal energy) were calculated with the B3LYP/6-311++G(d,p)

basis set at 298 K and applied to SCF calculations from all utilized density functionals. Charges derived from the electrostatic potential and Mulliken populations were calculated for selected molecules using Jaguar, and natural atomic charges were calculated using NBO 5.0 (Theoretical Chemistry Institute, University of Wisconsin, Madison, WI) at the B3LYP/6-311g++G(d,p) level of theory. All optimizations were performed using the spin unrestricted methodology, and the spin contamination was found to be small (S^2<0.782). All calculations were performed using computational resources kindly provided by the Material and Process Simulation center at the Beckman Institute, Caltech.

5.4 Experimental Results and Discussion

5.4.1 Unique Product Ions Observed at Serine and Threonine

Peptide ions derivatized by the TEMPO-based FRIPS reagent were collisionally activated to provide precursors for studies of hydrogen-deficient radical-driven dissociation. The use of the TEMPO-based reagent greatly improves the signal intensity of FRIPS spectra over the previously employed Vazo 68 FRIPS reagent by eliminating an additional stage of MS/MS experiments (Scheme 5.1). In all experiments presented in this work, the singly protonated peptide derivatized with the TEMPO-based reagent was isolated and subjected to CID, producing the acetyl radical peptide ion (right-hand side of Scheme 5.1). Further dissociation of this species by collisional activation (i.e., MS^3) produced the desired FRIPS spectrum.

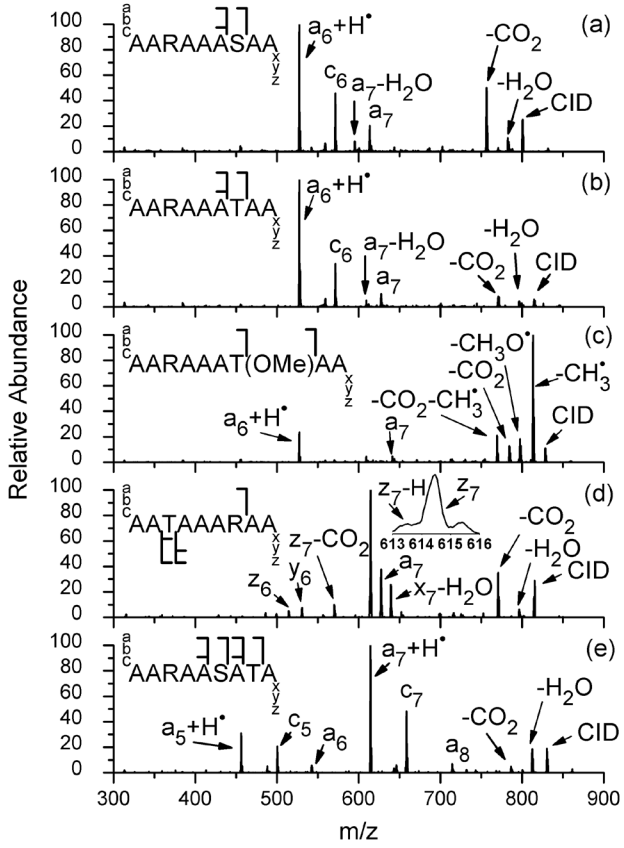

Figure 5.1. Free radical chemistry of serine and threonine in model peptides. For both serine (a) and threonine (b), the spectra are dominated by the formation of $[a_6+H]^{\bullet}$ and c_6 ions, instead of the more typical a_7 ion and side-chain losses. Reaction at threonine is more prominent than at serine, as seen in (e). Methylation of the hydroxyl group of threonine (c) prevents c_6 ion formation. The FRIPS spectrum of a model peptide with the threonine and arginine residues transposed to place the charge site on the C-terminal side of threonine (d) yields the z_7, $[z_7-H]^{\bullet}$, and x_7-H_2O ions.

Parts a and b of Figure 5.1 show the FRIPS spectra of AARAAASAA and AARAAATAA, respectively. Contrary to the expected dissociation to yield a ions or side-chain losses typically observed in FRIPS spectra, reaction at serine or threonine generates the $[a_6+H]^{\bullet}$ and c_6 ions as the dominant products, with minor formation of the a_7 ion. These atypical product ions, whose assignment was confirmed by MS^n experiments, cannot be explained by the general mechanisms outlined in Scheme 5.2. Also notable is a small

amount of water loss and a_7-H_2O ions, which have been observed previously in free radical reactions at serine and threonine.[320] Although the FRIPS spectra for these two model peptides are nearly identical, there is a significant difference in the abundance of CO_2 loss, which can be attributed to a difference in reactivity between serine and threonine. The FRIPS spectrum of AARAASATA shown in Figure 5.1e further highlights this disparity, with a significantly higher abundance of product ions from reaction at threonine than serine. These differences in reactivity were investigated using DFT calculations on model systems, and it was found that the activation energy for the rate-limiting β-cleavage reactions was systematically higher for serine than threonine due to the absence of the stabilizing methyl group on the side chain.[321]

To further investigate the mechanism of formation of these atypical product ions, the transposed sequence of the threonine model peptide, AATAAARAA, was examined. The FRIPS spectrum shown in Figure 5.1d is dominated by the formation of the z_7 ion, with the $[z_7-H]^{\bullet}$ (inset), a_7, and x_7-H_2O ions also of notable abundance. The y_6 ion is likely formed from dissociation of the z_7 species, as this ion is prominently observed upon collisional activation of the z_7 ion. The a_7 ion results from β-cleavage of the $C_\alpha-C$ bond at the arginine residue, a process that gave negligible yields of the a_3 ion in the model peptides possessing an arginine near the N-terminus. This difference can again be attributed to the somewhat regioselective nature of the FRIPS reagent. Similarly, the increased abundance of CO_2 neutral loss can be attributed to the decreased accessibility of the reactive threonine residue to the radical site. However, given that the most prominent ions in the spectrum occur from the threonine residue near the C-terminus, the chemical properties of the various moieties

on the peptide are more influential than amino acid position in determining product ion yields.

In explaining the atypical free radical chemistry of serine and threonine, attention is naturally focused on the hydroxyl group, which not only serves as a key site for modifying protein structure and function through PTMs but also has the ability to affect protein stability directly by hydrogen bonding. To determine the role this functional group plays in observed dissociation patterns, the threonine residue in the model peptide was modified by methylation of the hydroxyl group and examined using FRIPS. As shown in Figure 5.1c, the FRIPS spectrum is dominated by the loss of a methyl radical. This process likely occurs by hydrogen abstraction from C_β of the *O*-methylthreonine residue followed by β-cleavage of the O−CH_3 bond, resulting in the formation of a stable ketone product. Similarly, the neutral loss of the methoxy radical ($CH_3O^\bullet$) can be explained by hydrogen abstraction from C_α of *O*-methylthreonine and subsequent β-cleavage of the C−OCH_3 bond. Interestingly, the c_6 ion is completely absent from the spectrum, implicating the necessity of the hydroxyl group for formation of this ion. In contrast, the $[a_6+H]^\bullet$ ion is still present, although its relative abundance is decreased, possibly due to competition with the more favorable loss of the methyl radical. The a_7 ion is similarly present with decreased relative intensity.

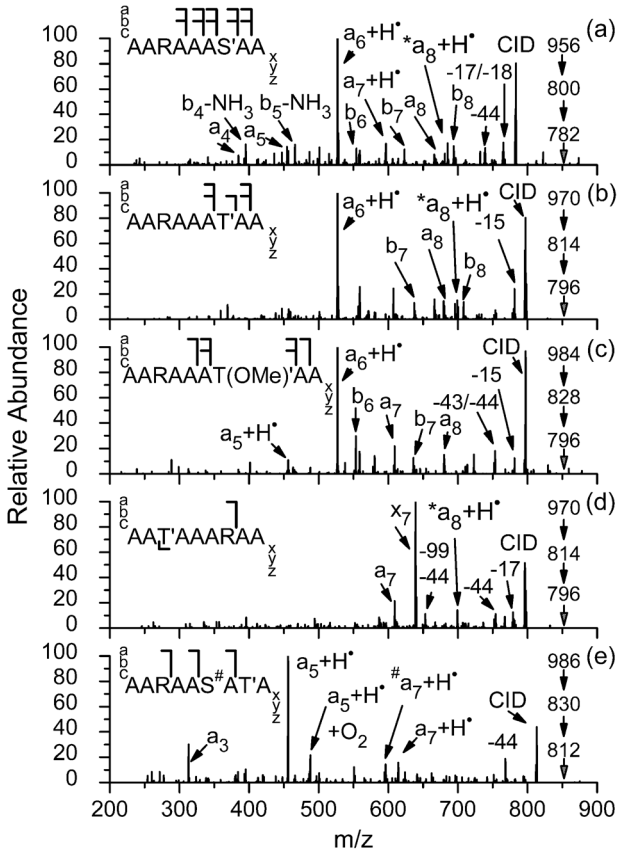

Figure 5.2. Collisional activation (MS^4) of the water neutral loss from model serine and threonine peptides. Each spectrum is dominated by a prominent product ion, either the $[a_{n-1}+H]^{\bullet}$ ion or the x_7 ion. All product ion identifications include loss of water from serine or threonine, except those marked with *, and in (e), where # explicitly denotes water loss from serine.

The presence of the x_7-H_2O ion in such great abundance in the FRIPS spectrum of AATAAARAA (Figure 5.1d) is rather unexpected, indicating that a favorable dissociation pathway exists for $C_\alpha-C$ bond cleavage coupled with water loss, likely from the threonine side-chain. To further investigate the water loss pathway, MS^4 experiments were performed on the neutral loss of water from each of the model peptides, as shown in Figure 5.2. In each case, the spectrum predominantly consists of a single ion, either the $[a_{n-1}+H]^{\bullet}$ ion when an N-terminal charge site is present, or the x_m ion when there is a C-terminal charge

site. Interestingly, the MS^4 spectrum of AARAASATA (Figure 5.2e) shows a much greater abundance of the $[a_5+H]^{\bullet}$ ion than the $[a_7+H]^{\bullet}$ ion, suggesting that the neutral loss of water occurs largely from serine rather than threonine in this case. However, whether this trend is due to peptide structural constraints or the inherent differences in the chemistry of the serine and threonine side chains is not clear from these data. Overall, these results reveal multiple reaction pathways to the $[a_{n-1}+H]^{\bullet}$ ion that generate distinct C-terminal product ions, further highlighting the complex free radical chemistry of serine and threonine.

5.4.2 Proposed Mechanism of Reaction at Serine and Threonine Residues

It is clear from the experimental results that the common processes of C_α–C bond cleavage (from a C_β-centered radical) and side-chain loss (from a C_α-centered radical) are replaced by distinct lower-energy dissociation pathways at serine and threonine. Scheme 5.3 outlines the proposed mechanisms by which the novel product ions shown in Figure 5.1 are formed. All of these mechanisms posit that the presence of hydrogen bonds between the side-chain hydroxyl group and backbone amide group enables new dissociation pathways by accessing energetically favorable fragmentation processes. In spite of the relative weakness of the hydrogen bonds (~5 kcal/mol)[326-329] in comparison to the cleaved covalent bonds, these interactions are capable of significantly altering the energetic landscape by guiding access to and stabilizing transition states for otherwise noncompetitive dissociation reactions.

Scheme 5.3. Proposed Mechanisms of Free-Radical-Initiated Dissociation at Serine and Threonine Residues

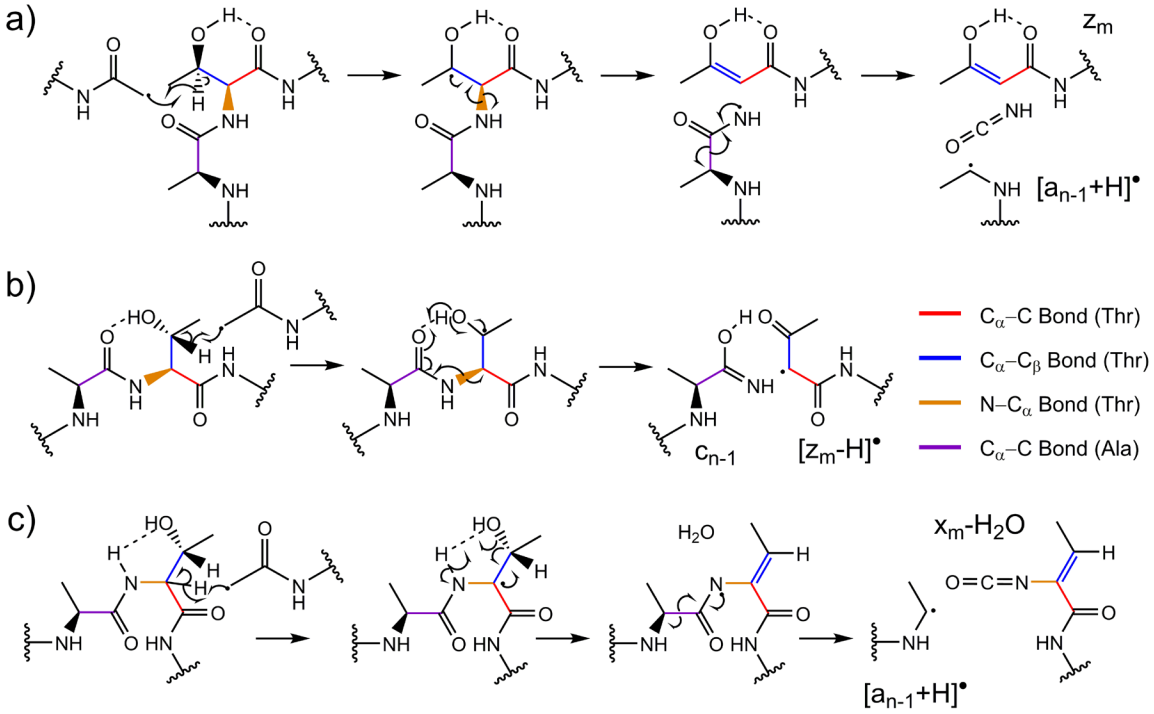

The $[a_{n-1}+H]^\bullet$ ion is proposed to form as a result of hydrogen bonding between the C-terminal carbonyl oxygen and the hydroxyl group, forming a six-membered ring that stabilizes the reaction intermediate, as illustrated in Scheme 5.3a. Due to the favorable interactions between the hydroxyl group and the carbonyl oxygen, the energy required to cleave the N−C_α bond is lowered, leading to preferential β-cleavage. This process gives the z_m ion and a $c_{n-1}^\bullet$ ion that rapidly loses isocyanic acid to give the observed $[a_{n-1}+H]^\bullet$ ion. The dominance of the $[a_{n-1}+H]^\bullet$ (Figure 5.1a,b) and z_m ions (Figure 5.1d) in the FRIPS spectra suggest that this pathway should be the most energetically favored. The hydroxyl group of serine or threonine may alternately form a seven-membered ring through hydrogen bonding with the N-terminal carbonyl oxygen atom, as shown in Scheme 5.3b.

This conformation facilitates hydrogen atom transfer from the hydroxyl group in conjunction with hydrogen abstraction from C_β. As the $N-C_\alpha$ bond is elongated, the transfer of the hydrogen atom occurs in a concerted manner, reducing the reaction barrier and yielding an enol-imine c_{n-1} ion and the C_α-centered radical $[z_m-H]^\bullet$ ion. This hydrogen atom transfer process is supported by the experimental observation that methylation of the threonine hydroxyl group eliminates formation of the c_{n-1} ion. Both of these mechanisms are in agreement with those proposed by Sun et al. for the formation of c_{n-1} and radical a_{n-1} ions at serine and threonine residues through hydrogen-deficient radical dissociation from a crown ether-based photolabile radical precursor, but the importance of the hydrogen bonding interactions has not been previously demonstrated.[311]

As evidenced by the formation of $[a_{n-1}+H]^\bullet$ ions in the absence of a hydrogen bond donor (Figure 5.1c) as well as the formation of $[a_{n-1}+H]^\bullet$ and x_m-H_2O ions following neutral loss of water (Figure 5.2), a third dissociation pathway must be considered at serine and threonine residues. In the mechanism proposed in Scheme 5.3c, the hydroxyl group of serine or threonine acts as hydrogen bond acceptor instead of donor, leading to a strong interaction with the N-terminal amide hydrogen. Following hydrogen abstraction from C_α by the acetyl radical, the new radical center may undergo β-cleavage in concert with hydrogen abstraction from the backbone amide nitrogen, yielding a neutral loss of water and a nitrogen-centered radical. This nitrogen-centered radical may then undergo further β-cleavage of the N-terminal $C_\alpha-C$ bond to yield the observed $[a_{n-1}+H]^\bullet$ and x_m-H_2O ions. A similar mechanism was previously proposed by Reilly and co-workers in their examination of the collisional activation of radical a ions produced by 157 nm photodissociation.[320] Importantly, this mechanism offers an explanation for the formation

of the $[a_{n-1}+H]^{\bullet}$ ion even when the hydroxyl group of threonine is methylated (Figure 5.1c), as the methoxy group may still act as hydrogen bond acceptor and yield the nitrogen-centered radical via loss of methanol.

5.5 Computational Analysis

5.5.1 Models for Serine and Threonine Free Radical Chemistry

Given the strong experimental evidence for the mechanisms proposed in Scheme 5.3, in both this work and previous studies,[311,320] we investigate these reactions utilizing computational techniques to better understand the free radical chemistry of serine and threonine. The C_{β}-centered radical structures shown in Figure 5.3a,b,d were employed to examine cleavage of the N−C_{α} and C_{α}−C bond via β-cleavage, and the C_{α}-centered radicals in Figure 5.3c,e were used to explore the neutral loss of water from the side-chain. Finally, the nitrogen-centered radicals shown in Figures 5.3f,g were used to study β-cleavage of the C_{α}−C bond. The structures shown beneath the schematic diagram for each molecule represent the low-energy conformer or conformers found for that compound, with the relative enthalpy (B3LYP/6-311++G(d,p) level of theory) indicated for molecules with multiple low-energy conformations of interest.

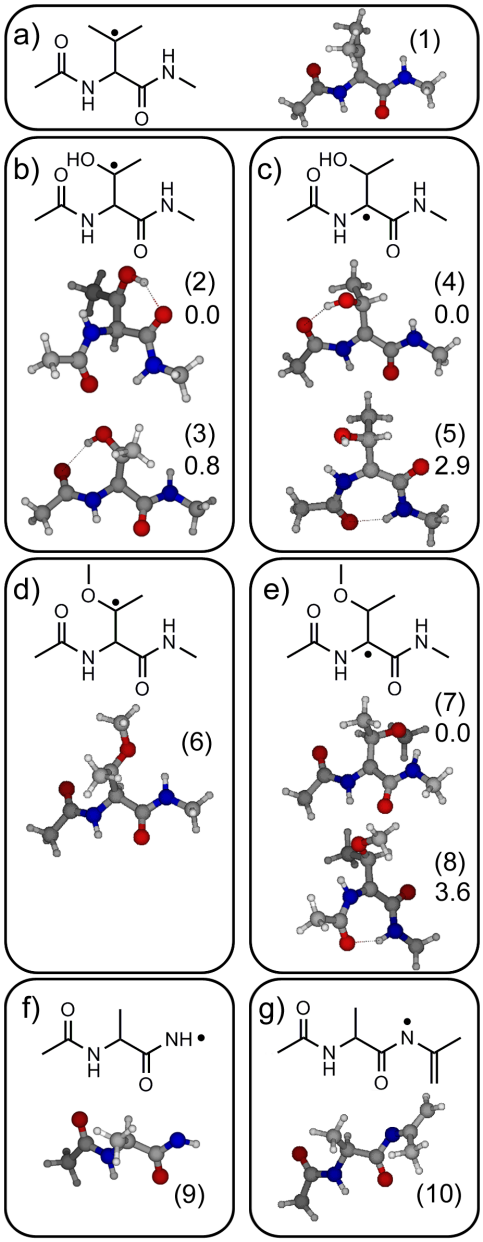

Figure 5.3. Model structures for computational investigation of threonine free radical chemistry. The structures of compounds possessing a C_β-centered radical are shown for valine (a), threonine (b), and *O*-methylthreonine (d), whereas those possessing a C_α-centered radical are shown for threonine (c) and *O*-methylthreonine (e). The final two compounds (f and g) were utilized to study C_α–C bond cleavage from a nitrogen-centered radical. Relative enthalpies [B3LYP/6-311++G(d,p)] are indicated for multiple structures. Hydrogen bonding interactions are denoted with dashed lines (see text for further discussion).

For all bond cleavage processes examined, the reaction energetics were calculated using the M05-2X and M06-2X density functionals as well as B3LYP. These functionals give reaction enthalpies differing by as much as 13 kcal/mol for β-cleavage processes, with slightly smaller differences for activation energies. Previous work by Izgorodina et al. demonstrated that B3LYP may underestimate the energetics of β-cleavage reactions by up to 9 kcal/mol.[330] The M05-2X and M06-2X density functionals are expected to be significantly more accurate for these reactions, although they were found to overestimate energetics of β-cleavage by ~2 kcal/mol compared to G3(MP2)-RAD benchmarks.[325] These results suggests that the computational energetics presented here likely represent upper and lower bounds on the actual thermochemistry.

5.5.2 β-Cleavage of the N−C_α vs C_α−C Bond

To investigate the favored β-cleavage of the N−C_α bond over the C_α−C bond from a radical centered at C_β (Scheme 5.3a,b), the energetics for these processes were calculated for valine, serine, and threonine model compounds (Figure 5.4). The energetics for the valine model compound shown in Figure 5.4a provide reference dissociation energetics in the absence of hydrogen bonding. The low-energy conformer (**1**) has the backbone in the all-trans configuration with the side-chain oriented perpendicular to the backbone. Cleavage of the C_α−C bond was found to be favored over N−C_α bond cleavage by 6−10 kcal/mol depending on the density functional. Dissociation of the N−C_α bond proceeds through a transition state in which a stabilizing hydrogen bond interaction between products is preserved, yielding an energetic minimum between dissociation transition state and overall reaction enthalpy of the separated products (right-hand side of Figure 5.4a).

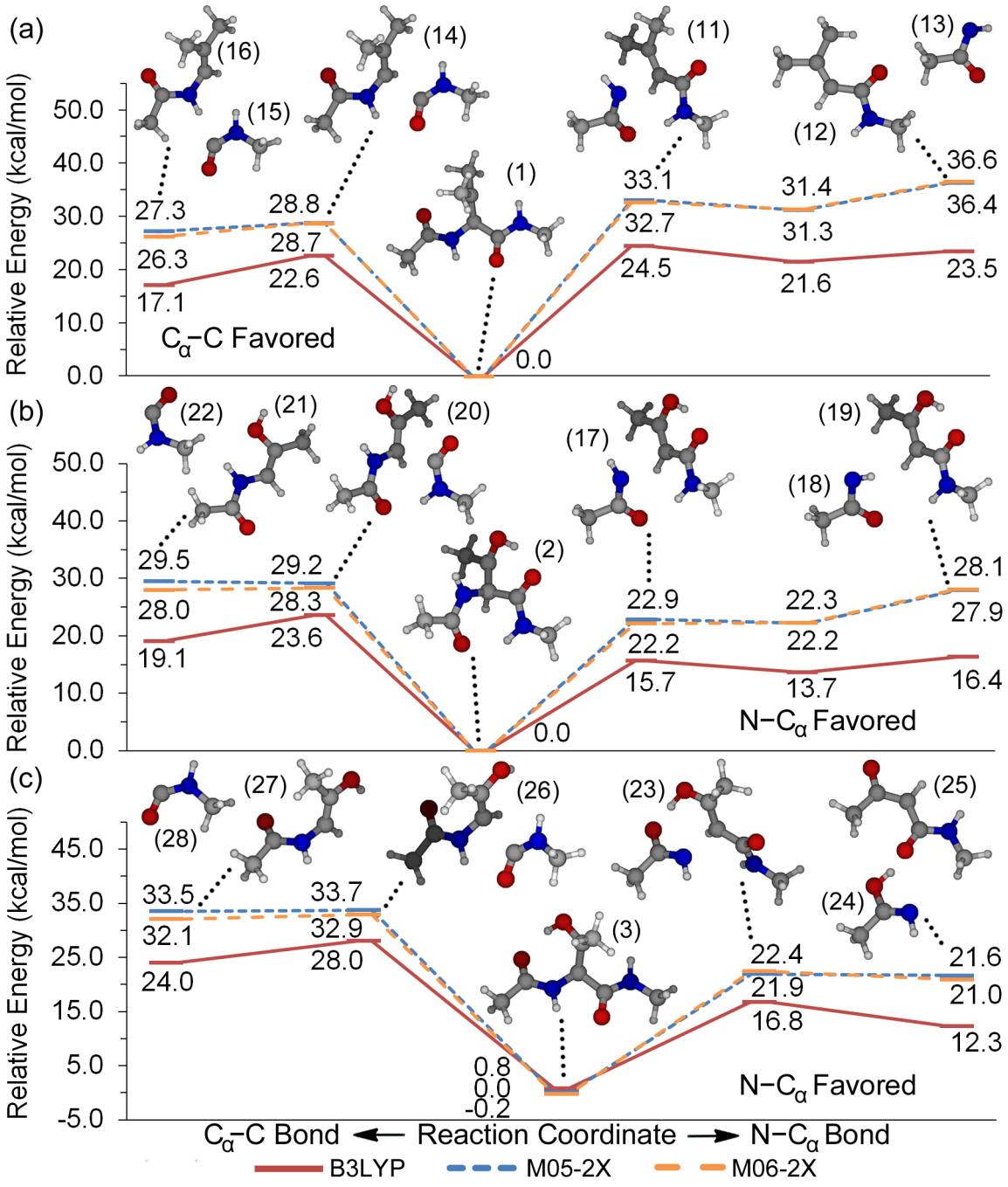

Figure 5.4. β-cleavage of the N–C_α vs C_α–C bond from a C_β-centered radical on model amino acids. For the valine model compound (a), dissociation of the C_α–C bond is favored, whereas hydrogen bonding in threonine (b and c) favors N–C_α bond cleavage via stabilization of the reaction intermediate. Enthalpies are given relative to structure **1** for the valine molecule and structure **2** for the threonine molecule.

Two low-energy structures were found for the threonine model compound possessing a radical center at C_β (Figure 5.3b), and both conformers were examined to obtain reaction energetics as shown in Figure 5.4b,c. These two structures possess an all-trans backbone conformation, and the side-chain hydroxyl group forms a hydrogen bond with either the C-terminal (**2**, 0.0 kcal/mol) or N-terminal (**3**, 0.8 kcal/mol) carbonyl oxygen. Although the energetics of C_α–C bond cleavage are quite similar between valine (Figure 5.4a) and the C-terminal hydrogen bonding structure of threonine (Figure 5.4b), the energy required for N–C_α bond cleavage is greatly decreased for threonine. The hydrogen bonding interactions are eliminated at the transition state for C_α–C bond cleavage (**20**) to enhance the π-orbital interactions of the N-terminal product (**22**), but the hydrogen bond persists in the transition state for N–C_α bond dissociation (**17**), reducing the energy required to form the $c^\bullet$ (**18**) and z (**19**) ion analogues of the products proposed in Scheme 5.3a. Similar to the case for the valine model compound, the loose transition state for N–C_α bond cleavage is found to be lower than the product enthalpies due to formation of a stabilizing hydrogen bond following dissociation. Though the B3LYP calculations clearly favor cleavage of the N–C_α bond over the C_α–C bond, the M05-2X and M06-2X calculations give similar reaction enthalpies for the two processes. Experimentally, product ions resulting from N–C_α bond cleavage are on the order of 10 times more abundant than those from C_α–C bond cleavage, meaning a significant difference in the reaction rates would be expected on the ion trap time scale. Previous work has demonstrated that even small differences in activation energy can have large impacts on the kinetics and branching ratios of peptide dissociation,[331,332] and dissociation of the N–C_α bond need only be slightly enthalpically favored to be the dominant product ion (assuming similar frequency factors for the two processes).

For the N-terminal hydrogen bonding structure (**3**) shown in Figure 5.4c, the preference for dissociation of the N−C_α bond over the C_α−C bond is quite clear. In this conformation, the energy required for cleavage of the N−C_α bond is significantly reduced due to the approach of the hydroxyl and carbonyl groups at the transition state (**23**) and subsequent hydrogen atom transfer to give the enol-imine (**24**) and carbon-centered radical (**25**) products (c and $[z-H]^{\bullet}$ ion analogues of Scheme 5.3b, respectively). The reaction coordinate for C_α−C bond cleavage shows that the threonine side-chain rotates during dissociation, disrupting hydrogen bonding at the transition state (**26**) and forming the N-terminal product (**27**) with the hydroxyl group oriented outward along the axis of the N−C_α bond. This N-terminal product (a ion analogue) may readily isomerize to give the lower-energy structure seen in Figure 5.4b (**21**) and thereby reduce the reaction enthalpy, but the process still remains unfavorable due to the significant activation energy required to reach the transition state (**26**). Similar energetics with slightly higher barriers for all processes were found for a model serine compound. Thus, the calculations outlined support both the data and proposed mechanism in concluding that hydrogen bond constraints favor N−C_α bond cleavage at serine and threonine residues.

5.5.3 Nitrogen-Centered Radical Chemistry via Loss of H_2O

The processes examined above fail to explain the presence of x_m−H_2O and a_n−H_2O ions. Therefore, calculations were also utilized to investigate the energetics of the mechanism shown in Scheme 5.3c, in which dissociation occurs through β-cleavage from a nitrogen-centered radical initially formed by water loss. The low-energy structures of the C_α-centered radical for the threonine and *O*-methylthreonine model compounds are shown in

Figure 5.3c,e, respectively. For both model compounds, the low-energy structures (**4** and **7**) do not possess interactions between the side-chain hydroxyl and the N-terminal amide nitrogen that would give a clear pathway to the neutral loss of water, though such structures can be found for threonine (**5**) and *O*-methylthreonine (**8**) at relative enthalpies of 2.9 and 3.6 kcal/mol, respectively. In these conformations, the side-chain oxygen acts as hydrogen bond acceptor, with the backbone N−H group functioning as hydrogen bond donor. Water loss is found to occur from these structures via concerted cleavage of the side-chain C_β−OH bond and abstraction of hydrogen from the amide nitrogen, as shown in Figure 5.5a,b. This process occurs via a tight transition state of 32-36 kcal/mol for both molecules, although the overall enthalpy of reaction in each case was favorable (10-20 kcal/mol).

Beginning from either threonine or *O*-methylthreonine, loss of water or methanol yields a nitrogen-centered radical and double bond between C_α and C_β (structures **30** and **32**, respectively). The structure shown in Figure 5.3g seeks to replicate these features in a model system to study the energetics of β-cleavage of the C_α−C bond. As illustrated in Figure 5.5c, cleavage of the C_α−C bond from the low-energy structure (**10**) was found to occur with a tight transition state but favorable reaction enthalpy as the N−C−O bond angle changes from 123° to 174° during formation of the double bond.

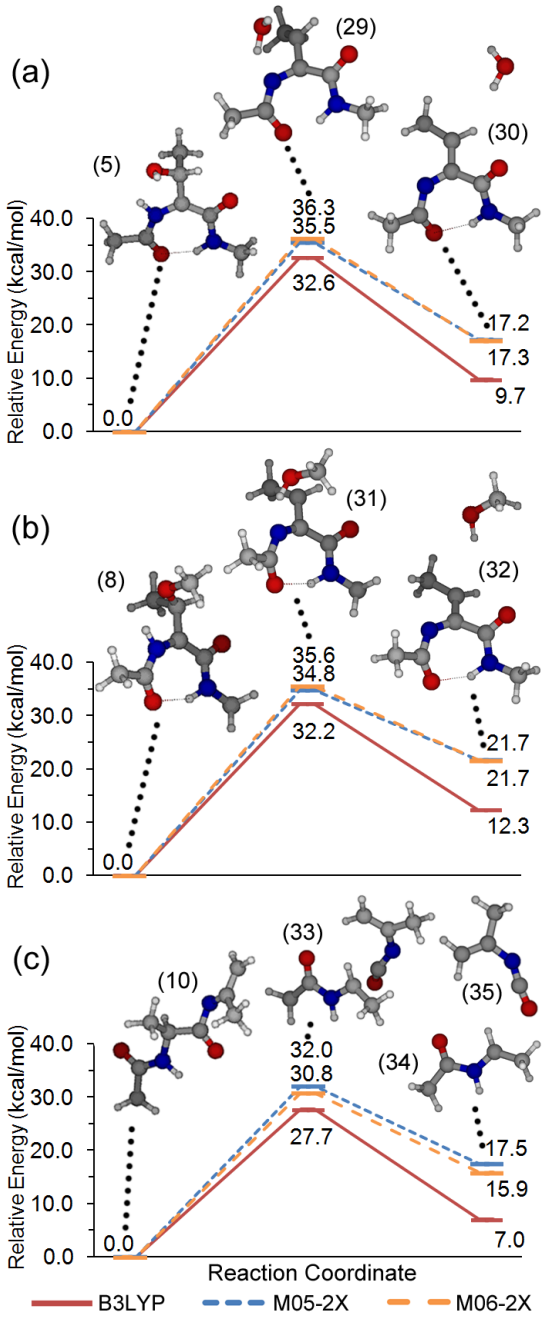

Figure 5.5. Energetics of alternate pathways to cleavage of the N-terminal C_α–C bond via formation of a nitrogen-centered radical: (a) water loss from threonine model compound; (b) methanol loss from *O*-methylthreonine model compound; (c) cleavage of C_α–C bond from nitrogen-centered radical. These processes have low reaction enthalpies but possess high activation energies.

This pathway to dissociation of the C_α–C bond is essential to explain the experimental results for the *O*-methylthreonine model peptide (Figure 5.1c). Methylation of the hydroxyl group prevents any conformation in which the side-chain acts as hydrogen bond donor, thereby suggesting that the two mechanisms presented in Scheme 5.3a,b are inoperable for this molecule. In agreement with this assertion, it was found that cleavage of the N–C_α bond via β-cleavage from the low-energy C_β-centered radical structure (**6**, Figure 5.3d) is not energetically favorable. However, β-cleavage from a nitrogen-centered radical in *O*-methylthreonine residues gives a viable route to the observed $[a_{n-1}+H]^\bullet$ ion even in the absence of a side-chain hydrogen bond donor. In addition, the energetics for this process are only slightly higher than those calculated for C_α–C bond cleavage, further supporting the feasibility of this pathway.

In the case of the threonine model compound possessing a free hydroxyl group, there exists a significant disparity between the experimental observation of the water loss pathway outlined in Scheme 5.3c and the theoretical activation energies for this reaction. The theoretical barrier to water loss of 32-36 kcal/mol is 7-14 kcal/mol higher than those calculated for the processes outlined in Scheme 5.3a,b and therefore would not be expected to compete. Since the experimental data provide compelling evidence for the proposed reaction pathway leading to water loss, especially the MS^4 spectra shown in Figure 5.2, it appears that these calculations overestimate the activation energy for this pathway. A conformation with a lower barrier to water loss may exist, but extensive conformational searching failed to yield a transition state lower in energy than the one shown in Figure 5.5a. Alternately, the activation energy for this process may be lowered by cleavage of the backbone C_α–C bond in concert with hydrogen atom transfer from the amide to the

hydroxyl group, a process somewhat analogous to that proposed in Scheme 5.3b. A concerted reaction would also explain the low abundance of water loss in the FRIPS spectra, but such processes were not examined using DFT calculations due to the difficulty in searching the expanded conformational space to identify the minimum energy pathway.

5.5.4 Why Hydrogen Bonding Favors N−C_α Bond Cleavage

Although calculations can quantify the energetics of the proposed processes leading to cleavage of the stronger N−C_α bond in the mechanisms shown in Scheme 5.3a,b, it is useful to provide a simpler but more transposable rationalization for why these reactions occur by examining the molecular orbitals involved. Strong orbital overlap connecting reactants to products is generally associated with favorable chemical reactions, whereas little overlap leads to energetically unfavorable processes.[333] Parts a and b of Figure 5.6 show schematically the interaction between the singly occupied π orbital of the C_β-radical site and the N−C_α σ bond for the N-terminal hydrogen bonding and C-terminal hydrogen bonding complexes, respectively. In either structure, the hydrogen bonding interactions strongly align the π orbital on C_β with the N−C_α σ bond, resulting in facile cleavage of the N−C_α bond. In contrast, the C_α−C σ bond lies nearly orthogonal to the π orbital on C_β in both conformations, and the cleavage of this bond is therefore unfavorable without the destruction of the stabilizing hydrogen bonding interactions.

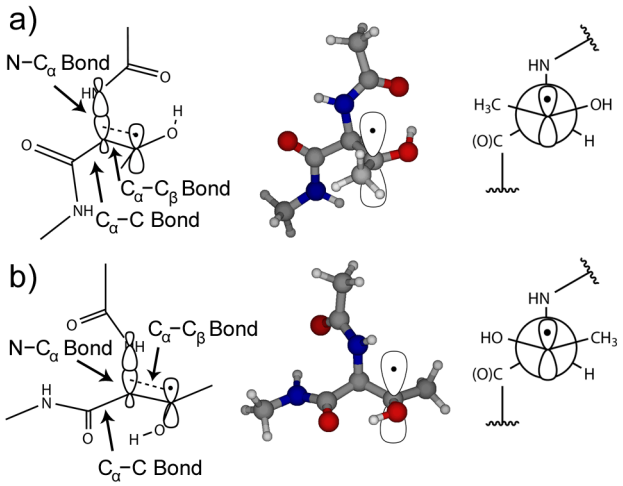

Figure 5.6. Alignment of the singly occupied π orbital on C_β with the N−C_α σ bond via hydrogen bonding interactions of threonine with either the N-terminal (a) or C-terminal (b) carbonyl oxygen. Left: schematic representation of computational structures, with orbital alignment denoted by the dashed line, Center: computational structures with schematic representation of the singly occupied π orbital on C_β, Right: Newman projection along the axis of the C_β−C_α bond.

In addition to orbital overlap, the transition state structures for both conformations are stabilized by enhanced hydrogen bonding. This observation is illustrated in Scheme 5.4, which gives the bond lengths in Angstroms for the N-terminal (a) and C-terminal (b) hydrogen bonding conformations in both the ground state (GS) and transition state (TS). In the C-terminal hydrogen bonding structure, the distance between the carbonyl oxygen and the hydroxyl group hydrogen decreases from 1.78 Å in the ground state to 1.63 Å in the transition state, imparting a stabilizing partial double bond character to the hydroxyl group. In the case of the N-terminal hydrogen bonding conformer, the hydrogen atom approaches to a distance of only 1.4 Å from the carbonyl at the transition state for N−C_α bond cleavage, forming a stabilizing intermediate with increased bond order on the side-

chain C_β–O bond. These hydrogen bonding interactions therefore play a crucial role in dictating the favored pathway of the reaction.

Scheme 5.4. Calculated Bond Lengths (Å) during N−C_α Bond Cleavage for the Threonine Model Compound Possessing an (a) N-Terminal or (b) C-Terminal Hydrogen Bond

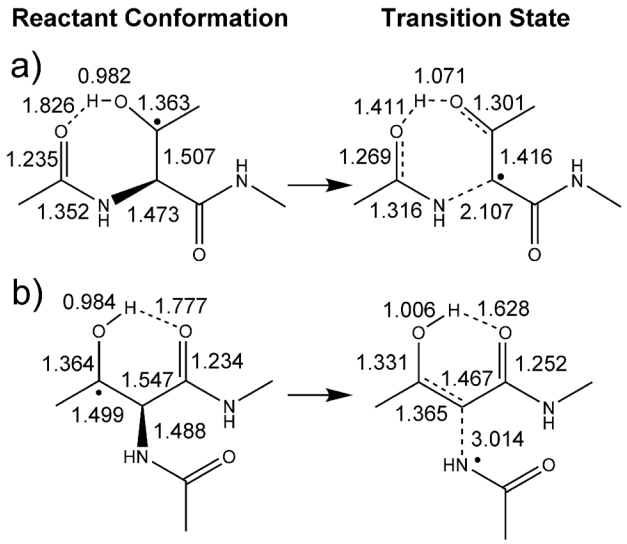

5.5.5 Comparison of FRIPS to ECD/ETD

The process of hydrogen atom transfer along with N−C_α bond cleavage (Scheme 5.3b) examined in this work gives product ions with remarkable resemblance to those observed in ECD and ETD. In the UW mechanism, which is supported by numerous experimental and theoretical reports, an aminoketyl intermediate may be formed either through direct electron capture to the amide π* orbital or through intramolecular electron transfer from electron capture in a Rydberg orbital at a positively charged site, followed by proton abstraction by the strongly basic amide anion radical.[255,265-267,275] The mechanism proposed here is more comparable to the Cornell mechanism, in which hydrogen atom transfer is suggested to form the aminoketyl intermediate, with backbone cleavage occurring

separately.[255,268,269,273] However, the proposed mechanism for radical-initiated cleavage at serine and threonine is absent of any aminoketyl intermediate, as the transfer of the hydrogen atom occurs in concert with N−C_α bond cleavage. Further examination of the potential energy surface failed to find a pathway in which aminoketyl intermediate formation was more energetically favorable than concerted hydrogen atom transfer and N−C_α bond cleavage, making this dissociation mechanism unlikely for this system. In addition, the Cornell mechanism is unlikely to be prevalent in ECD and ETD, as the energetic barriers to hydrogen atom transfer are greater than those to intramolecular electron transfer followed by proton abstraction.[255,260] Although not directly applicable to the ECD or ETD case, the hydrogen atom transfer observed here is interesting in that it illuminates yet another unique mechanism for the cleavage of backbone N−C_α bonds via a decrease in the energetic requirements for this process.

5.6 Conclusions

The calculations and experiments detailed in this work provide a comprehensive analysis of the factors responsible for the unique free radical chemistry of serine and threonine. Cleavage of the N−C_α bond may occur directly via β-cleavage from a C_β-centered radical, whereas dissociation of the N-terminal C_α−C bond may occur either from a nitrogen-centered radical or by loss of isocyanic acid following N−C_α bond cleavage. As a result of the lower energetic barriers associated with odd-electron versus even-electron cleavage processes, these reaction pathways are more susceptible to influence by weak interactions such as hydrogen bonding that constrain molecular geometry in reactants, intermediates, and products. This principle has significant implications for gas-phase free radical

sequencing applications, in which many peptides and proteins may possess stable gas-phase noncovalent interactions that may direct radical-induced dissociation, an attribute that Julian and co-workers have leveraged to elucidate the gas phase structure of proteins.[294,296,313] In other situations, such effects may be masked by rapid migration of the radical site following formation.[315] Nevertheless, it is abundantly clear from this work that free radical chemistry can be highly sensitive to local conformation at the radical site, as no fewer than five unique dissociation pathways can occur at serine and threonine residues via dissociation from different conformations.

Chapter 6

Separation and Identification of Peptide Isomers by Free-Radical-Initiated Peptide Sequencing (FRIPS) Combined with Ion Mobility-Mass Spectrometry

(Reproduced in part with permission from Mui, W.; Thomas, D. A.; Downard, A. J.; Beauchamp, J. L.; Seinfeld, J.. H.; Flagan, R. C. *Anal. Chem.* **2013**, *85*, 6319-6326. http://dx.doi.org/10.1021/ac400580u Copyright 2013 American Chemical Society.)

6.1 Abstract

Complex mixtures of peptides with strong sequence homogeneity are often challenging to separate by high performance liquid chromatography. However, ion mobility spectrometry (IMS) provides another dimension of analyte separation that is capable of resolving highly similar peptide structures. This study demonstrates the application of a novel classification device, the radial opposed migration ion and aerosol classifier (ROMIAC), to the separation of peptide isomers. The ROMIAC is coupled to the atmospheric pressure interface of a linear trap quadrupole mass spectrometer, and monitoring distinct dissociation pathways associated with peptide isomers fully resolves overlapping features in the ion mobility data. We find that the addition of the reagent for free-radical-initiated peptide sequencing (FRIPS) to the N-terminus of isomeric peptides improves separation by altering gas-phase peptide structure. The ability of the ROMIAC to operate at atmospheric pressure and serve as a front-end analyzer to continuously transmit ions with a particular mobility facilitates its utilization in a variety of experimental protocols in which additional analyte separation is required.

6.2 Introduction

The field of proteomics has advanced rapidly in the past decade with the development of both novel instrumentation and new experimental techniques.[334,335] The combination of mass spectrometry (MS) methods that simultaneously enable high resolution, mass accuracy, and sensitivity with techniques for improved analyte separation through high performance liquid chromatography (HPLC) or capillary electrophoresis has enabled the analysis of increasingly intricate samples and yielded valuable insight into a vast array of cellular processes.[336-341]. In spite of these improvements, many challenges to the analysis of complex samples remain. For example, many isomeric peptides cannot be separated in standard HPLC columns, precluding sequence identification by HPLC-MS.[342-344] In addition, traditional collision-induced dissociation (CID) experiments often lead to loss of post-translational modifications (PTMs), such as phosphorylation or nitrosylation, hindering the identification of modified amino acid residues.

Several recent developments in the dissociation of gas-phase peptide ions offer improved capabilities for peptide sequencing. The advent of electron capture dissociation (ECD) and electron transfer dissociation (ETD) has greatly enhanced the ability of proteomics experiments to identify PTMs, as these dissociation methods typically cleave selectively at N-C_α bonds and leave side chain modifications intact.[245,249-251,280,345,346] However, these techniques have their own experimental limitations, including inefficient dissociation, especially for low charge-state peptides. Free-radical-initiated peptide sequencing (FRIPS) is an alternative method for the gas-phase sequencing that gives information complementary to that obtained by traditional CID or ECD/ETD experiments.[304] In this

technique, a free radical precursor is attached to the N-terminus of a peptide or protein. When the derivatized peptide is subjected to collisional activation, homolytic bond cleavage adjacent to the free radical precursor generates an acetyl radical at the N-terminus of the peptide, which subsequently initiates dissociation of the peptide by hydrogen atom abstraction from various sites along the peptide backbone. As with other radical-directed dissociation techniques, the product ions formed are highly sensitive to the $C_\beta-H$ bond dissociation energy (BDE) of each amino acid residue, with residues possessing high $C_\beta-H$ BDEs preferentially generating side chain loss and those with low $C_\beta-H$ BDEs leading to backbone dissociation.[248,311]

In the separation of complex mixtures prior to dissociation, ion mobility spectrometry (IMS) adds another useful dimension of separation between HPLC and MS analysis. A wide range of methodologies have been successfully employed to separate peptide and other complex biological mixtures, including drift cells,[347,348] traveling wave ion mobility cells,[349] high-field asymmetric waveform devices (FAIMS),[350] and differential mobility analyzers (DMA).[351,352] These techniques have unique advantages and limitations, but many of them require significant new instrumentation that is costly to build and implement.

The opposed migration aerosol classifier (OMAC) is a new instrument that operates with equipotential inlet and outlet flows, reducing loss of ions and particles due to electric field distortions.[353] The OMAC employs parallel porous or screen electrodes and can readily be integrated with the atmospheric pressure interface of a mass spectrometer. A gas cross-flow enters and exits the classification region through porous electrodes within the classification region, exerting a drag force on translating ions or particles. Mobility

classification is accomplished by balancing this drag force with the force from an electric field applied antiparallel to the gas flow. The use of antiparallel drag and electric forces increases the distance that particles or ions must diffuse to degrade instrument resolution, improving instrument performance. A radial geometry further decreases diffusional losses and enhances resolution by elimination of electric field deformities from proximate dielectric walls. We refer to the instrument as a radial opposed migration ion and aerosol classifier (ROMIAC).

The ability of the ROMIAC to classify ions with high transfer efficiency makes it well-suited for the analysis of biological samples, especially peptides, which possess mobility diameters on the order of a single nanometer. This study combines this novel front-end classifier with peptide derivatization by the FRIPS reagent to achieve improved peptide separation prior to sequence analysis by mass spectrometry. Specifically, the ROMIAC is utilized to separate several isomeric peptide samples as a demonstration of the ability of this instrument to improve analysis of peptide samples with significant sequence homogeneity. The addition of the FRIPS reagent to the peptides is found to enhance peptide isomer separation through alterations in gas-phase peptide structure.

6.3 Methods

6.3.1 Materials

High-purity methanol was obtained from J. T. Baker Avantor (Center Valley, PA), and high-purity water as well as ACS grade glacial acetic were purchased from EMD Millipore (Billerica, MA). The model peptides AARAAATAA, AATAAARAA, AARAAHAMA, and AARAAMAHA, were obtained from Biomer Technologies (Pleasanton, CA) and used without further purification.

6.3.2 Synthesis of TEMPO-based FRIPS Reagent

The (2,2,6,6-tetramethylpiperidin-1-yl)oxyl (TEMPO)-based FRIPS reagent recently developed by Sohn and co-workers, based upon the procedure outlined by Lee and co-workers,[305] was synthesized and employed for free radical generation.[94,306,321] An overview of the synthetic procedure is found in Chapter 5, and full synthetic details have been detailed in a previous publication.[321]

6.3.3 Sample Preparation

Solutions of the underivatized peptides were prepared from a 1 mg/mL stock solution in water, which was then diluted in 49% methanol, 49% water, and 2% acetic acid (v/v) for a 50 μM solution. To derivatize the model peptides, approximately 1 mg of a peptide was dissolved in 1 mL of a 50/50 (v/v) mixture of acetonitrile/water, vortexed for 3 min, sonicated for 15 min, and centrifuged at 4500 rpm for 5 min. A reaction mixture of 50 μL of peptide supernatant, 10 μL of a 10 μg/μL solution of FRIPS reagent in acetonitrile in a 100 mM triethyl ammonium bicarbonate buffer (pH 8.5) was prepared. The reaction was allowed to proceed for 2 hr and then quenched by addition of 2 μL of formic acid. The

solvent was removed with use of a rotary evaporator, and the sample was resuspended in 10 µL of 0.1% trifluoroacetic acid and purified using a C_{18} ZipTip (Millipore, Billerica, MA) according to manufacturer protocol. The eluted sample was increased to a final volume of 500 µL in 49% methanol, 49% water, and 2% acetic acid (v/v).

6.3.4 Experimental Setup

The experimental setup consists of an electrospray ion source (ESI), the ROMIAC, and a Thermo LTQ-MS (Thermo Fisher, Waltham, MA). Full details of the experimental apparatus and calibration procedure can be found elsewhere in work by Mui and co-workers.[95] Nitrogen gas enters the ESI chamber perpendicular to the spray needle and conveys ions to the ROMIAC. Nitrogen is also utilized as the cross-flow gas through the ROMIAC, regulated with a proportioning solenoid valve and exhausted through a vacuum pump with the flow rate kept constant by a critical orifice at the inlet to the vacuum pump. All experiments were run at cross-flow gas rate of 34.3 L min^{-1} and a carrier gas flow rate of 1.70 L min^{-1}, resulting in a theoretical resolution (R_{nd}) of 20.2. Gas flow was controlled by a custom LabView interface utilizing a proportional-integral-differential (PID) algorithm with feedback from differential pressure transducers. Analytes were at atmospheric pressure for the entire journey from the ESI spray needle to the LTQ-MS inlet, the duration of which is estimated to be on the order of tens to hundreds of milliseconds.

Ion mobility spectra were obtained by stepping through a range of voltages and monitoring the LTQ-MS signal. The LTQ-MS was scanned from *m/z* 50 to 2000 and averaged over three microscans of 10 ms maximum duration. The instrument was operated with a capillary temperature of 50° C, a capillary voltage of 0 V, and a tube lens voltage of

88 V. For model peptide collision-induced dissociation (CID) experiments, the singly-protonated parent ion was isolated with an isolation width of 3 m/z (window of m/z in the trap during isolation prior to collisional activation) and a normalized collision energy of 10%. The experimental setup was calibrated using tetraalkylammonium halide salts as mobility standards for instrument calibration (IC) and also using biomolecules with known cross sections for mobility calibration (MC).

6.4 Results and Discussion

6.4.1 CID and FRIPS of Peptide Isomers

Two sets of peptide isomers, AARAAATAA/AATAAARAA and AARAAHAMA/AARAAMAHA, were analyzed in this study. To identify diagnostic product ions for each species, CID was performed on the singly-protonated ion of each of the peptides, as shown in Figure 6.1 with the product ions unique to each isomer highlighted. The CID spectra of untagged peptides are dominated by b- and y-type ions generated via proton-catalyzed dissociation of the peptide backbone,[247] whereas addition of the FRIPS reagent results in free-radical-initiated dissociation that is highly selective for specific amino acids in the peptide sequence.[304,311] As shown in Figure 6.2a, CID of peptides derivatized with the FRIPS reagent generates an acetyl radical at the N-terminus of the peptide by homolytic cleavage of the C–O bond, followed by hydrogen atom abstraction and dissociation. The product ions utilized to differentiate the model peptide isomers are formed according to the processes shown in Figure 6.2b-d. For threonine-containing peptides, the observed $[a_6+H]^{\bullet}$ and z_7 ions are generated by hydrogen atom abstraction from C_β of the threonine side chain, followed by N–C_α bond cleavage and

subsequent loss of isocyanic acid from the N-terminal product ion (Figure 6.2b). The z_7-H ion may further decompose to yield the y_6 ion. The c_6 ion is formed by a similar process in which hydrogen atom transfer to the N-terminal carbonyl oxygen occurs in concert with N–C_α bond cleavage (Figure 6.2c).[321] For isomeric peptides containing histidine, unique product ions are formed by abstraction of hydrogen from C_β of histidine followed by cleavage of the C_α–C bond (Figure 6.2d).[311]

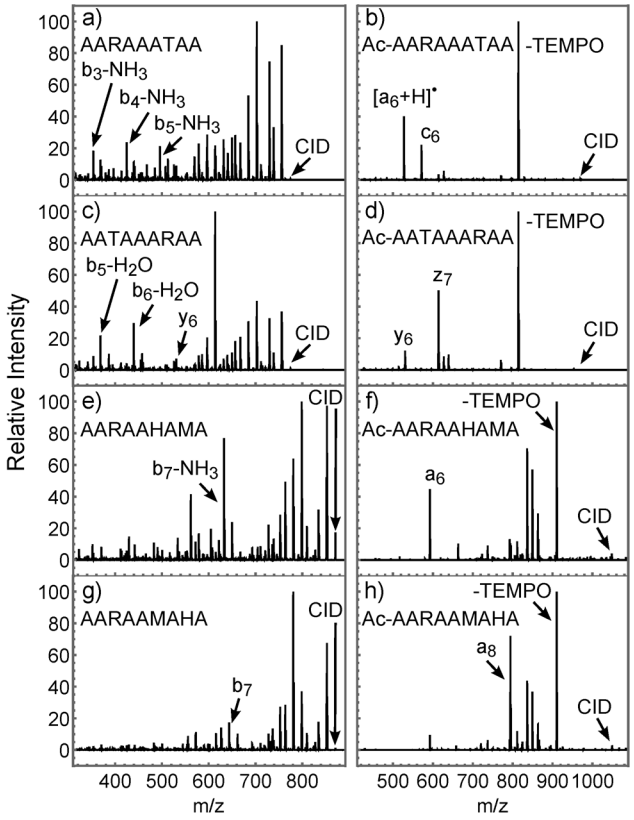

Figure 6.1. CID and FRIPS spectra of peptide isomers. Shown in a-d are the MS^2 spectra of AARAAATAA and AATAAARAA, both underivatized (a, c) and tagged with the FRIPS reagent (b, d). Shown in e-h are the MS^2 spectra of AARAAHAMA and AARAAMAHA, both underivatized (e, g) and tagged with the FRIPS reagent (f, h). Labeled product ions are specific to each isomer and are used for identification during ion mobility separation. Product ions in the FRIPS spectra are referenced to the *m/z* of the peptide with an acetyl radical at the N-terminus.

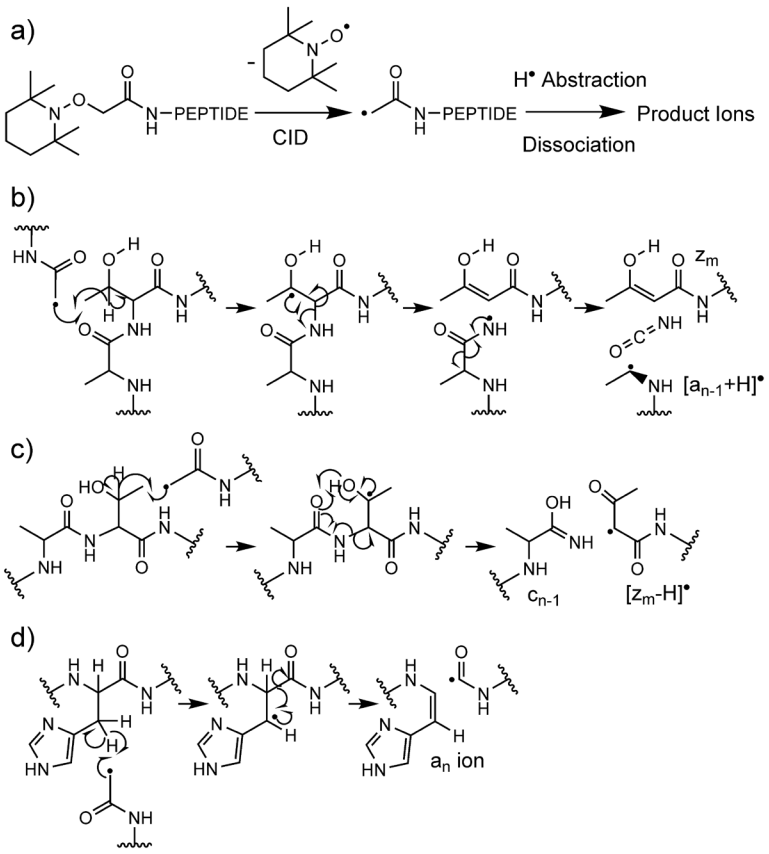

Figure 6.2. Free radical dissociation processes in peptides derivatized with the FRIPS reagent. The FRIPS methodology employed here is shown schematically in (a). The TEMPO-based FRIPS reagent is coupled to the N-terminus of the peptide, and subsequent collisional activation leads to loss of the TEMPO moiety, generating an acetyl radical. This acetyl radical then abstracts a hydrogen atom from diverse sites along the peptide, leading to dissociation of the backbone or neutral loss of amino acid side chains. Unique product ions are proposed to occur at threonine residues via the mechanisms shown in (b) and (c), resulting in (b) $[a_6+H]^•$ and z_7 ion and (c) c_6 ion formation. Backbone dissociation at histidine residues occurs by the mechanism illustrated in (d), leading to a_6 and a_8 ion generation.

6.4.2 Separation of Peptide Isomers

Following the identification of diagnostic product ions for each isomer, a mixture of isomeric peptides was separated by the ROMIAC and sequenced by CID within the ion trap, both with and without attachment of the FRIPS reagent. For untagged AARAAATAA

and AATAAARAA, the peak signals from the three diagnostic product ions of each isomer (Figure 6.1a,c) appear at the same voltage (considering errors), precluding resolution of the isomers (Figure 6.3a,b). However, the addition of the FRIPS reagent enhances peptide isomer separation by ~7 V or ~14 $Å^2$ (Figure 6.3c,d), allowing for isomer identification by CID. A similar but less dramatic separation enhancement occurs for the AARAAHAMA and AARAAMAHA isomers; unique product ions from the untagged peptides (Figure 6.1e,g) are separated by ~1 V (Figure 6e,f), but tagging of these peptides with the FRIPS reagent increases separation in the ion mobility spectrum by ~3 V or ~4 $Å^2$ (Figure 6.3g,h). The difference in separation enhancement between the two pairs of model peptides upon addition of the FRIPS reagent is not surprising, since the structural similarity is much greater between AARAAHAMA and AARAAMAHA than between AARAAATAAA and AATAAARAA. In the former pair of isomers, the location of the likely protonation site (Arg) is not altered, and the His and Met residues change position only slightly. It is evident in both cases, however, that the addition of the FRIPS reagent to the N-terminus improves separation. The reason for this improvement is not entirely clear but is likely due to disruption of interactions between the altered N-terminus and other sites on the peptide backbone. In addition, the radical-driven dissociation of the TEMPO-tagged peptides generates a more distinct spectrum than CID, although the overall sequence coverage is diminished.

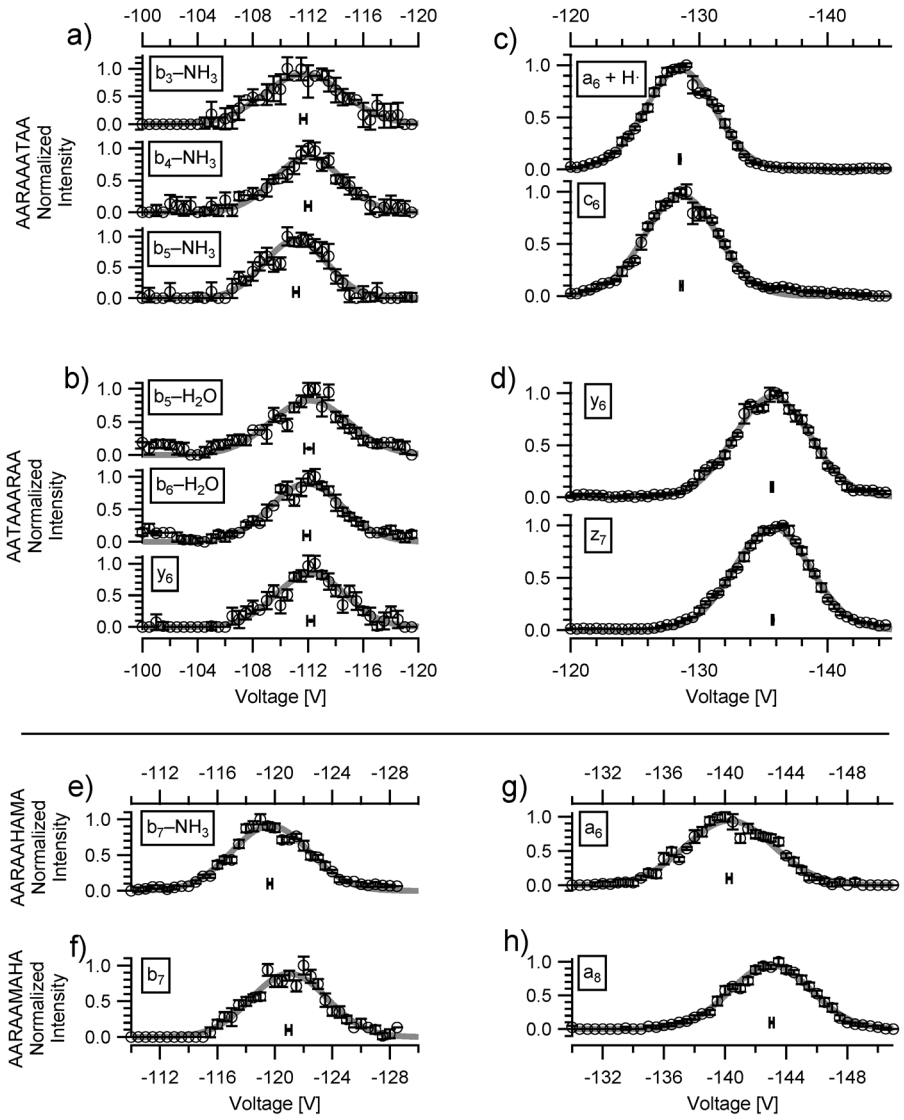

Figure 6.3. Separation of peptide isomers derivatized with the FRIPS reagent utilizing the ROMIAC. Shown are mass-resolved, normalized product ion signals as a function of applied voltage. Data point error bars indicate 1 standard deviation of the normalized signal. Gray line: Gaussian-fitted function to the signal; dot marker: centroid of fit, with 95% confidence interval error bars. (a) Non-TEMPO-tagged AARAAATAA CID fragments. (b) Non-TEMPO-tagged AATAAARAA CID fragments. (c) TEMPO-tagged AARAAATAA CID fragments. (d) TEMPO-tagged AATAAARAA CID fragments. (e) Non-TEMPO-tagged AARAAHAMA CID fragment. (f) Non-TEMPO-tagged AARAAMAHA CID fragment. (g) TEMPO-tagged AARAAHAMA CID fragment. (h) TEMPO-tagged AARAAMAHA CID fragment.

6.5 Conclusions

This study demonstrates the ability of IM-MS experiments using a ROMIAC to effectively separate peptides with similar sequences. Specifically, model peptide isomer separation was successfully conducted with untagged AARAAHAMA/AARAAMAHA using ROMIAC-IMS, and separation was demonstrably enhanced by derivatization with the FRIPS reagent, allowing the separation of AARAAATAA/AATAAARAA isomers. Although the modest resolution of ~20 achieved in these experiments was readily able to separate peptide isomers, greater resolution may be achieved in future work by increasing the cross flow rate.

The ROMIAC is desirable for further IMS applications, as it suffers fewer diffusional losses of ions than the conventional DMA and readily achieves resolution sufficient for separation of peptides. Additionally, the ROMIAC provides continuous transmission of ions, allowing for targeted monitoring of specific analytes. The ROMIAC can be easily interfaced to any mass spectrometer with an atmospheric pressure inlet. Improvements to the ROMIAC-MS interface should greatly enhance ion transfer efficiency and hence sensitivity. Given the ability to identify isomeric peptides shown in this study, the ROMIAC may be utilized in future experiments as a prefilter to reject abundant ion components and enhance the MS capability for detection of low abundance ions. For example, it could be used for real-time investigations of low abundance human serum proteins, especially those known to be markers for disease, by eliminating abundant background proteins and thereby improving the dynamic range of MS to detect the desired proteins.

Appendix A

Design of Enclosure for FIDI-MS Experiments in a Regulated Atmosphere

The FIDI-MS source utilized in experiments in Chapter 3 is designed to allow for control of the ambient conditions in which suspended droplet chemistry is studied. The device consists of four main parts: an enclosure, a back plate, and two viewport plates, all machined by eMachineShop (Mahwah, NJ). The assembled source is shown in Figure A.1a. The interface with the mounts of the LTQ mass spectrometer is based upon a design for a custom electrospray stage by Priska D. von Haller at the University of Washington Proteomics Resource. The device seals to the front of the mass spectrometer by an O-ring present on the atmospheric pressure interface, normally utilized to seal commercially available atmospheric pressure ionization sources. Once mounted, the entire device can reach a vacuum pressure of approximately 10 Torr using only the draw of gas through the atmospheric pressure interface of the LTQ.

Shown in Figure A.1b is an image of the main enclosure mounted to the inlet of the LTQ mass spectrometer. The right side of the enclosure is equipped with two 1” baseplate apertures, which allow for the mounting of various feedthrough interfaces. For the experiments in Chapter 3, the apertures are mounted with 1/8 in. outer diameter (OD) feedthroughs (FCH-012S, Kurt J. Lesker, Jefferson, Hills, PA) to introduce sample to the FIDI capillary and collect waste droplets from the enclosure. The backing plate of the enclosure is also equipped with three 1” baseplate apertures and is sealed to the main enclosure by a Viton O-ring (McMaster-Carr, Santa Fe Springs, CA). The backing plate

holds a gas feedthrough (LFT421TETE, Kurt J. Lesker) to control the ambient conditions in the chamber and a high voltage feedthrough (A0507-1-QF, MPF Products, Gray Court, SC) to apply an electric potential to the FIDI apparatus.

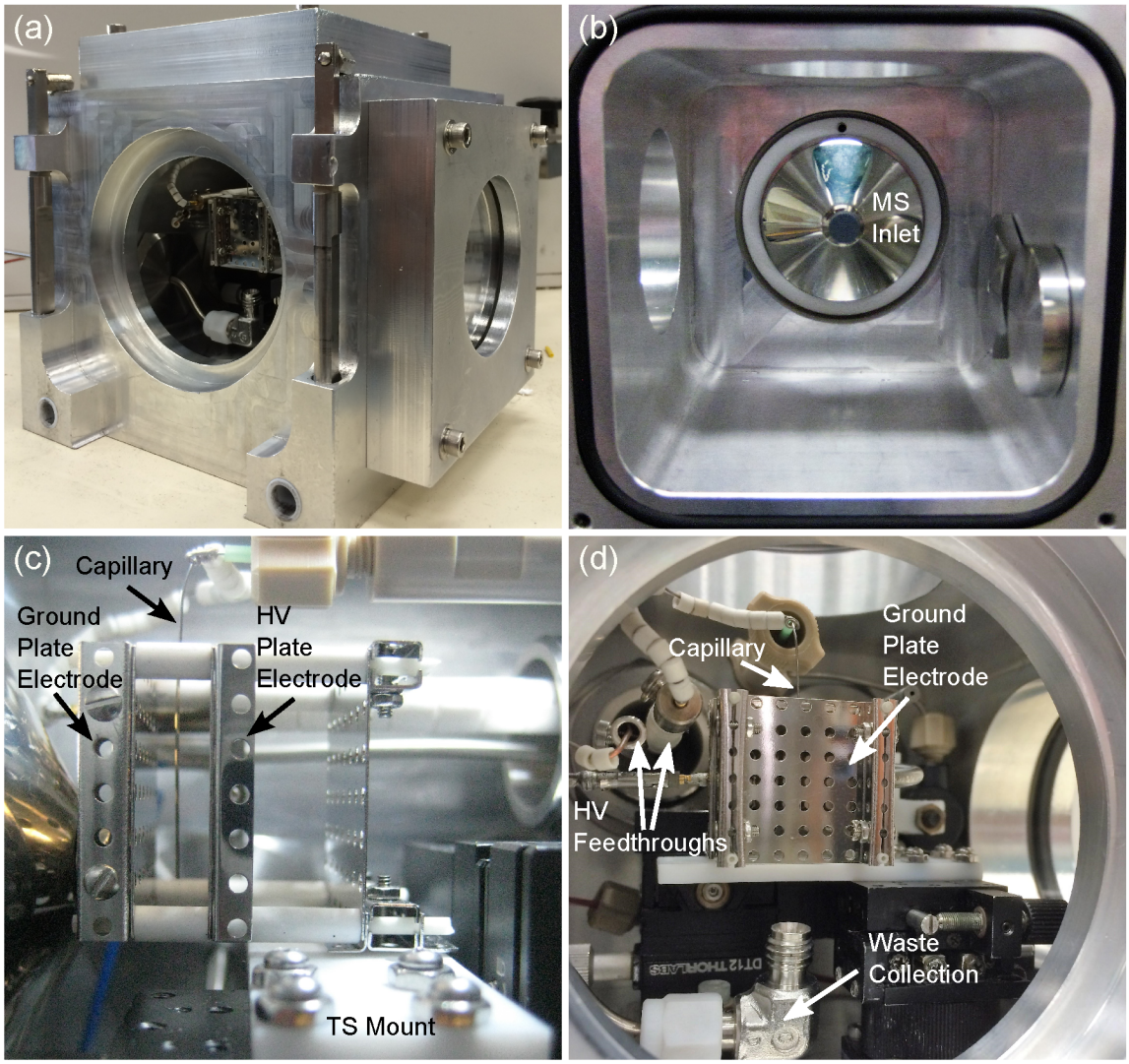

Figure A.1. Enclosure for FIDI experiments to regulate ambient conditions. Shown in (a) is the assembled source, and the main enclosure mounted to the mass spectrometer inlet is shown in (b). Shown in (c) and (d) are two views of the FIDI apparatus mounted within the enclosure.

The enclosure is also equipped with glass viewport mounts on the top and left side of the device to allow for visual monitoring and to initiate photochemistry. The viewport mounts are based on a design detailed by Abbott and Scace in which the glass window is sealed on each side by compression of an O-ring, avoiding direct glass-metal contact.[354] Glass windows of 80 mm diameter and 12 mm thickness were obtained from OptoSigma (Santa Ana, CA), with the top window fabricated from BK7 glass and the side window fabricated from fused silica to allow for efficient UV transmission.

Within the enclosure, the FIDI apparatus is based upon a design described previously by Grimm and co-workers.[83] The source region is fabricated from eV parts (Kimball Physics, Wilton, NH), with the high voltage and ground plates (SS-PL-B7x7) mounted on ceramic rods (Al2O3-TU-B-2000) secured to a custom PTFE mount via a bracket (SS-BR-B2x7). The plates are held in position by a combination of screw clamps (SS-SC-B7) and ceramic spacers (AL2O3-TU-C-250). The mount is affixed to a translation stage (TS) for alignment with the inlet of the mass spectrometer. The stainless steel (SS) capillary (28 gauge, McMaster-Carr) is also connected to a translation stage by 1/16 in. OD stainless steel tubing (0.005 in. ID, Sigma-Aldrich, St. Louis, MO) for alignment between the two plates.

Appendix B

Parameters for Modelling of Uptake Coupled with Reaction and Diffusion in Aqueous Droplets

Table B.1. Diffusion Constants for Species in Reaction-Diffusion Model

Molecule	D x 10^5, $cm^2\ s^{-1}$	Reference
CO_2	1.9	355
HCO_3^-	1.0	355
CO_3^{2-}	0.8	355
H_2CO_3	1.0	Assumed equivalent to HCO_3^-
NH_3	1.9	356
NH_4^+	1.9	357
H^+	8.8	358
OH^-	5.0	358

Table B.2. Reaction Kinetic Parameters for Reaction-Diffusion Model

Reaction #	Reaction	Rate	Units	Reference
3f	$NH_3 + H_2O \rightarrow NH_4^+ + OH^-$	5.0×10^5	s^{-1}	121
3r	$NH_4^+ + OH^- \rightarrow NH_3 + H_2O$	3.4×10^{10}	$M^{-1}\ s^{-1}$	121
4f	$NH_3 + H_3O^+ \rightarrow NH_4^+ + H_2O$	4.3×10^{10}	$M^{-1}\ s^{-1}$	120,121
4r	$NH_4^+ + H_2O \rightarrow NH_3 + H_3O^+$	24.6	s^{-1}	120,121
5f	$2\ H_2O \rightarrow H_3O^+ + OH^-$	1.4×10^{-3}	$M^{-1}\ s^{-1}$	121
5r	$H_3O^+ + OH^- \rightarrow 2\ H_2O$	1.4×10^{11}	$M^{-1}\ s^{-1}$	121
6f	$CO_2 + H_2O \rightarrow H_2CO_3$	0.04	s^{-1}	122
6r	$H_2CO_3 \rightarrow CO_2 + H_2O$	18	s^{-1}	122
7f	$CO_2 + OH^- \rightarrow HCO_3^-$	8.5×10^3	$M^{-1}\ s^{-1}$	359, 360
7r	$HCO_3^- \rightarrow CO_2 + OH^-$	2×10^4	s^{-1}	360
8f	$H_2CO_3 + H_2O \rightarrow HCO_3^- + H_3O^+$	1.0×10^7	s^{-1}	121
8r	$HCO_3^- + H_3O^+ \rightarrow H_2CO_3 + H_2O$	5.0×10^{10}	$M^{-1}\ s^{-1}$	121
9f	$HCO_3^- + OH^- \rightarrow CO_2 + H_2O$	6×10^9	$M^{-1}\ s^{-1}$	121
9r	$CO_2 + H_2O \rightarrow HCO_3^- + OH^-$	1.3×10^6	s^{-1}	121

Table B.3. Henry's Law Constants and Mass Accommodation Coefficients for Reaction-Diffusion Model

Constant	Value	Units	Reference
H_{CO2}	3.3×10^{-4}	mol Pa m^{-3}	361
H_{NH3}	3.1×10^{-1}	mol Pa m^{-3}	103
α_{CO2}	0.0001	Unitless	20
α_{NH3}	0.08	Unitless	103

Table B.4. Initial Conditions for Reaction-Diffusion Model

Condition	Value	Units
T	295	K
$[CO_2]$ (g)	40.5	Pa
$[CO_2]$ (aq)	1.35×10^{-5}	M
$[H_2CO_3]$	3.00×10^{-7}	M
$[HCO_3^-]$	2.45×10^{-6}	M
$[CO_3^{2-}]$	4.69×10^{-11}	M
$[H_3O^+]$	2.45×10^{-6}	M
$[OH^-]$	4.08×10^{-9}	M

BIBLIOGRAPHY

(1) Donaldson, D. J.; George, C. *Environ. Sci. Technol.* **2012**, *46*, 10385-10389.
(2) Shiraiwa, M.; Pfrang, C.; Koop, T.; Pöschl, U. *Atmos. Chem. Phys.* **2012**, *12*, 2777-2794.
(3) Kolb, C. E.; Cox, R. A.; Abbatt, J. P. D.; Ammann, M.; Davis, E. J.; Donaldson, D. J.; Garrett, B. C.; George, C.; Griffiths, P. T.; Hanson, D. R.; Kulmala, M.; McFiggans, G.; Pöschl, U.; Riipinen, I.; Rossi, M. J.; Rudich, Y.; Wagner, P. E.; Winkler, P. M.; Worsnop, D. R.; O' Dowd, C. D. *Atmos. Chem. Phys.* **2010**, *10*, 10561-10605.
(4) Blando, J. D.; Turpin, B. J. *Atmos. Environ.* **2000**, *34*, 1623-1632.
(5) Ervens, B.; Turpin, B. J.; Weber, R. J. *Atmos. Chem. Phys.* **2011**, *11*, 11069-11102.
(6) Herrmann, H.; Schaefer, T.; Tilgner, A.; Styler, S. A.; Weller, C.; Teich, M.; Otto, T. *Chem. Rev.* **2015**, *115*, 4259-4334.
(7) Kim, H. I.; Kim, H.; Shin, Y. S.; Beegle, L. W.; Jang, S. S.; Neidholdt, E. L.; Goddard, W. A.; Heath, J. R.; Kanik, I.; Beauchamp, J. L. *J. Am. Chem. Soc.* **2010**, *132*, 2254-2263.
(8) Ma, G.; Allen, H. C. *Photochem. Photobiol.* **2006**, *82*, 1517-1529.
(9) Garrett, B. C.; Schenter, G. K.; Morita, A. *Chem. Rev.* **2006**, *106*, 1355-1374.
(10) Bhattacharyya, I.; Maze, J. T.; Ewing, G. E.; Jarrold, M. F. *J. Phys. Chem. A* **2010**, *115*, 5723-5728.
(11) Jungwirth, P.; Tobias, D. J. *Chem. Rev.* **2006**, *106*, 1259-1281.
(12) Tobias, D. J.; Stern, A. C.; Baer, M. D.; Levin, Y.; Mundy, C. J. *Annu. Rev. Phys. Chem.* **2013**, *64*, 339-359.
(13) Takahashi, M. *J. Phys. Chem. B* **2005**, *109*, 21858-21864.
(14) Du, Q.; Superfine, R.; Freysz, E.; Shen, Y. R. *Phys. Rev. Lett.* **1993**, *70*, 2313-2316.
(15) Knipping, E. M.; Lakin, M. J.; Foster, K. L.; Jungwirth, P.; Tobias, D. J.; Gerber, R. B.; Dabdub, D.; Finlayson-Pitts, B. J. *Science* **2000**, *288*, 301-306.
(16) Laskin, A.; Gaspar, D. J.; Wang, W.; Hunt, S. W.; Cowin, J. P.; Colson, S. D.; Finlayson-Pitts, B. J. *Science* **2003**, *301*, 340-344.
(17) George, I. J.; Abbatt, J. P. D. *Nat. Chem.* **2010**, *2*, 713-722.
(18) Ota, S. T.; Richmond, G. L. *J. Am. Chem. Soc.* **2011**, *133*, 7497-7508.
(19) Van Loon, L. L.; Allen, H. C. *J. Phys. Chem. A* **2008**, *112*, 7873-7880.
(20) Davidovits, P.; Kolb, C. E.; Williams, L. R.; Jayne, J. T.; Worsnop, D. R. *Chem. Rev.* **2011**, *111*, PR76-109.
(21) Mouchel-Vallon, C.; Bräuer, P.; Camredon, M.; Valorso, R.; Madronich, S.; Herrmann, H.; Aumont, B. *Atmos. Chem. Phys.* **2013**, *13*, 1023-1037.
(22) Vácha, R.; Slavíček, P.; Mucha, M.; Finlayson-Pitts, B. J.; Jungwirth, P. *J. Phys. Chem. A* **2004**, *108*, 11573-11579.
(23) Donaldson, D. J.; Vaida, V. *Chem. Rev.* **2006**, *106*, 1445-1461.
(24) Donaldson, D. J.; Valsaraj, K. T. *Environ. Sci. Technol.* **2010**, *44*, 865-873.
(25) Martins-Costa, M. T. C.; Anglada, J. M.; Francisco, J. S.; Ruiz-Lopez, M. F. *Angew. Chem., Int. Ed.* **2012**, *51*, 5413-5417.

(26) Waring, C.; King, K. L.; Bagot, P. A. J.; Costen, M. L.; McKendrick, K. G. *Phys. Chem. Chem. Phys.* **2011**, *13*, 8457-8469.
(27) Voss, L. F.; Bazerbashi, M. F.; Beekman, C. P.; Hadad, C. M.; Allen, H. C. *J. Geophys. Res.: Atmos.* **2007**, *112*, D06209.
(28) Finlayson-Pitts, B. J. *Phys. Chem. Chem. Phys.* **2009**, *11*.
(29) Saykally, R. J. *Nat. Chem.* **2013**, *5*, 82-84.
(30) Lambert, A. G.; Davies, P. B.; Neivandt, D. J. *Appl. Spectrosc. Rev.* **2005**, *40*, 103-145.
(31) Moad, A. J.; Simpson, G. J. *J. Phys. Chem. B* **2004**, *108*, 3548-3562.
(32) Jungwirth, P.; Tobias, D. J. *J. Phys. Chem. B* **2002**, *106*, 6361-6373.
(33) Skinner, J. L.; Pieniazek, P. A.; Gruenbaum, S. M. *Acc. Chem. Res.* **2011**, *45*, 93-100.
(34) Jungwirth, P.; Tobias, D. J. *J. Phys. Chem. B* **2001**, *105*, 10468-10472.
(35) Shen, Y. R.; Ostroverkhov, V. *Chem. Rev.* **2006**, *106*, 1140-1154.
(36) Nihonyanagi, S.; Mondal, J. A.; Yamaguchi, S.; Tahara, T. *Annu. Rev. Phys. Chem.* **2013**, *64*, 579-603.
(37) Jungwirth, P.; Winter, B. *Annu. Rev. Phys. Chem.* **2008**, *59*, 343-366.
(38) Geissler, P. L. *Annu. Rev. Phys. Chem.* **2013**, *64*, 317-337.
(39) Onorato, R. M.; Otten, D. E.; Saykally, R. J. *J. Phys. Chem. C* **2010**, *114*, 13746-13751.
(40) Baldelli, S.; Schnitzer, C.; Simonelli, D. *J. Phys. Chem. B* **2002**, *106*, 5313-5324.
(41) Jubb, A. M.; Hua, W.; Allen, H. C. *Acc. Chem. Res.* **2011**, *45*, 110-119.
(42) Richmond, G. L. *Chem. Rev.* **2002**, *102*, 2693-2724.
(43) Ji, N.; Ostroverkhov, V.; Chen, C.-Y.; Shen, Y.-R. *J. Am. Chem. Soc.* **2007**, *129*, 10056-10057.
(44) Brauner, J. W.; Flach, C. R.; Xu, Z.; Bi, X.; Lewis, R. N. A. H.; McElhaney, R. N.; Gericke, A.; Mendelsohn, R. *J. Phys. Chem. B* **2003**, *107*, 7202-7211.
(45) Mendelsohn, R.; Mao, G.; Flach, C. R. *Biochim. Biophys. Acta, Biomembr.* **2010**, *1798*, 788-800.
(46) Griffith, E. C.; Vaida, V. *Proc. Natl. Acad. Sci. U.S.A.* **2012**, *109*, 15697-15701.
(47) Mmereki, B. T.; Donaldson, D. J.; Gilman, J. B.; Eliason, T. L.; Vaida, V. *Atmos. Environ.* **2004**, *38*, 6091-6103.
(48) Clifford, D.; Donaldson, D. J. *J. Phys. Chem. A* **2007**, *111*, 9809-9814.
(49) Clifford, D.; Bartels-Rausch, T.; Donaldson, D. J. *Phys. Chem. Chem. Phys.* **2007**, *9*, 1362-1369.
(50) Chen, X.; Huang, Z.; Hua, W.; Castada, H.; Allen, H. C. *Langmuir* **2010**, *26*, 18902-18908.
(51) Griffith, E. C.; Perkins, R. J.; Telesford, D.-M.; Adams, E. M.; Cwiklik, L.; Allen, H. C.; Roeselová, M.; Vaida, V. *J. Phys. Chem. B* **2015**, *119*, 9038-9048.
(52) Griffith, E. C.; Adams, E. M.; Allen, H. C.; Vaida, V. *J. Phys. Chem. B* **2012**, *116*, 7849-7857.
(53) Peikert, M.; Chen, X.; Chi, L.; Brezesinski, G.; Janich, S.; Würthwein, E.-U.; Schäfer, H. J. *Langmuir* **2014**, *30*, 5780-5789.
(54) Hoenig, D.; Moebius, D. *J. Phys. Chem.* **1991**, *95*, 4590-4592.
(55) Weber, R.; Winter, B.; Schmidt, P. M.; Widdra, W.; Hertel, I. V.; Dittmar, M.; Faubel, M. *J. Phys. Chem. B* **2004**, *108*, 4729-4736.

(56) Winter, B.; Weber, R.; Hertel, I. V.; Faubel, M.; Vrbka, L.; Jungwirth, P. *Chem. Phys. Lett.* **2005**, *410*, 222-227.
(57) Buchner, F.; Lubcke, A.; Heine, N.; Schultz, T. *Rev. Sci. Instrum.* **2010**, *81*, 113107-113106.
(58) Ghosal, S.; Brown, M. A.; Bluhm, H.; Krisch, M. J.; Salmeron, M.; Jungwirth, P.; Hemminger, J. C. *J. Phys. Chem. A* **2008**, *112*, 12378-12384.
(59) Thomas, R. K. *Annu. Rev. Phys. Chem.* **2004**, *55*, 391-426.
(60) Pignat, J.; Daillant, J.; Leiserowitz, L.; Perrot, F. *J. Phys. Chem. B* **2006**, *110*, 22178-22184.
(61) Strzalka, J.; Chen, X.; Moser, C. C.; Dutton, P. L.; Ocko, B. M.; Blasie, J. K. *Langmuir* **2000**, *16*, 10404-10418.
(62) Kisko, K.; Szilvay, G. R.; Vuorimaa, E.; Lemmetyinen, H.; Linder, M. B.; Torkkeli, M.; Serimaa, R. *Langmuir* **2008**, *25*, 1612-1619.
(63) Nathanson, G. M.; Davidovits, P.; Worsnop, D. R.; Kolb, C. E. *J. Phys. Chem.* **1996**, *100*, 13007-13020.
(64) Jayne, J. T.; Davidovits, P.; Worsnop, D. R.; Zahniser, M. S.; Kolb, C. E. *J. Phys. Chem.* **1990**, *94*, 6041-6048.
(65) Tarbuck, T. L.; Richmond, G. L. *J. Am. Chem. Soc.* **2005**, *127*, 16806-16807.
(66) Tarbuck, T. L.; Richmond, G. L. *J. Am. Chem. Soc.* **2006**, *128*, 3256-3267.
(67) Baer, M.; Mundy, C. J.; Chang, T.-M.; Tao, F.-M.; Dang, L. X. *J. Phys. Chem. B* **2010**, *114*, 7245-7249.
(68) Hearn, J. D.; Smith, G. D. *Anal. Chem.* **2004**, *76*, 2820-2826.
(69) Zhao, Z.; Husainy, S.; Smith, G. D. *J. Phys. Chem. A* **2011**, *115*, 12161-12172.
(70) Zhao, Z.; Husainy, S.; Stoudemayer, C. T.; Smith, G. D. *Phys. Chem. Chem. Phys.* **2011**, *13*, 17809-17817.
(71) Ault, A. P.; Zhao, D.; Ebben, C. J.; Tauber, M. J.; Geiger, F. M.; Prather, K. A.; Grassian, V. H. *Phys. Chem. Chem. Phys.* **2013**, *15*, 6206-6214.
(72) Hirabayashi, A.; Sakairi, M.; Koizumi, H. *Anal. Chem.* **1995**, *67*, 2878-2882.
(73) Enami, S.; Hoffmann, M. R.; Colussi, A. J. *J. Phys. Chem. A* **2009**, *113*, 7002-7010.
(74) Enami, S.; Vecitis, C. D.; Cheng, J.; Hoffmann, M. R.; Colussi, A. J. *J. Phys. Chem. A* **2007**, *111*, 13032-13037.
(75) Enami, S.; Hoffmann, M. R.; Colussi, A. J. *Proc. Natl. Acad. Sci. U.S.A.* **2008**, *105*, 7365-7369.
(76) Hayase, S.; Yabushita, A.; Kawasaki, M.; Enami, S.; Hoffmann, M. R.; Colussi, A. J. *J. Phys. Chem. A* **2011**, *115*, 4935-4940.
(77) Kinugawa, T.; Enami, S.; Yabushita, A.; Kawasaki, M.; Hoffmann, M. R.; Colussi, A. J. *Phys. Chem. Chem. Phys.* **2011**, *13*, 5144-5149.
(78) Enami, S.; Vecitis, C. D.; Cheng, J.; Hoffmann, M. R.; Colussi, A. J. *J. Phys. Chem. A* **2007**, *111*, 8749-8752.
(79) Jorabchi, K.; Smith, L. M. *Anal. Chem.* **2009**, *81*, 9682-9688.
(80) Jorabchi, K.; Westphall, M. S.; Smith, L. M. *J. Am. Soc. Mass Spectrom.* **2008**, *19*, 833-840.
(81) Westphall, M. S.; Jorabchi, K.; Smith, L. M. *Anal. Chem.* **2008**, *80*, 5847-5853.
(82) Stindt, A.; Albrecht, M.; Panne, U.; Riedel, J. *Anal Bioanal Chem* **2013**, *405*, 7005-7010.

(83) Grimm, R. L.; Hodyss, R.; Beauchamp, J. L. *Anal. Chem.* **2006**, *78*, 3800-3806.
(84) Grimm, R. L.; Beauchamp, J. L. *J. Phys. Chem. B* **2003**, *107*, 14161-14163.
(85) Grimm, R. L.; Beauchamp, J. L. *J. Phys. Chem. B* **2005**, *109*, 8244-8250.
(86) Kim, H. I.; Kim, H.; Shin, Y. S.; Beegle, L. W.; Goddard, W. A.; Heath, J. R.; Kanik, I.; Beauchamp, J. L. *J. Phys. Chem. B* **2010**, *114*, 9496-9503.
(87) Ko, J.; Choi, S.; Rhee, Y.; Beauchamp, J.; Kim, H. *J. Am. Soc. Mass Spectrom.* **2012**, *23*, 141-152.
(88) Kharlamova, A.; Prentice, B. M.; Huang, T.-Y.; McLuckey, S. A. *Anal. Chem.* **2010**, *82*, 7422-7429.
(89) Kharlamova, A.; DeMuth, J. C.; McLuckey, S. A. *J. Am. Soc. Mass Spectrom.* **2011**, *23*, 88-101.
(90) Harris, E.; Sinha, B.; van Pinxteren, D.; Tilgner, A.; Fomba, K. W.; Schneider, J.; Roth, A.; Gnauk, T.; Fahlbusch, B.; Mertes, S.; Lee, T.; Collett, J.; Foley, S.; Borrmann, S.; Hoppe, P.; Herrmann, H. *Science* **2013**, *340*, 727-730.
(91) Nguyen, T. B.; Coggon, M. M.; Flagan, R. C.; Seinfeld, J. H. *Environ. Sci. Technol.* **2013**, *47*, 4307-4316.
(92) Zuo, Y.; Hoigne, J. *Environ. Sci. Technol.* **1992**, *26*, 1014-1022.
(93) Sorooshian, A.; Wang, Z.; Coggon, M. M.; Jonsson, H. H.; Ervens, B. *Environ. Sci. Technol.* **2013**, *47*, 7747-7756.
(94) Sohn, C. H.; Gao, J.; Thomas, D. A.; Kim, T.-Y.; Goddard III, W. A.; Beauchamp, J. L. *Chem. Sci.* **2015**, *6*, 4550-4560.
(95) Mui, W.; Thomas, D. A.; Downard, A. J.; Beauchamp, J. L.; Seinfeld, J. H.; Flagan, R. C. *Anal. Chem.* **2013**, *85*, 6319-6326.
(96) Buch, V.; Milet, A.; Vácha, R.; Jungwirth, P.; Devlin, J. P. *Proc. Natl. Acad. Sci. U.S.A.* **2007**, *104*, 7342-7347.
(97) Enami, S.; Stewart, L. A.; Hoffmann, M. R.; Colussi, A. n. J. *J. Phys. Chem. Lett.* **2010**, *1*, 3488-3493.
(98) Beattie, J. K.; Djerdjev, A. M.; Warr, G. G. *Faraday Discuss.* **2009**, *141*.
(99) Ardura, D.; Donaldson, D. J. *Phys. Chem. Chem. Phys.* **2009**, *11*, 857-863.
(100) Simonelli, D.; Baldelli, S.; Shultz, M. J. *Chem. Phys. Lett.* **1998**, *298*, 400-404.
(101) Simonelli, D.; Shultz, M. J. *J. Chem. Phys.* **2000**, *112*, 6804-6816.
(102) Donaldson, D. J. *J. Phys. Chem. A* **1999**, *103*, 62-70.
(103) Shi, Q.; Davidovits, P.; Jayne, J. T.; Worsnop, D. R.; Kolb, C. E. *J. Phys. Chem. A* **1999**, *103*, 8812-8823.
(104) Mozgawa, K.; Mennucci, B.; Frediani, L. *J. Phys. Chem. C* **2014**, *118*, 4715-4725.
(105) Fu, C.-F.; Tian, S. X. *J. Phys. Chem. C* **2013**, *117*, 13011-13020.
(106) Carignano, M. A.; Jacob, M. M.; Avila, E. E. *J. Phys. Chem. A* **2008**, *112*, 3676-3679.
(107) Dang, L. X.; Garrett, B. C. *Chem. Phys. Lett.* **2004**, *385*, 309-313.
(108) Takenaka, N.; Koyano, Y.; Nagaoka, M. *Chem. Phys. Lett.* **2010**, *485*, 119-123.
(109) Chakraborty, D.; Chandra, A. *J. Chem. Phys.* **2011**, *135*, -.
(110) Paul, S.; Chandra, A. *J. Chem. Phys.* **2005**, *123*, -.
(111) Kebarle, P.; Verkerk, U. H. *Mass Spec. Rev.* **2009**, *28*, 898-917.
(112) Takats, Z.; Nanita, S. C.; Cooks, R. G.; Schlosser, G.; Vekey, K. *Anal. Chem.* **2003**, *75*, 1514-1523.

(113) Liu, C.; Shang, J.; Zachara, J. M. *Water Resour. Res.* **2011**, *47*, W12514.
(114) Greenberg, M. D. *Advanced Engineering Mathematics*, 2nd ed.; Prentice Hall: Upper Saddle River, NJ, 1998.
(115) Miller, D. G. *J. Phys. Chem.* **1967**, *71*, 3588-3592.
(116) Bard, A. J.; Faulkner, L. R. *Electrochemical Methods: Fundamentals and Applications*, 2nd ed.; John Wiley: New York, 2000.
(117) Crank, J. *The Mathematics of Diffusion*, 2nd ed.; Oxford University Press: London, 1975.
(118) Lundberg, D.; Holmberg, K. *J. Surfactants Deterg.* **2004**, *7*, 239-246.
(119) Kumar, N.; Kishore, N. *J. Chem. Phys.* **2013**, *139*, 115104.
(120) Emerson, M. T.; Grunwald, E.; Kromhout, R. A. *J. Chem. Phys.* **1960**, *33*, 547-555.
(121) Eigen, M. *Angew. Chem., Int. Ed.* **1964**, *3*, 1-19.
(122) Stumm, W.; Morgan, J. J. *Aquatic Chemistry: Chemical Equilibria and Rates in Natural Waters*, 3rd ed.; John Wiley & Sons, Inc.: New York, 1996.
(123) Swartz, E.; Shi, Q.; Davidovits, P.; Jayne, J. T.; Worsnop, D. R.; Kolb, C. E. *J. Phys. Chem. A* **1999**, *103*, 8824-8833.
(124) Lim, Y. B.; Tan, Y.; Perri, M. J.; Seitzinger, S. P.; Turpin, B. J. *Atmos. Chem. Phys.* **2010**, *10*, 10521-10539.
(125) McNeill, V. F. *Environ. Sci. Technol.* **2015**, *49*, 1237-1244.
(126) Ervens, B.; Volkamer, R. *Atmos. Chem. Phys.* **2010**, *10*, 8219-8244.
(127) Jang, M.; Czoschke, N. M.; Lee, S.; Kamens, R. M. *Science* **2002**, *298*, 814-817.
(128) Vione, D.; Maurino, V.; Minero, C.; Pelizzetti, E.; Harrison, M. A. J.; Olariu, R.-I.; Arsene, C. *Chem. Soc. Rev.* **2006**, *35*, 441-453.
(129) George, C.; Ammann, M.; D'Anna, B.; Donaldson, D. J.; Nizkorodov, S. A. *Chem. Rev.* **2015**, *115*, 4218-4258.
(130) George, C.; D'Anna, B.; Herrmann, H.; Weller, C.; Vaida, V.; Donaldson, D. J.; Bartels-Rausch, T.; Ammann, M. In *Atmospheric and Aerosol Chemistry*, McNeill, F. V.; Ariya, A. P., Eds.; Springer Berlin Heidelberg: Berlin, Heidelberg, 2014, pp 1-53.
(131) Ervens, B.; Sorooshian, A.; Lim, Y. B.; Turpin, B. J. *J. Geophys. Res.: Atmos.* **2014**, *119*, 3997-4016.
(132) Carlton, A. G.; Turpin, B. J.; Altieri, K. E.; Seitzinger, S.; Reff, A.; Lim, H.-J.; Ervens, B. *Atmos. Environ.* **2007**, *41*, 7588-7602.
(133) Perri, M. J.; Seitzinger, S.; Turpin, B. J. *Atmos. Environ.* **2009**, *43*, 1487-1497.
(134) Perri, M. J.; Lim, Y. B.; Seitzinger, S. P.; Turpin, B. J. *Atmos. Environ.* **2010**, *44*, 2658-2664.
(135) Zhang, X.; Chen, Z. M.; Zhao, Y. *Atmos. Chem. Phys.* **2010**, *10*, 9551-9561.
(136) Aregahegn, K. Z.; Noziere, B.; George, C. *Faraday Discuss.* **2013**, *165*, 123-134.
(137) Griffith, E. C.; Carpenter, B. K.; Shoemaker, R. K.; Vaida, V. *Proc. Natl. Acad. Sci. U.S.A.* **2013**, *110*, 11714-11719.
(138) Fu, H.; Ciuraru, R.; Dupart, Y.; Passananti, M.; Tinel, L.; Rossignol, S.; Perrier, S.; Donaldson, D. J.; Chen, J.; George, C. *J. Am. Chem. Soc.* **2015**.
(139) Wang, Z.; Chen, C.; Ma, W.; Zhao, J. *J. Phys. Chem. Lett.* **2012**, *3*, 2044-2051.
(140) Guasco, T. L.; Cuadra-Rodriguez, L. A.; Pedler, B. E.; Ault, A. P.; Collins, D. B.; Zhao, D.; Kim, M. J.; Ruppel, M. J.; Wilson, S. C.; Pomeroy, R. S.; Grassian, V. H.; Azam, F.; Bertram, T. H.; Prather, K. A. *Environ. Sci. Technol.* **2014**, *48*, 1324-1333.

(141) Deguillaume, L.; Leriche, M.; Desboeufs, K.; Mailhot, G.; George, C.; Chaumerliac, N. *Chem. Rev.* **2005**, *105*, 3388-3431.
(142) Faust, B. C.; Hoigné, J. *Atmos. Environ., Part A* **1990**, *24*, 79-89.
(143) Chu, B.; Hao, J.; Takekawa, H.; Li, J.; Wang, K.; Jiang, J. *Atmos. Environ.* **2012**, *55*, 26-34.
(144) Xiao, D.; Guo, Y.; Lou, X.; Fang, C.; Wang, Z.; Liu, J. *Chemosphere* **2014**, *103*, 354-358.
(145) Wang, Z.; Xiao, D.; Liu, J. *RSC Adv.* **2014**, *4*, 44654-44658.
(146) Balmer, M. E.; Sulzberger, B. *Environ. Sci. Technol.* **1999**, *33*, 2418-2424.
(147) Weller, C.; Horn, S.; Herrmann, H. *J. Photochem. Photobiol., A* **2013**, *255*, 41-49.
(148) Weller, C.; Horn, S.; Herrmann, H. *J. Photochem. Photobiol., A* **2013**, *268*, 24-36.
(149) Sorooshian, A.; Ng, N. L.; Chan, A. W. H.; Feingold, G.; Flagan, R. C.; Seinfeld, J. H. *J. Geophys. Res.: Atmos.* **2007**, *112*, D13201.
(150) Benedict, K. B.; Lee, T.; Collett Jr, J. L. *Atmos. Environ.* **2012**, *46*, 104-114.
(151) Sorooshian, A.; Lu, M.-L.; Brechtel, F. J.; Jonsson, H.; Feingold, G.; Flagan, R. C.; Seinfeld, J. H. *Environ. Sci. Technol.* **2007**, *41*, 4647-4654.
(152) Parker, C. A. *Proc. R. Soc. London, Ser. A* **1953**, *220*, 104-116.
(153) Hatchard, C. G.; Parker, C. A. *Proc. R. Soc. London, Ser. A* **1956**, *235*, 518-536.
(154) Long, Y.; Charbouillot, T.; Brigante, M.; Mailhot, G.; Delort, A.-M.; Chaumerliac, N.; Deguillaume, L. *Atmos. Environ.* **2013**, *77*, 686-695.
(155) Vincze, L.; Papp, S. *J. Photochem.* **1987**, *36*, 289-296.
(156) Chen, J.; Zhang, H.; Tomov, I. V.; Rentzepis, P. M. *Inorg. Chem.* **2008**, *47*, 2024-2032.
(157) Pozdnyakov, I. P.; Kel, O. V.; Plyusnin, V. F.; Grivin, V. P.; Bazhin, N. M. *J. Phys. Chem. A* **2008**, *112*, 8316-8322.
(158) Chen, J.; Dvornikov, A. S.; Rentzepis, P. M. *J. Phys. Chem. A* **2009**, *113*, 8818-8819.
(159) Pozdnyakov, I. P.; Kel, O. V.; Plyusnin, V. F.; Grivin, V. P.; Bazhin, N. M. *J. Phys. Chem. A* **2009**, *113*, 8820-8822.
(160) Sedlak, D. L.; Hoigné, J. *Atmos. Environ., Part A* **1993**, *27*, 2173-2185.
(161) Zuo, Y.; Zhan, J. *Atmos. Environ.* **2005**, *39*, 27-37.
(162) Spaulding, R. S.; Schade, G. W.; Goldstein, A. H.; Charles, M. J. *J. Geophys. Res.: Atmos.* **2003**, *108*, 4247.
(163) Atkinson, R.; Arey, J. *Acc. Chem. Res.* **1998**, *31*, 574-583.
(164) Betterton, E. A.; Hoffmann, M. R. *Environ. Sci. Technol.* **1988**, *22*, 1415-1418.
(165) Neidholdt, E. L. *Novel pyroelectric and switched ferroelectric ion sources in mass spectrometry: implementation and applications*. Ph.D. Dissertation California Institute of Technology, Pasadena, CA, 2010.
(166) DeMore, W. B.; Sander, S. P.; Golden, D. B.; Hampson, R. F.; Kurylo, M. J.; Howard, C. J.; Ravishankara, A. R.; Kolb, C. E.; Molina, M. J. *Chemical Kinetics and Photochemical Data for Use in Stratospheric Modeling, Evaluation Number 12, JPL Pub. 97-4*; NASA Jet Propulsion Laboratory: Pasadena, CA, 1997.
(167) Ortiz-Montalvo, D. L.; Lim, Y. B.; Perri, M. J.; Seitzinger, S. P.; Turpin, B. J. *Aerosol Sci. Technol.* **2012**, *46*, 1002-1014.
(168) Iribarne, J. V.; Mason, B. J. *Trans. Faraday. Soc.* **1967**, *63*, 2234-2245.
(169) Knelman, F.; Dombrowski, N.; Newitt, D. M. *Nature* **1954**, *173*, 261-261.

(170) Mason, B. J. *Nature* **1954**, *174*, 470-471.
(171) Rossodivita, A.; Andreussi, P. *J. Geophys. Res.: Oceans* **1999**, *104*, 30059-30066.
(172) Spiel, D. E. *J. Geophys. Res.: Oceans* **1994**, *99*, 10289-10296.
(173) Lee, J. S.; Weon, B. M.; Park, S. J.; Je, J. H.; Fezzaa, K.; Lee, W.-K. *Nat. Commun.* **2011**, *2*, 367.
(174) Lugli, F.; Zerbetto, F. *Phys. Chem. Chem. Phys.* **2007**, *9*, 2447-2456.
(175) Duchemin, L.; Popinet, S.; Josserand, C.; Zaleski, S. *Phys. Fluids* **2002**, *14*, 3000-3008.
(176) Garcia-Briones, M. A.; Brodkey, R. S.; Chalmers, J. J. *Chem. Eng. Sci.* **1994**, *49*, 2301-2320.
(177) Sakai, M.; Tanaka, A.; Egawa, H.; Sugihara, G. *J. Colloid Interface Sci.* **1988**, *125*, 428-436.
(178) Ehrenhauser, F. S.; Avij, P.; Shu, X.; Dugas, V.; Woodson, I.; Liyana-Arachchi, T.; Zhang, Z.; Hung, F. R.; Valsaraj, K. T. *Environ. Sci.: Processes Impacts* **2014**, *16*, 65-73.
(179) Liyana-Arachchi, T. P.; Zhang, Z.; Ehrenhauser, F. S.; Avij, P.; Valsaraj, K. T.; Hung, F. R. *Environ. Sci.: Processes Impacts* **2014**, *16*, 53-64.
(180) Liger-Belair, G.; Polidori, G.; Jeandet, P. *Chem. Soc. Rev.* **2008**, *37*, 2490-2511.
(181) Quinn, P. K.; Bates, T. S.; Schulz, K. S.; Coffman, D. J.; Frossard, A. A.; Russell, L. M.; Keene, W. C.; Kieber, D. J. *Nat. Geosci.* **2014**, *7*, 228-232.
(182) Russell, L. M.; Hawkins, L. N.; Frossard, A. A.; Quinn, P. K.; Bates, T. S. *Proc. Natl. Acad. Sci. U. S. A.* **2010**, *107*, 6652-6657.
(183) Spiel, D. E. *J. Geophys. Res.: Oceans* **1998**, *103*, 24907-24918.
(184) Boultonstone, J. M.; Blake, J. R. *J. Fluid. Mech.* **1993**, *254*, 437-466.
(185) Blanchard, D. C. *J. Meteorol.* **1958**, *15*, 383-396.
(186) MacIntyre, F. *J. Geophys. Res.* **1972**, *77*, 5211-5228.
(187) Dulieu, B.; Aymami, J.; Hamaide, G. *Oceanol. Acta* **1984**, *7*, 175-179.
(188) Elrod, S. A.; Hadimioglu, B.; Khuri-Yakub, B. T.; Rawson, E. G.; Richley, E.; Quate, C. F.; Mansour, N. N.; Lundgren, T. S. *J. Appl. Phys.* **1989**, *65*, 3441-3447.
(189) Ellson, R.; Mutz, M.; Browning, B.; Lee, L.; Miller, M. F.; Papen, R. *JALA* **2003**, *8*, 29-34.
(190) Huang, D.; Kim, E. S. *J. Microelectromech. Syst.* **2001**, *10*, 442-449.
(191) Lee, C.-Y.; Yu, H.; Kim, E. S. *Appl. Phys. Lett.* **2006**, *89*, 223902.
(192) Yamada, K.; Shimizu, H. *J. Acoust. Soc. Jpn.* **1991**, *12*, 123-129.
(193) Wang, L.; Choe, Y.; Kim, E. S. In *2011 IEEE 24th International Conference on Micro Electro Mechanical Systems (MEMS)*: Cancun, Mexico, 2011, pp 1115-1118.
(194) Lee, C.-Y.; Pang, W.; Yu, H.; Kim, E. S. *Appl. Phys. Lett.* **2008**, *93*, 034104.
(195) Banic, C. M.; Iribarne, J. V. *J. Chem. Phys.* **1985**, *83*, 6432-6448.
(196) Keesee, R. G.; Castleman Jr, A. W. *Chem. Phys. Lett.* **1980**, *74*, 139-142.
(197) Hiraoka, K.; Mizuse, S.; Yamabe, S. *J. Phys. Chem.* **1988**, *92*, 3943-3952.
(198) Schlosser, G.; Takáts, Z.; Vékey, K. *J. Mass Spectrom.* **2003**, *38*, 1245-1251.
(199) Wang, G.; Cole, R. B. *Anal. Chim. Acta* **2000**, *406*, 53-65.
(200) Tang, L.; Kebarle, P. *Anal. Chem.* **1993**, *65*, 3654-3668.
(201) Smith, J. N.; Flagan, R. C.; Beauchamp, J. L. *J. Phys. Chem. A* **2002**, *106*, 9957-9967.

(202) Duft, D.; Lebius, H.; Huber, B. A.; Guet, C.; Leisner, T. *Phys. Rev. Lett.* **2002**, *89*, 084503.
(203) Duft, D.; Achtzehn, T.; Muller, R.; Huber, B. A.; Leisner, T. *Nature* **2003**, *421*, 128.
(204) Dodd, E. E. *J. Appl. Phys.* **1953**, *24*, 73-80.
(205) Zilch, L. W.; Maze, J. T.; Smith, J. W.; Ewing, G. E.; Jarrold, M. F. *J. Phys. Chem. A* **2008**, *112*, 13352-13363.
(206) Rayleigh, L. *Philos. Mag. (1798-1977)* **1882**, *14*, 184-186.
(207) Tison, S. A. *Vacuum* **1993**, *44*, 1171-1175.
(208) *CRC Handbook of Chemistry and Physics*, 95th ed.; CRC Press: Boca Raton, 2014.
(209) Gimelshein, N.; Gimelshein, S.; Lilly, T.; Moskovets, E. *J. Am. Soc. Mass Spectrom.* **2014**, *25*, 820-831.
(210) Xu, W.; Charipar, N.; Kirleis, M. A.; Xia, Y.; Ouyang, Z. *Anal. Chem.* **2010**, *82*, 6584-6592.
(211) Hinds, W. C. *Aerosol Technology: Properties, Behavior, and Measurement of Airborne Particles*, 2nd ed.; Wiley: New York, 1999.
(212) Grimm, R. L.; Beauchamp, J. L. *Anal. Chem.* **2002**, *74*, 6291-6297.
(213) Yaws, C. L. *Chemical Properties Handbook: Physical, Thermodynamic, Environmental, Transport, Safety, and Health Related Properties for Organic and Inorganic Chemicals*; McGraw-Hill: New York, 1999.
(214) Vargaftik, N. B.; Vinogradov, Y. K.; Yargin, V. S. *Handbook of Physical Propertieis of Liquids and Gases: Pure Substances and Mixtures*, 3rd ed.; Begell House, Inc.: New York, 1996.
(215) Kadoya, K.; Matsunaga, N.; Nagashima, A. *J. Phys. Chem. Ref. Data* **1985**, *14*, 947-970.
(216) Krzeczkowski, S. A. *Int. J. Multiphase Flow* **1980**, *6*, 227-239.
(217) Wierzba, A. *Exp. Fluids* **1990**, *9*, 59-64.
(218) Blakley, C. R.; Vestal, M. L. *Anal. Chem.* **1983**, *55*, 750-754.
(219) Blakley, C. R.; Carmody, J. J.; Vestal, M. L. *Anal. Chem.* **1980**, *52*, 1636-1641.
(220) Vestal, M. L. *Int. J. Mass Spectrom. Ion Phys.* **1983**, *46*, 193-196.
(221) Katta, V.; Rockwood, A. L.; Vestal, M. L. *Int. J. Mass Spectrom. Ion Processes* **1991**, *103*, 129-148.
(222) Pagnotti, V. S.; Inutan, E. D.; Marshall, D. D.; McEwen, C. N.; Trimpin, S. *Anal. Chem.* **2011**, *83*, 7591-7594.
(223) Pagnotti, V. S.; Chubatyi, N. D.; McEwen, C. N. *Anal. Chem.* **2011**, *83*, 3981-3985.
(224) Haddad, R.; Sparrapan, R.; Eberlin, M. N. *Rapid Commun. Mass Spectrom.* **2006**, *20*, 2901-2905.
(225) Chen, T.-Y.; Lin, J.-Y.; Chen, J.-Y.; Chen, Y.-C. *J. Am. Soc. Mass Spectrom.* **2010**, *21*, 1547-1553.
(226) Harris, G. A.; Galhena, A. S.; Fernández, F. M. *Anal. Chem.* **2011**, *83*, 4508-4538.
(227) Katrib, Y.; Martin, S. T.; Hung, H.-M.; Rudich, Y.; Zhang, H.; Slowik, J. G.; Davidovits, P.; Jayne, J. T.; Worsnop, D. R. *J. Phys. Chem. A* **2004**, *108*, 6686-6695.
(228) Ziemann, P. J. *Faraday Discuss.* **2005**, *130*, 469-490.
(229) Hung, H.-M.; Katrib, Y.; Martin, S. T. *J. Phys. Chem. A* **2005**, *109*, 4517-4530.
(230) Zahardis, J.; Petrucci, G. A. *Atmos. Chem. Phys.* **2007**, *7*, 1237-1274.
(231) Jubb, A. M.; Hua, W.; Allen, H. C. *Annu. Rev. Phys. Chem.* **2012**, *63*, 107-130.

(232) George, I. J.; Slowik, J.; Abbatt, J. P. D. *Geophys. Res. Lett.* **2008**, *35*, L13811.
(233) Roeselová, M.; Vieceli, J.; Dang, L. X.; Garrett, B. C.; Tobias, D. J. *J. Am. Chem. Soc.* **2004**, *126*, 16308-16309.
(234) Eckhardt, C. J.; Peachey, N. M.; Swanson, D. R.; Takacs, J. M.; Khan, M. A.; Gong, X.; Kim, J. H.; Wang, J.; Uphaus, R. A. *Nature* **1993**, *362*, 614-616.
(235) Viswanathan, R.; Zasadzinski, J. A.; Schwartz, D. K. *Nature* **1994**, *368*, 440-443.
(236) Hu, Y.; Lee, K. Y. C.; Israelachvili, J. *Langmuir* **2002**, *19*, 100-104.
(237) Bogdanov, B.; Smith, R. D. *Mass Spectrom. Rev.* **2005**, *24*, 168-200.
(238) Petrotchenko, E. V.; Borchers, C. H. *Mass Spectrom. Rev.* **2010**, *29*, 862-876.
(239) Lee, J.; Soper, S. A.; Murray, K. K. *J. Mass Spectrom.* **2009**, *44*, 579-593.
(240) Cooper, H. J.; Håkansson, K.; Marshall, A. G. *Mass Spectrom. Rev.* **2005**, *24*, 201-222.
(241) Shen, Y.; Zhao, R.; Berger, S. J.; Anderson, G. A.; Rodriguez, N.; Smith, R. D. *Anal. Chem.* **2002**, *74*, 4235-4249.
(242) Senko, M. W.; Speir, J. P.; McLafferty, F. W. *Anal. Chem.* **1994**, *66*, 2801-2808.
(243) Little, D. P.; Speir, J. P.; Senko, M. W.; O'Connor, P. B.; McLafferty, F. W. *Anal. Chem.* **1994**, *66*, 2809-2815.
(244) Kruger, N. A.; Zubarev, R. A.; Carpenter, B. K.; Kelleher, N. L.; Horn, D. M.; McLafferty, F. W. *Int. J. Mass Spectrom.* **1999**, *182-183*, 1-5.
(245) Håkansson, K.; Cooper, H. J.; Emmett, M. R.; Costello, C. E.; Marshall, A. G.; Nilsson, C. L. *Anal. Chem.* **2001**, *73*, 4530-4536.
(246) Shukla, A. K.; Futrell, J. H. *J. Mass Spectrom.* **2000**, *35*, 1069-1090.
(247) Paizs, B.; Suhai, S. *Mass Spectrom. Rev.* **2005**, *24*, 508-548.
(248) Tureček, F.; Julian, R. R. *Chem. Rev.* **2013**.
(249) Zubarev, R. A.; Kelleher, N. L.; McLafferty, F. W. *J. Am. Chem. Soc.* **1998**, *120*, 3265-3266.
(250) Kruger, N. A.; Zubarev, R. A.; Horn, D. M.; McLafferty, F. W. *Int. J. Mass Spectrom.* **1999**, *185-187*, 787-793.
(251) Syka, J. E. P.; Coon, J. J.; Schroeder, M. J.; Shabanowitz, J.; Hunt, D. F. *Proc. Natl. Acad. Sci. U.S.A.* **2004**, *101*, 9528-9533.
(252) Zubarev, R. A.; Kruger, N. A.; Fridriksson, E. K.; Lewis, M. A.; Horn, D. M.; Carpenter, B. K.; McLafferty, F. W. *J. Am. Chem. Soc.* **1999**, *121*, 2857-2862.
(253) Zubarev, R. A.; Horn, D. M.; Fridriksson, E. K.; Kelleher, N. L.; Kruger, N. A.; Lewis, M. A.; Carpenter, B. K.; McLafferty, F. W. *Anal. Chem.* **2000**, *72*, 563-573.
(254) Zubarev, R. A.; Haselmann, K. F.; Budnik, B.; Kjeldsen, F.; Jensen, F. *Eur. J. Mass Spectrom.* **2002**, *8*, 337-349.
(255) Simons, J. *Chem. Phys. Lett.* **2010**, *484*, 81-95.
(256) Iavarone, A. T.; Paech, K.; Williams, E. R. *Anal. Chem.* **2004**, *76*, 2231-2238.
(257) Chamot-Rooke, J.; Malosse, C.; Frison, G.; Tureček, F. *J. Am. Soc. Mass Spectrom.* **2007**, *18*, 2146-2161.
(258) Xia, Y.; Gunawardena, H. P.; Erickson, D. E.; McLuckey, S. A. *J. Am. Chem. Soc.* **2007**, *129*, 12232-12243.
(259) Anusiewicz, I.; Berdys-Kochanska, J.; Simons, J. *J. Phys. Chem. A* **2005**, *109*, 5801-5813.

(260) Anusiewicz, I.; Berdys-Kochanska, J.; Skurski, P.; Simons, J. *J. Phys. Chem. A* **2006**, *110*, 1261-1266.
(261) Sawicka, A.; Skurski, P.; Hudgins, R. R.; Simons, J. *J. Phys. Chem. B* **2003**, *107*, 13505-13511.
(262) Sawicka, A.; Berdys-Kochańska, J.; Skurski, P.; Simons, J. *Int. J. Quantum Chem.* **2005**, *102*, 838-846.
(263) Sobczyk, M.; Anusiewicz, I.; Berdys-Kochanska, J.; Sawicka, A.; Skurski, P.; Simons, J. *J. Phys. Chem. A* **2005**, *109*, 250-258.
(264) Skurski, P.; Sobczyk, M.; Jakowski, J.; Simons, J. *Int. J. Mass Spectrom.* **2007**, *265*, 197-212.
(265) Sobczyk, M.; Simons, J. *Int. J. Mass Spectrom.* **2006**, *253*, 274-280.
(266) Sobczyk, M.; Simons, J. *J. Phys. Chem. B* **2006**, *110*, 7519-7527.
(267) Sobczyk, M.; Neff, D.; Simons, J. *Int. J. Mass Spectrom.* **2008**, *269*, 149-164.
(268) Tureček, F. *J. Am. Chem. Soc.* **2003**, *125*, 5954-5963.
(269) Syrstad, E.; Tureček, F. *J. Am. Soc. Mass Spectrom.* **2005**, *16*, 208-224.
(270) Tureček, F.; Chen, X.; Hao, C. *J. Am. Chem. Soc.* **2008**, *130*, 8818-8833.
(271) Chen, X.; Tureček, F. *J. Am. Chem. Soc.* **2006**, *128*, 12520-12530.
(272) Syrstad, E. A.; Tureček, F. *J. Phys. Chem. A* **2001**, *105*, 11144-11155.
(273) Tureček, F.; Syrstad, E. A. *J. Am. Chem. Soc.* **2003**, *125*, 3353-3369.
(274) Syrstad, E. A.; Stephens, D. D.; Tureček, F. *J. Phys. Chem. A* **2003**, *107*, 115-126.
(275) Sohn, C. H.; Chung, C. K.; Yin, S.; Ramachandran, P.; Loo, J. A.; Beauchamp, J. L. *J. Am. Chem. Soc.* **2009**, *131*, 5444-5459.
(276) Frison, G.; van der Rest, G.; Tureček, F.; Besson, T.; Lemaire, J. l.; Maître, P.; Chamot-Rooke, J. *J. Am. Chem. Soc.* **2008**, *130*, 14916-14917.
(277) Tureček, F. *J. Mass Spectrom.* **2010**, *45*, 1280-1290.
(278) Bakhtiar, R.; Guan, Z. *Biochem. Biophys. Res. Commun.* **2005**, *334*, 1-8.
(279) Siuti, N.; Kelleher, N. L. *Nat. Meth.* **2007**, *4*, 817-821.
(280) Shi, S. D. H.; Hemling, M. E.; Carr, S. A.; Horn, D. M.; Lindh, I.; McLafferty, F. W. *Anal. Chem.* **2000**, *73*, 19-22.
(281) Adamson, J. T.; Håkansson, K. *J. Prot. Res.* **2006**, *5*, 493-501.
(282) Simon, M. D.; Chu, F.; Racki, L. R.; de la Cruz, C. C.; Burlingame, A. L.; Panning, B.; Narlikar, G. J.; Shokat, K. M. *Cell* **2007**, *128*, 1003-1012.
(283) Hopkinson, A. C. *Mass Spectrom. Rev.* **2009**, *28*, 655-671.
(284) Chu, I. K.; Rodriquez, C. F.; Lau, T.-C.; Hopkinson, A. C.; Siu, K. W. M. *J. Phys. Chem. B* **2000**, *104*, 3393-3397.
(285) Wee, S.; O'Hair, R. A. J.; McFadyen, W. D. *Int. J. Mass Spectrom.* **2004**, *234*, 101-122.
(286) Bagheri-Majdi, E.; Ke, Y.; Orlova, G.; Chu, I. K.; Hopkinson, A. C.; Siu, K. W. M. *J. Phys. Chem. B* **2004**, *108*, 11170-11181.
(287) Barlow, C. K.; Wee, S.; McFadyen, W. D.; x; Hair, R. A. J. *Dalton Trans.* **2004**.
(288) Ke, Y.; Zhao, J.; Verkerk, U. H.; Hopkinson, A. C.; Siu, K. W. M. *J. Phys. Chem. B* **2007**, *111*, 14318-14328.
(289) Laskin, J.; Yang, Z.; Chu, I. K. *J. Am. Chem. Soc.* **2008**, *130*, 3218-3230.
(290) Wee, S.; O'Hair, R. A. J.; McFadyen, W. D. *Int. J. Mass Spectrom.* **2006**, *249-250*, 171-183.

(291) Thompson, M. S.; Cui, W.; Reilly, J. P. *Angew. Chem. Int. Ed.* **2004**, *43*, 4791-4794.
(292) Cui, W.; Thompson, M. S.; Reilly, J. P. *J. Am. Soc. Mass Spectrom.* **2005**, *16*, 1384-1398.
(293) Kim, T.-Y.; Thompson, M. S.; Reilly, J. P. *Rapid Commun. Mass Spectrom.* **2005**, *19*, 1657-1665.
(294) Ly, T.; Julian, R. R. *J. Am. Chem. Soc.* **2007**, *130*, 351-358.
(295) Sun, Q.; Yin, S.; Loo, J. A.; Julian, R. R. *Anal. Chem.* **2010**, *82*, 3826-3833.
(296) Ly, T.; Julian, R. R. *J. Am. Chem. Soc.* **2010**, *132*, 8602-8609.
(297) Masterson, D. S.; Yin, H.; Chacon, A.; Hachey, D. L.; Norris, J. L.; Porter, N. A. *J. Am. Chem. Soc.* **2003**, *126*, 720-721.
(298) Yin, H.; Chacon, A.; Porter, N. A.; Masterson, D. S. *J. Am. Soc. Mass Spectrom.* **2007**, *18*, 807-816.
(299) Ryzhov, V.; Lam, A.; O'Hair, R. *J. Am. Soc. Mass Spectrom.* **2009**, *20*, 985-995.
(300) Wee, S.; Mortimer, A.; Moran, D.; Wright, A.; Barlow, C. K.; O'Hair, R. A. J.; Radom, L.; Easton, C. J. *Chem. Commun.* **2006**, 4233-4235.
(301) Lam, A. K. Y.; Ryzhov, V.; O'Hair, R. A. J. *J. Am. Soc. Mass Spectrom.* **2010**, *21*, 1296-1312.
(302) Barlow, C. K.; Wright, A.; Easton, C. J.; O'Hair, R. A. J. *Org. Biomol. Chem.* **2011**, *9*, 3733-3745.
(303) Osburn, S.; O'Hair, R. A. J.; Ryzhov, V. *Int. J. Mass Spectrom.* **2012**, *316–318*, 133-139.
(304) Hodyss, R.; Cox, H. A.; Beauchamp, J. L. *J. Am. Chem. Soc.* **2005**, *127*, 12436-12437.
(305) Lee, M.; Kang, M.; Moon, B.; Oh, H. B. *Analyst* **2009**, *134*, 1706-1712.
(306) Sohn, C. H. *New Reagents and Methods for Mass Spectrometry-based Proteomics Investigations*. Ph.D. Dissertation, California Institute of Technology, Pasadena, CA, 2011.
(307) Lee, M.; Lee, Y.; Kang, M.; Park, H.; Seong, Y.; June Sung, B.; Moon, B.; Bin Oh, H. *J. Mass Spectrom.* **2011**, *46*, 830-839.
(308) Lee, J.; Park, H.; Kwon, H.; Kwon, G.; Jeon, A.; Kim, H. I.; Sung, B. J.; Moon, B.; Oh, H. B. *Anal. Chem.* **2013**, *85*, 7044-7051.
(309) Laskin, J.; Yang, Z.; Ng, C. M. D.; Chu, I. K. *J. Am. Soc. Mass Spectrom.* **2010**, *21*, 511-521.
(310) Laskin, J.; Yang, Z.; Lam, C.; Chu, I. K. *Anal. Chem.* **2007**, *79*, 6607-6614.
(311) Sun, Q.; Nelson, H.; Ly, T.; Stoltz, B. M.; Julian, R. R. *J. Proteome Res.* **2008**, *8*, 958-966.
(312) Moore, B.; Sun, Q.; Hsu, J.; Lee, A.; Yoo, G.; Ly, T.; Julian, R. *J. Am. Soc. Mass Spectrom.* **2012**, *23*, 460-468.
(313) Zhang, X.; Julian, R. R. *Int. J. Mass Spectrom.* **2011**, *308*, 225-231.
(314) Zhang, X.; Julian, R. R. *J. Am. Soc. Mass Spectrom.* **2013**, *24*, 524-533.
(315) Moore, B. N.; Blanksby, S. J.; Julian, R. R. *Chem. Commun.* **2009**, 5015-5017.
(316) Ly, T.; Julian, R. R. *J. Am. Soc. Mass Spectrom.* **2009**, *20*, 1148-1158.
(317) Diedrich, J. K.; Julian, R. R. *Anal. Chem.* **2011**, *83*, 6818-6826.
(318) Diedrich, J. K.; Julian, R. R. *Anal. Chem.* **2010**, *82*, 4006-4014.
(319) Tao, Y.; Quebbemann, N. R.; Julian, R. R. *Anal. Chem.* **2012**, *84*, 6814-6820.

(320) Zhang, L.; Reilly, J. P. *J. Am. Soc. Mass Spectrom.* **2009**, *20*, 1378-1390.
(321) Thomas, D. A.; Sohn, C. H.; Gao, J.; Beauchamp, J. L. *J. Phys. Chem. A* **2014**, *118*, 8380-8392.
(322) Schaftenaar, G.; Noordik, J. H. *J. Comput.-Aided Mol. Des.* **2000**, *14*, 123-134.
(323) Zhao, Y.; Schultz, N. E.; Truhlar, D. G. *J. Chem. Theory Comput.* **2006**, *2*, 364-382.
(324) Zhao, Y.; Truhlar, D. *Theor. Chem. Account* **2008**, *120*, 215-241.
(325) Zhao, Y.; Truhlar, D. G. *J. Phys. Chem. A* **2008**, *112*, 1095-1099.
(326) Gronert, S.; O'Hair, R. A. J. *J. Am. Chem. Soc.* **1995**, *117*, 2071-2081.
(327) Fu, A.-p.; Du, D.-m.; Zhou, Z.-y. *Chem. Phys. Lett.* **2003**, *377*, 537-543.
(328) Miao, R.; Jin, C.; Yang, G.; Hong, J.; Zhao, C.; Zhu, L. *J. Phys. Chem. A* **2005**, *109*, 2340-2349.
(329) Wendler, K.; Thar, J.; Zahn, S.; Kirchner, B. *J. Phys. Chem. A* **2010**, *114*, 9529-9536.
(330) Izgorodina, E. I.; Brittain, D. R. B.; Hodgson, J. L.; Krenske, E. H.; Lin, C. Y.; Namazian, M.; Coote, M. L. *J. Phys. Chem. A* **2007**, *111*, 10754-10768.
(331) Marzluff, E. M.; Beauchamp, J. L. In *Large Ions : Their Vaporization, Detection, and Structural Analysis*; Wiley: Chichester ; New York, 1996, pp. 115-143.
(332) Marzluff, E. M.; Campbell, S.; Rodgers, M. T.; Beauchamp, J. L. *J. Am. Chem. Soc.* **1994**, *116*, 7787-7796.
(333) Anh, N. T. *Frontier Orbitals: A Practical Manual*, 1st ed.; John Wiley and Sons: Hoboken, NJ, 2007.
(334) Yates, J. R.; Ruse, C. I.; Nakorchevsky, A. *Annu. Rev. Biomed. Eng.* **2009**, *11*, 49-79.
(335) Nilsson, T.; Mann, M.; Aebersold, R.; Yates, J. R.; Bairoch, A.; Bergeron, J. J. M. *Nat. Meth.* **2010**, *7*, 681-685.
(336) Perry, R. H.; Cooks, R. G.; Noll, R. J. *Mass Spectrom. Rev.* **2008**, *27*, 661-699.
(337) Mann, M.; Kelleher, N. L. *Proc. Natl. Acad. Sci. U.S.A.* **2008**, *105*, 18132-18138.
(338) Michalski, A.; Damoc, E.; Hauschild, J.-P.; Lange, O.; Wieghaus, A.; Makarov, A.; Nagaraj, N.; Cox, J.; Mann, M.; Horning, S. *Mol. Cell Proteomics* **2011**, *10*.
(339) van Midwoud, P. M.; Rieux, L.; Bischoff, R.; Verpoorte, E.; Niederländer, H. A. G. *J. Prot. Res.* **2007**, *6*, 781-791.
(340) Elias, J. E.; Haas, W.; Faherty, B. K.; Gygi, S. P. *Nat. Meth.* **2005**, *2*, 667-675.
(341) Herrero, M.; Ibañez, E.; Cifuentes, A. *Electrophoresis* **2008**, *29*, 2148-2160.
(342) Srebalus Barnes, C. A.; Hilderbrand, A. E.; Valentine, S. J.; Clemmer, D. E. *Anal. Chem.* **2001**, *74*, 26-36.
(343) Singer, D.; Kuhlmann, J.; Muschket, M.; Hoffmann, R. *Anal. Chem.* **2010**, *82*, 6409-6414.
(344) Winter, D.; Pipkorn, R.; Lehmann, W. D. *J. Sep. Sci.* **2009**, *32*, 1111-1119.
(345) Sweet, S. M. M.; Bailey, C. M.; Cunningham, D. L.; Heath, J. K.; Cooper, H. J. *Mol. Cell. Proteomics* **2009**, *8*, 904-912.
(346) Molina, H.; Matthiesen, R.; Kandasamy, K.; Pandey, A. *Anal. Chem.* **2008**, *80*, 4825-4835.
(347) Bush, M. F.; Hall, Z.; Giles, K.; Hoyes, J.; Robinson, C. V.; Ruotolo, B. T. *Anal. Chem.* **2010**, *82*, 9557-9565.
(348) Wyttenbach, T.; von Helden, G.; Bowers, M. T. *J. Am. Chem. Soc.* **1996**, *118*, 8355-8364.

(349) Shvartsburg, A. A.; Smith, R. D. *Anal. Chem.* **2008**, *80*, 9689-9699.
(350) Guevremont, R. *J. Chromatogr. A* **2004**, *1058*, 3-19.
(351) Kaufman, S. L. *J. Aerosol Sci.* **1998**, *29*, 537-552.
(352) de la Mora, J. F.; Ude, S.; Thomson, B. A. *Biotechnol. J.* **2006**, *1*, 988-997.
(353) Flagan, R. C. *Aerosol Sci. Technol.* **2004**, *38*, 890-899.
(354) Abbott, P. J.; Scace, B. *J. Vac. Sci. Technol. A* **2010**, *28*, 573-577.
(355) Zeebe, R. E. *Geochim. Cosmochim. Acta* **2011**, *75*, 2483-2498.
(356) Frank, M. J. W.; Kuipers, J. A. M.; van Swaaij, W. P. M. *J. Chem. Eng. Data* **1996**, *41*, 297-302.
(357) Tanaka, K.; Hashitani, T. *Trans. Faraday Soc.* **1971**, *67*, 2314-2317.
(358) Light, T. S.; Licht, S.; Bevilacqua, A. C.; Morash, K. R. *Electrochem. Solid-State Lett.* **2005**, *8*, E16-E19.
(359) Sirs, J. A. *Trans. Faraday Soc.* **1958**, *54*, 201-206.
(360) Pocker, Y.; Bjorkquist, D. W. *J. Am. Chem. Soc.* **1977**, *99*, 6537-6543.
(361) Sander, R. *Compilation of Henry's law constants for inorganic and organic species of potential importance in environmental chemistry (version 3)*; http://www.henrys-law.org/henry-3.0.pdf, Downloaded April 2016.